The Dissertation Committee for Enakshi Devinka Wikramanayake

Certifies that this is the approved version of the following Dissertation:

Electrical Control and Enhancement of Dropwise Condensation

Committee:

Vaibhav Bahadur, Supervisor

Ofodike Ezekoye

Li Shi

Roger Bonnecaze

Electrical Control and Enhancement of Dropwise Condensation

by

Enakshi Devinka Wikramanayake

Dissertation

Presented to the Faculty of the Graduate School of

The University of Texas at Austin

in Partial Fulfillment

of the Requirements

for the Degree of

Doctor of Philosophy

The University of Texas at Austin

May 2020

Dedication

I would like to dedicate this to my mother and father for all their unconditional love,

affection and support.

Acknowledgements

Abstract

Electrical Control and Enhancement of Dropwise Condensation

Enakshi Devinka Wikramanayake, Ph.D.

The University of Texas at Austin, 2020

Supervisor: Vaibhav Bahadur

Condensation of vapor typically occurs via the formation of condensate films on condensing surfaces; however, the liquid film imposes a substantial thermal resistance to heat transfer. Filmwise condensation heat transfer can be enhanced by 5-7X by condensing vapor as droplets, which roll-off the surface, thereby preventing buildup of a liquid film. Dropwise condensation heat transfer can be enhanced by the use of electrowetting (EW) to enhance coalescence, growth and shedding of condensed droplets. This dissertation includes several fundamental studies on EW-enhanced dropwise condensation. Experiments, analytical modeling and statistical modeling are used to gain a deeper understanding of droplet growth, coalescence and shedding under EW.

Chapter 1 details the motivation for this study and the objectives of this dissertation. Chapter 2 includes a literature review of condensation, electrowetting and data science-based statistical methods. Chapter 3 presents a detailed experimental study of dropwise condensation of humid air under the influence of electrowetting fields. An analytical heat transfer model, which accounts for the presence of non-condensable gases, is used to

predict the heat transfer benefits associated with electrowetting-assisted condensation. Chapter 4 presents a detailed analysis of electrowetting-induced coalescence dynamics of a distribution of water droplets. Statistical modeling-based algorithms are used to identify key electrowetting-related parameters that influence droplet coalescence; the influence of these parameters on coalescence is quantified. Chapter 5 studies droplet shedding dynamics under electrowetting and shows that an intermittent electric field can significantly increase condensation rates (as compared to a continuous electric field). A key finding is the almost complete removal of water from surfaces in very short durations (< 1 sec) is observed. It is also found that the extent and rate of water removal depends on the applied voltage and frequency of the AC EW waveform, respectively. Chapter 6 presents a novel approach and an experimentally validated model to analyze the oscillations of water droplets under the influence of AC electrowetting. Chapter 7 summarizes key conclusions and outlines suggestions for future work.

Overall, the research reported in this dissertation has led to fundamental contributions in the areas of condensation and microfluidics. This multidisciplinary work has involved experiments, analytical modeling and statistical modeling. Results show that electrowetting fields influence all the phenomena important in dropwise condensation (growth, coalescence, shedding of droplets). Electrowetting is therefore a powerful tool to control and enhance condensation heat transfer. This research impacts applications in energy (steam condensation, refrigeration), water (atmospheric water harvesting, desalination) and infrastructure (self-cleaning).

Table of Contents

List of Tables

List of Figures

Chapter 1: Introduction

Condensation significantly impacts the performance of several engineering systems in the areas of power generation, refrigeration, HVAC (heating, ventilation, and air conditioning) and desalination. On common metallic surfaces, the most common mode of condensation is filmwise condensation (Figure 1.1a), wherein vapor condenses as a thin liquid film on the condensing surface [1]. The presence of this liquid film between the vapor and the condensing surface degrades heat transfer substantially.
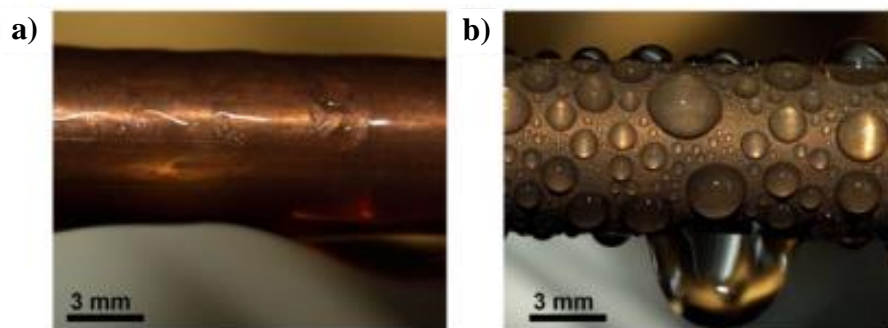
Figure 1.1 Comparison of a) filmwise and b) dropwise condensation. Figure 1.1 reprinted with permission from Miljkovic et al. Copyright 2013 Cambridge University Press.

A widely studied method to enhance condensation heat transfer is by using non-wetting surfaces to induce dropwise condensation (Figure 1.1b) [2]. Heat transfer coefficients can be enhanced by an order of magnitude by condensing vapor as droplets, which roll-off, thereby exposing the surface to fresh vapor [2]. This fundamental difference in the two condensation modes has inspired significant research on the use of

superhydrophobic (non-wetting) coatings for condensation heat transfer enhancement. Several types of surfaces have been studied for enhancing condensation including hydrophobic surfaces, superhydrophobic surfaces, and hybrid surfaces. A wide range of surface textures have been studied; parameters which have been varied include the length scale of surface features, shape and the hierarchy of roughness causing features [3]–[5]. Nature-inspired surfaces [6], [7] and lubricant infused surfaces have been widely studied as an avenue to increase droplet mobility and shedding [8], [9]. Another condensation enhancement technique, which has been widely explored, relies on jumping condensate droplets on super hydrophobic surfaces [10], [11]. This enhancement strategy is based on the observation that when two droplets coalesce, they will have leftover energy remaining after coalescence; this energy can be used to cause droplets to jump away from the surface.

More recently, a few studies have looked at the influence of electric fields on enhancement in dropwise condensation (DWC) of moisture. These studies show that an externally applied electric field can alter the droplet size distribution, droplet growth rate and coalescence and roll-off dynamics [12]–[16].

This dissertation studies the influence of electrowetting (EW) on dropwise condensation enhancement. Enhancement is a result of increased coalescence and growth of condensate droplets, and EW-promoted roll-off and shedding of droplets. EW is a well-understood microfluidic technology used to control the wettability and motion of droplets via the application of an electrical potential difference across a dielectric layer underlying the droplet [17], [18]. Of late, EW has attracted the attention of the microfluidics community as a tool to enhance condensation. The following chapters detail fundamental

analysis of droplet growth, coalescence and roll-off during DWC under continuous and intermittent electric fields.

1.1 MOTIVATION OF THE PRESENT WORK

Condensation heat transfer can be enhanced by 5-7X by switching from dropwise condensation to filmwise condensation [1]. Many studies have sought to optimize the surface texture and chemistry which maximize dropwise condensation [3]–[5]. These modifications can reduce contact angle hysteresis, reduce droplet roll-off sizes and remove larger droplets from the surface, all of which lead to higher condensation rates and enhanced condensation heat transfer (CHT). However, surface engineering-based approaches have limitations associated with low durability, performance degradation and fouling associated with surface textures [19].

Recent studies show that active methods of enhancing CHT have greater benefits than passive methods. Utilizing electrowetting for controlling DWC can enhance condensation heat transfer by 30-50% [12], [15]. Additionally, application of an electric field can increase the condensation rate by several orders of magnitude if the field is applied intermittently (see Chapter 5). Studies show that an electric field has the ability to remove a majority of droplets resting on a surface (Chapter 5). EW can also be used to control and alter the droplet size distribution on the surface (Chapter 3) [14]. A key advantage of EW is that it can provide dynamic, real-time control of condensation heat transfer.

Some specific applications of this work are discussed ahead briefly. Similar to classical condensation applications, EW controlled DWC can enhance phase change heat transfer in power generation, refrigeration, HVAC systems, desalination, water recovery

3

from cooling tower exhaust etc. A significant area which would benefit from this technology is water harvesting. Atmospheric water harvesting systems condense and collect moisture from humid air for various applications ranging from municipal consumption to use in the oil and gas industry [20]–[22]. The high condensate removal rates that can be achieved by applying intermittent electric fields can substantially enhance water harvesting rates[16].

In addition to heat transfer applications, the ability of an electric field to clear the surface of >90% of liquid makes this an attractive method for self-cleaning, dust removal or anti-fouling applications [23], [24]. As droplets are removed from the surface, they can carry away dust, debris or bacteria which can be exploited for self-cleaning applications in solar cells, biotechnology or commercial applications such as cleaning high rise windows, glass or car windshields. The performance of passive self-cleaning surfaces is limited by characteristics such as surface hydrophobicity and contact angle hysteresis, which determine the conditions under which droplets can overcome pinning forces and roll-off [25]. Via EW, the user can control droplet roll-off dynamics and frequency by applying the appropriate electric field based on surface cleaning requirements. EW will perturb the three-phase contact line, de-pin droplets from the surface and cause droplet coalescence to form large enough droplets that roll-off the surface. These droplets carry away dust and debris as they roll off, leaving behind a clean surface.

A specific advantage of using EW as an active method for such applications is the low power requirement (<1 mW per microfluidic operation). The dielectric layer which isolates the droplet from the electrodes prevents current flow, which reduces power consumption despite the high voltage requirements [17]. It must be noted that

4

electrification of DWC does present formidable challenges. Finding a dielectric material which can withstand long term exposure to electric fields and moisture is challenging. This has been a longstanding challenge for the EW community. Throughout this dissertation a variety of dielectric materials were utilized in various configurations; related findings on the reliability of dielectric materials and device durability are detailed in section 7.2.

1.2 OBJECTIVES OF THE PRESENT WORK

The work presented in this dissertation is a fundamental study on the influence of electrowetting on DWC. This dissertation addresses the following fundamental questions related to various factors that influence DWC under EW:

- What is the influence of an EW field on various phenomena underlying DWC (initial growth, coalescence, roll-off)?
- How significant is the electrical waveform in influencing EW-assisted DWC? How is DWC different for AC fields as compared to DC fields?
- What is the influence of the AC frequency on DWC?
- How does electrode geometry influence coalescence, growth and roll-off?
- How much enhancement in condensation heat transfer can EW provide?
- What is the influence of an EW field on macroscopic parameters: condensation rate, condensation heat transfer coefficient, droplet roll-off size and frequency?
- Can condensation be further enhanced by using an intermittent electric field to sweep away condensate (as compared to a continuous electric fields)?
- What are good dielectric materials for EW-assisted condensation applications? Attributes of a good material include high electrical breakdown strength, high dielectric constant, pinhole-free nature, good adhesion and moisture resistance.

1.3 ORGANIZATION OF THE DISSERTATION

The remainder of the dissertation is divided into six chapters. A detailed literature review of condensation, electrowetting and data science-based statistical analysis is included in Chapter 2. Chapter 3 describes a detailed study on EW-based enhancement of droplet growth and roll-off dynamics, as well as heat transfer enhancement during humid air condensation. Chapter 4 analyzes droplet coalescence dynamics using statistical data science-based algorithms to quantify the influence of voltage, AC frequency and electrode geometry on coalescence. Chapter 5 studies the influence of electric field, AC frequency and device geometry on droplet removal from surfaces. Chapter 6 details a new fundamentals-based analytical model to study contact angle oscillations-induced by electrowetting. Conclusions and suggestions for future work are outlined in Chapter 7. Appendices A-E include abstracts of journal and conference publications that were published during my time at graduate school.

Chapter 2: Literature Review

2.1 OVERVIEW OF CONDENSATION

Condensation is a key determinant of overall performance of systems involved in power generation, refrigeration and air-conditioning, water harvesting and desalination. Enhancing the heat and mass transfer associated with condensation can significantly improve system-level performance and efficiency.

2.1.1 Filmwise condensation heat transfer

In most current applications, water films condense as a thin film due to the hydrophilic nature of metallic condenser surfaces (Figure 2.1a). Filmwise condensation is a classical topic in phase change heat transfer and is well understood. The first studies on filmwise condensation were detailed by Nusselt [1], which studied condensation under the following assumptions:

- Condensation of pure, quiescent, saturated vapor at saturation temperature, with a laminar liquid film and with constant properties.

- Only the heat transfer due to condensation at the liquid-vapor interface was considered. Heat conduction in the vapor layer was neglected.

- Shear stress on the liquid-vapor interface was assumed to be negligible.

- Momentum and energy transfer by advection in the condensate film was assumed to be negligible as low velocity flow was considered. Heat transfer through the film is dominated by conduction.

Based on the above assumptions, the x-momentum equation during filmwise condensation [1], [26] can be expressed as:

$$\frac{\partial^2 u}{\partial y^2} = -\frac{g}{\mu_l}(\rho_l - \rho_v) \quad (2.1)$$

where u is the velocity of the film, μ_l is the dynamic viscosity of the liquid film, ρ_l is the density of the liquid phase, and ρ_v is the density of the vapor phase. The above expression balances viscous forces with buoyancy. Using the boundary conditions based on the assumptions above, the condensate mass flow rate, $\Gamma(x)$, can be obtained as [26]:

$$\Gamma(x) = \frac{g\rho_l(\rho_l - \rho_v)\delta^3}{3\mu_l} \quad (2.2)$$

where δ is the thickness of the liquid film. This analysis yields the film thickness δ, the average Nusselt number and average condensation heat transfer coefficient. Similar analysis has been conducted for filmwise condensation on plates and tubes and has been modified and improved for various applications.

Importantly, the liquid film between the vapor and condensing surface presents a significant resistance to heat transfer. Condensation heat transfer can be significantly enhanced by bringing vapor in direct contact with the surface, thereby eliminating the temperature gradient associated with the liquid film. This enhancement is possible by condensing vapor as droplets, which then roll-off exposing the surface to fresh vapor. The transition from condensing vapor from a film to droplets is dependent on surface wettability as well as vapor-to-surface temperature difference [27]. The characteristics of moisture condensing as droplets is discussed next.

2.1.2 Dropwise condensation and enhancements

Dropwise condensation (DWC) was first studied by Schmit et al. [2] in 1930; a much better understanding emerged in the 1960s. On a non-wetting or hydrophobic surface, vapor will condense as droplets (Figure 2.1 b) instead of a film, which then roll-off before merging to form a film. DWC heat transfer can be 5-7 times higher than filmwise condensation [2]. However, there exist many challenges to sustaining dropwise condensation, since many hydrophobic coatings are not durable, and show rapid performance deterioration. Recent research has focused on the development of coatings to ensure long lasting DWC with high condensation heat transfer coefficients.
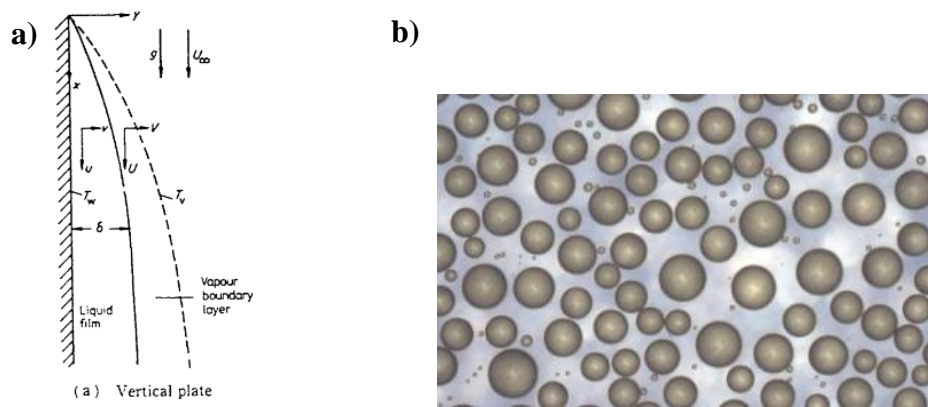
Figure 2.1 a) Filmwise condensation where a film develops on hydrophilic surface and b)
Dropwise condensation where condensate forms droplets on a hydrophobic
surface. Figure 2.1 a) reprinted with permission from Rose et al. Copyright
1998 Elsevier.

During DWC, nucleation takes place in sites such as cracks, pits and cavities. Droplets continue to grow in these locations by direct vapor condensation at the liquid

vapor interface[28]–[30]. As droplets grow large enough to contact neighboring droplets, the coalescence stage begins. As droplets merge and move, new droplets nucleate and grow in the area exposed by coalescence [29]. Throughout this process, the mean value of the droplet size distribution increases over time, and the distribution of droplet sizes widens. As droplets grow in size, surface coverage increases and as droplets coalesce and merge surface coverage decreases [28]. Finally, droplets merge and grow large enough that gravity causes them to roll-off the surface, exposing fresh area for nucleation, and the cycle continues. The size at which droplets roll off is related to the capillary length, $l_c = \sqrt{\frac{\gamma}{\rho g}}$ (γ is surface tension, ρ is density and g is gravity) which measures the relative importance of surface tension and gravitational forces. During roll-off, the departing droplet will capture additional fluid along its departure path, and thereby expose fresh areas for nucleation.

Once gravity shedding begins, the system reaches a pseudo steady-state where the droplet size distribution and average droplet size remain constant [31]. These droplet size distributions can be used to estimate the condensation heat transfer. Classical models have been developed to estimate the thermal resistance associated with conduction through the droplet [32], interface resistance at the vapor-liquid interface [5], [33] and the resistance due to droplet curvature for a single droplet [5], [34]. Knowledge of droplet-related resistances and the droplet size distribution can be used to estimate the overall condensation heat transfer [34].

In addition to roll-off dynamics, the entire process of DWC is also significantly influence by droplet coalescence dynamics, analyzed in Chapter 4. Coalescence of droplets is a complex microfluidic phenomenon governed by various interactions occurring at the three-phase contact line and various interfaces. When droplets coalesce, initially a liquid

bridge forms between the droplets, followed by the final droplet forming at the center of mass of the original droplets [28], [35]. Studies show that during this process, contact line pinning and viscous dissipation influence the receding contact angle dynamics more strongly than advancing contact line dynamics [36]. Also, the two merging droplets leave behind fresh dry area for nucleation to occur. Many studies exist on enhancing droplet coalescence by modifying the chemistry or texture of the condensing surface [5], [37]–[39] to create areas for fresh nucleation. Alternatively, there are studies on shifting the droplet size distribution to smaller droplets, which would increase heat and mass transfer.

Many recent efforts have studied passive methods of inducing DWC, which includes manipulation of surface chemistry and texture. Hydrophilic surfaces, such as copper, have a higher surface energy which causes water to spread. Conversely, on low energy hydrophobic surfaces, the condensate forms droplets, significantly reducing surface coverage and increasing heat transfer [40]. An alternate route to disallow film formation is via surface texturing. Keeping the condensed droplets in the Cassie state (droplet resting on top of roughness causing elements) will promote droplet shedding. This is the basis for a lot of recent studies on superhydrophobicity-enhanced condensation [5], [41].

While superhydrophobicity has clear advantages in promoting roll-off , the energy barrier for initiation of nucleation is higher on hydrophobic and superhydrophobic surfaces, than on a hydrophilic surface [6], [27]. Consequently, researchers have studied hybrid hydrophobic-hydrophilic surfaces where hydrophilic patches are introduced into a hydrophobic surface to locally lower the nucleation barrier [4], [42]. Mondal et al. [3] created a hybrid surface by impaling a superhydrophobic film into an array of steel hydrophilic needles. Nucleation initiated on the tips of the needles, but the hydrophobic

11

nature of the surrounding surface allowed for easier droplet roll-off. The same group showed water collection enhancement of 63% on a polyethylene hydrophobic surface compared to a hydrophilic copper surface [3].

Many such hybrid surface designs are nature inspired [43]–[45]. As an illustration, the Namib dessert beetle uses hydrophilic bumps on its hydrophobic back to condense and collect water droplets. On a similar note, Hou et al. [6] developed hydrophilic patches on top of micropillars which were surrounded by superhydrophobic nano-grass, shown in Figure 2.2a; 63% enhancement in heat transfer coefficient was observed. Similarly, Ghosh et al. [7] drew from the design of veins on a banana leaf to fabricate a hydrophilic-hydrophobic pattern which combines dropwise and filmwise condensation; a 19% enhancement in condensate collection was demonstrated. A more recent study by Cha et al. [46] demonstrated that stable DWC can be achieved on flat hydrophilic surfaces having very low contact angle hysteresis. The droplet size distributions on these surfaces matched the classical distribution for DWC, and the low contact angle hysteresis allowed easy droplet departure, resulting in high heat transfer.
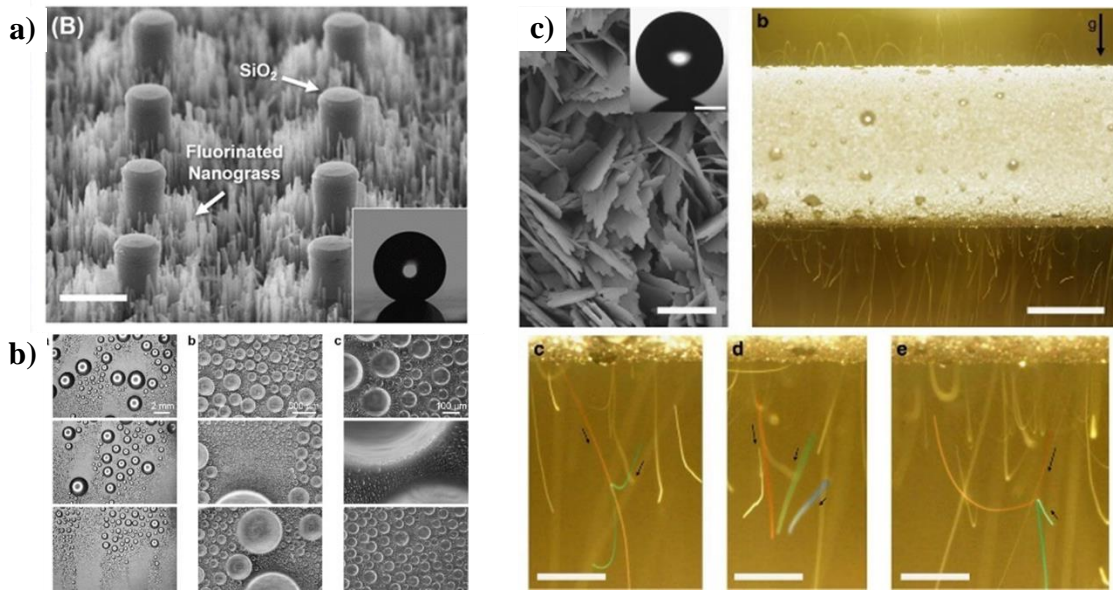
Figure 2.2. Surface enhancements to promote dropwise condensation: a) nature-inspired hybrid hydrophilic-hydrophobic surfaces, b) lubricant-infused surfaces, c) jumping droplets from superhydrophobic surfaces. Figure 2.2 a) reprinted with permission from Hou et al. Copyright 2014 American Chemical Society. Figure 2.2 b) reprinted with permission from Weisensee et al. Copyright 2017 Elsevier. Figure 2.2 c) reprinted with permission from Miljkovic et al. Copyright 2013 Springer Nature.

An alternate approach to enhancing condensation on hydrophobic surfaces is to infuse lubricating liquids into micro or nano scale structures patterned on condensing surfaces; these have been referred to as SLIP surfaces (Slippery Liquid-Infused Porous Surfaces) or LIS (lubricant-infused surfaces) [8], [9], [47]. The advantage of these surfaces is the reduction in droplet shedding radius and higher droplet mobility, since droplets float on the impregnated lubricant, resulting in reduced pinning [9]. However, the lubricating

oil on the surface can cloak or encapsulate droplets, so appropriate selection of the lubricating liquid is critical. Weisensee et al. [8] used a textured aluminum surface infused with Krytox-based lubricant oils and mineral oil to show that the droplet size distribution seen in classical DWC was independent of texture feature sizes, seen in Figure 2.2b. LIS-based condensation was 10-15X times higher as compared to filmwise condensation.

Recently, there have been multiple studies on dropwise condensation enhancement via 'jumping droplets' on superhydrophobic surfaces, illustrated in Figure 2.2c [10], [11]. Droplets jump out of plane on superhydophobic surfaces when they coalesce, due to the leftover energy remaining after coalescence. Out-of-plane jumping has been reported from coalescence of droplets in the diameter range 50-100 μm. For smaller diameters, jumping speeds rapidly decrease [5], [10]. Enright et al. found that droplets of diameter ~10 μm can jump to speeds of 1.4 m/s normal to the condensing surface [39]. They also estimated that only 6% of the surface energy is converted to kinetic energy of the jumping droplet, showing that this is a low efficiency conversion process. Overall, several factors such as surface topography, wettability, condensate fluid and surrounding gas density influence droplet jumping [10]. Miljkovic et al. [11] showed that jumping droplets on nanostructured CuO surfaces enhanced heat flux and condensation heat transfer coefficients by 25% and 30%, respectively, compared to classical DWC on Cu surfaces.

It is important to note that most condensation studies have been conducted under saturated vapor conditions where non-condensable components are not present. Many studies [48]–[51] clearly show that non-condensable gases (NCGs) degrade heat transfer during filmwise condensation and DWC. In humid air, a layer of NCGs accumulates around the condensate film forming a NCG diffusion layer, which results in a temperature

14

gradient between the ambient humid air and condensate-air interface [48]–[52]. A complex model for condensation of pure steam in the presence of NCGs was developed by Nusselt [48] that included a diffusion layer for vapor. Similarly, Zhao et al. [49] showed that the largest thermal resistance in DWC heat transfer is due to the presence of the NCG region around droplets. Castillo et al. [29] showed that droplet growth rate strongly depends on the relative humidity. However, the action of droplets rolling off in DWC can lead to mixing of the diffusion boundary layer, which can enhance mass diffusion [52]. Although many studies have examined the complications and phenomena associated with NCGs, there is limited analysis on heat transfer in the presence of an NCG boundary layer during DWC.

2.1.3 Applications of dropwise condensation-Atmospheric water harvesting

As a phase change process, condensation is the basis for many applications including power generation, desalination and heat exchangers [53], [54]. Additionally, atmospheric water harvesting (AWH) technologies can take advantage of condensation enhancements for increased condensation rates and heat transfer [20]. AWH refers to the condensation of water from humid air. The atmosphere is one of the largest freshwater reservoirs on the planet; 1 square kilometer of land holds between 10,000-30,000 m^3 of moisture above it [55]. Tapping into this source of water through AWH can relieve the pressure on conventional water sources for growing population levels.

Passive methods of AWH have been widely explored though fog or dew harvesting. Fog fences [56] are a passive method to collect water in high humidity areas by using mesh structures to trap fog droplets, shown in Figure 2.3 a [57]. Recent studies have looked into

optimizing the fiber mesh pattern and chemistry to maximize fog collection [58]. However, fog harvesting techniques work under very limited conditions and require large collection areas. Despite these limitations, small-scale fog harvesting projects have been implemented in many parts of the world, especially in South and Central America, Africa, Europe and Asia [57].
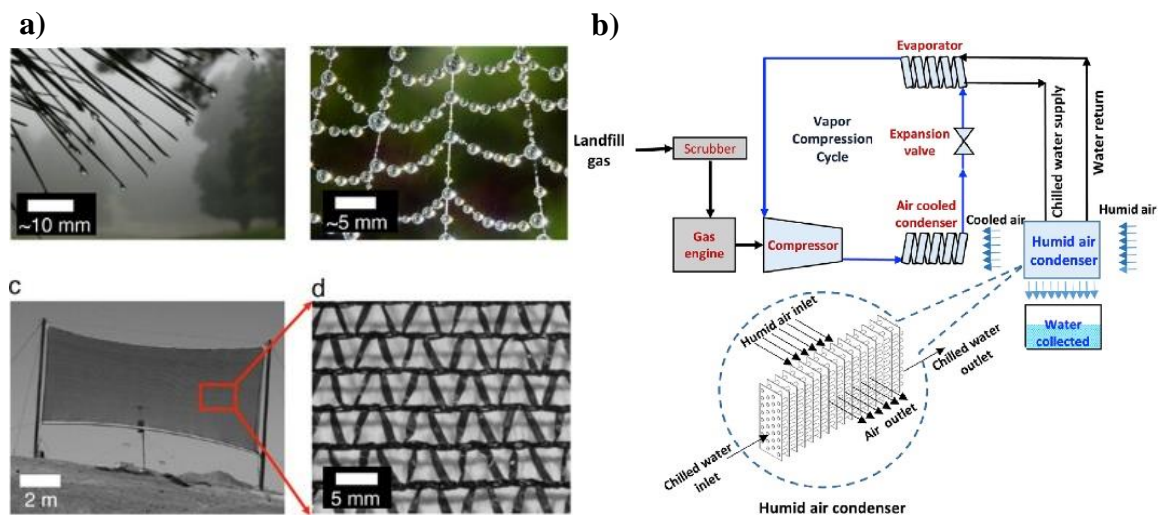
Figure 2.3. a) Natural and artificial fog harvesting systems b) Waste natural gas based-atmospheric water harvesting system. Figure 2.3 a) reprinted with permission from Park et al. Copyright 2013 American Chemical Society. Figure 2.3 b) reprinted with permission from Wikramanayake et al. Copyright 2017 Elsevier.

Alternatively, water collection rates can be significantly increased by using active water harvesting techniques, which cool air below the dew point to promote condensation. The cooling capacity for sustaining condensation can be provided by various kinds of

16

refrigeration systems or radiative cooling. Alternatively, moisture absorption can be used via a desiccant system, and via the use of other moisture absorbing or adsorbing materials [21], [22], [59]–[61]. Despite the enormous quantity of moisture in air, industrial scale AWH implementation has been stifled due to the energy intensive (2260 kiloJoules/liter of water) nature of condensation. Commercial development of AWH systems is limited to electricity powered units that produce hundreds of gallons of water daily, but with high electricity costs [22]. The economic viability of AWH projects would be significantly enhanced if the energy requirements could be met inexpensively.

Excess natural gas, which is currently either vented or flared can alternately power AWH systems and enable large scale deployment of this technology. Studies show that using natural gas that would be flared from hydraulically fractured oil fields, or methane that would be vented from decomposition of solid waste in landfills can be used to power onsite AWH systems [21], [22]. The natural gas that would be flared or the methane that would be vented can be used to power a gas engine which would drive the compressor of a vapor compression cycle, which generates cooling capacity for condensation (Figure 2.3b). This process can generate high-quality freshwater for local oil and gas production, noting that many of these operations take place in highly water stressed areas. The advantages of implementing such a technology include reduced stress on ground water and reduced water trucking distances. Overall, enhancing dropwise condensation and condensation rates using electric fields, as described in Chapters 4 and 5, would greatly benefit AWH technologies by bringing down the cost of AWH.

2.2 OVERVIEW OF ELECTROWETTING

Over the past two decades, electrowetting (EW) has emerged as a powerful tool to control droplet-based microfluidic operations such as droplet motion, generation and merging [17], [18], [62]–[64]. EW is based on the electrical modulation of the solid-liquid interfacial tension to control wettability. By applying a potential difference between an electrically conductive droplet resting on a dielectric layer and an underlying ground electrode, the droplet can be made to wet the surface. The reduction in solid-liquid surface energy can be attributed to charge accumulation at the interface caused by the electric field, where the presence of like charges at the interface causes the liquid to spread out. Figure 2.4 illustrates the reduction in contact angle upon application of an external voltage, which can be modeled using the *Young-Lippmann* equation [17] as:

$$cos\theta = cos\theta_{eq} - \frac{C}{2\gamma_{lv}}V^2 \qquad (2.3)$$

where θ_{eq} is the equilibrium contact angle (no voltage), γ_{lv} is the liquid-vapor interfacial tension, V is the applied voltage and C is the capacitance of the dielectric layer (under the droplet). It is noted that the electric double layer is thinner than the dielectric layer, hence the overall capacitance is determined by the capacitance of the dielectric layer [17], [18]. Importantly, the dielectric layer prevents flow of current, and is critical to the performance of EW devices. Most EW devices also have a thin layer of a hydrophobic coating such as Teflon to reduce the frictional resistance to contact-line motion.
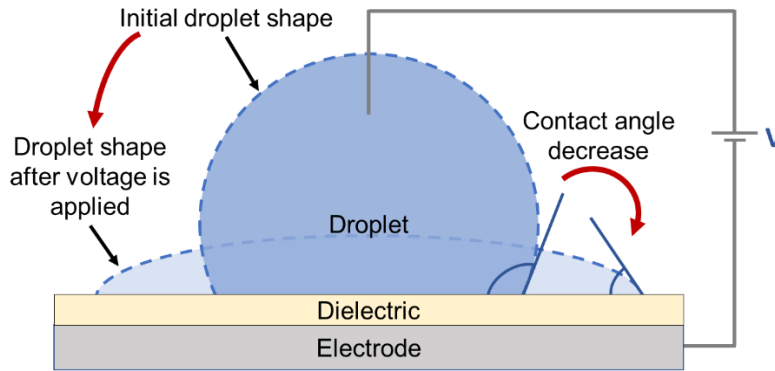
Figure 2.4 Schematic illustration of electrowetting (contact angle reduction due to an electrical potential difference across a dielectric layer underlying a droplet).

EW-induced droplet spreading requires exceeding a threshold voltage (V_{th}), at which the electrostatic force exceeds the pinning force at the three-phase line. Above the threshold voltage, the contact angle change is reasonably well captured by the Lippmann's equation. However, the contact angle does not keep on decreasing with voltage. Beyond the saturation voltage, V_s, the contact angle saturates (no further change with voltage). One theory underlying contact angle saturation is the divergence of the electric field near the contact line as the curvature reduces [17], [18]. Also, instabilities at the contact line, especially when AC voltages are applied, cause 'satellite droplets' to be ejected from the contact line as the voltage is increased beyond V_s [17], [18]. It is noted that contact angle saturation and satellite droplet emission remain unresolved topics in the field.

Most of the studies presented in this dissertation involve the application of an AC electric field, and it is important to understand the influence of AC frequency on EW. The frequency of the applied electrical waveform significantly influences electrowettability. For DC and low frequency AC voltages, the electrically conducting droplet can be

19

considered equipotential; there is no electric field inside the droplet and the entire potential difference falls across the dielectric layer (typically 1-2 µm thick) [17]. At higher frequencies, the electric field penetrates inside the droplet. The distribution of the electrical potential is thus fundamentally different for AC fields as compared to DC fields.

It is noted that an AC field has distinct advantages over DC fields for EW applications. AC voltages reduce contact angle hysteresis; under an AC field the contact line is continuously perturbed by the oscillating voltage, de-pinning the contact line from the surface[18]. Alternatively, a DC field pins the droplets to the surface, thereby increasing contact angle hysteresis. Consequently, threshold voltages are lower and contact angle saturation can be delayed under AC voltages as compared to DC voltages [17], [18].

It is noted that the *Young-Lippmann* equation is strictly valid only for DC voltages and low frequency AC voltages, wherein the liquid can be treated as a perfect electrical conductor. At higher frequencies, the analysis becomes more complex, and the resistance and capacitance of the droplets and the dielectric layer [17] needs to be accounted for. In general, the role of AC frequency can be explained by examining the expression for the complex permittivity of a material [17]:

$$\varepsilon^* = \varepsilon\varepsilon_0 - j\frac{\sigma}{\omega} \qquad (2.4)$$

where ε is dielectric constant, σ is electrical conductivity and ω is AC frequency. The first term represents the capacitance of the material, and the second term represents the electrical resistance. As the frequency increases the second term reduces in significance, implying that any material (liquid, in this instance) will behave more like a dielectric material than an electrical conductor. Effectively, the electric field lines penetrate the liquid, which can no longer be assumed equipotential. The reduced magnitude of the

20

electric field correspondingly reduces electrowettability above the relaxation frequency (σ/ε) of the liquid [65].

AC and DC voltages also result in very different sessile droplet dynamics and Chapter 6 presents a detailed analysis of droplet oscillations under AC frequencies. Under AC fields, droplets oscillate in response to the sinusoidal waveform, which is determined by the interplay of inertia and interfacial energies [66]. The frequency of the oscillating force is twice the input electrical force [65]–[67]; therefore the droplet oscillates at twice the AC frequency. At low AC frequencies, oscillations induce hydrodynamic flow within a droplet resulting in mixing and oscillatory motion [65]. However, droplet oscillations decrease at higher frequencies [68], [69]. At very high frequencies fluid flow and mixing is induced by electrothermally driven flows due to gradients in temperature arising from Joule heating within the droplet, which results in gradients in conductivity and permittivity [70].

Since AC fields are extensively used in this dissertation, and AC fields are invariably accompanied by droplet oscillations, a brief review of droplet oscillations under AC EW is provided. There exist many studies [65], [71]–[73] which have analyzed the influence of AC electric fields on droplet oscillations. In most such studies, transient droplet oscillations were quantified by measuring the transient contact angle (CA) or contact radius [66], [74]. Additionally, many of these studies used the traditional EW configuration, which consists of a wire electrode (or plate) in contact the droplet resting on a dielectric surface. The electric field is established using an electrode under the dielectric and the top wire or plate (which is usually electrically grounded). This traditional EW configuration (Figure 2.5 a) is widely used for studies on various microfluidic operations

such as pumping, merging and splitting [63], [64], [75]. One significant disadvantage of this configuration is that the wire/plate will influence the hydrodynamic response of the liquid to an electric field, and also distort the droplet shape.
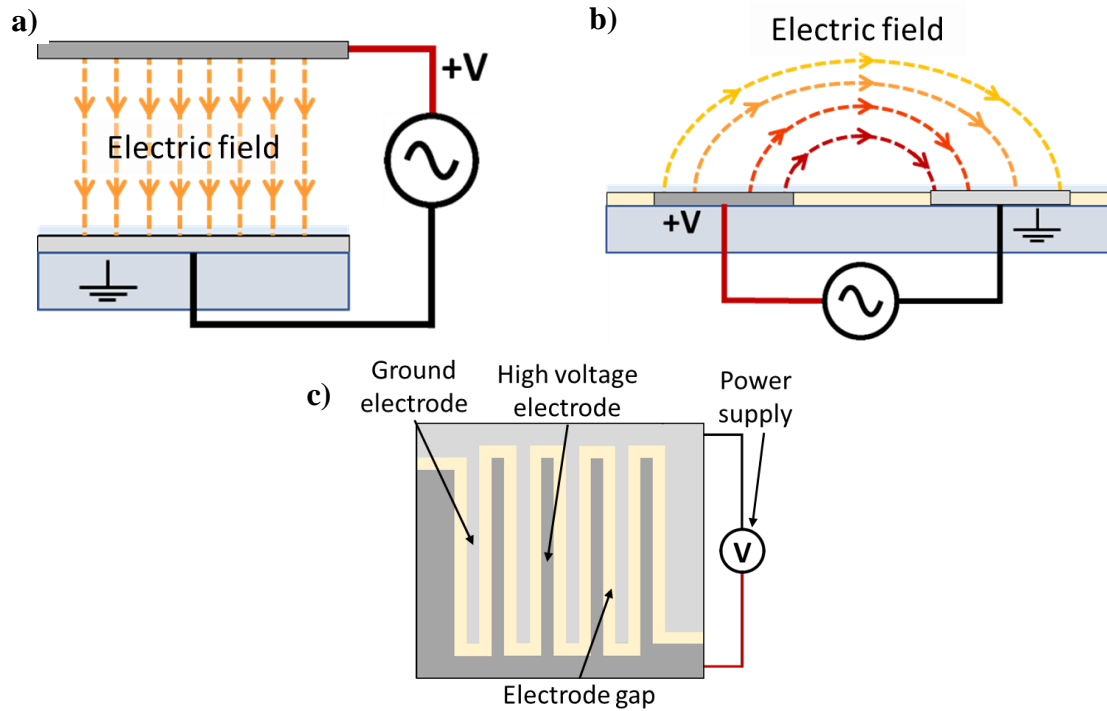
Figure 2.5 a) Traditional parallel plate EW configuration, b) co-planar electrode configuration, c) interdigitated electrode design for co-planar electrode configuration

Electrowetting experiments with droplets not having a physical electrode protruding into them are possible if the active and the ground electrodes are both located on the bottom plate; this configuration is known as the coplanar electrode arrangement [76]. While an overwhelming number of studies utilize the traditional EW configuration,

22

there do exist studies which utilize the coplanar electrode arrangement. Key previous studies using this arrangement are briefly summarized ahead.

Malk et al. [65] used coplanar electrode geometry to observe rotating flow within an oscillating droplet. Increasing the frequency reduced the amplitude of droplet oscillations and reduced the change in CA during oscillations. However, there was no reported relation or model to predict the amplitude of CA change as a function of the applied voltage and frequency. Another study [66] using the coplanar electrode geometry involved a ground electrode placed between two high voltage electrodes. Droplet dynamics under the influence of AC EW was quantified by measuring the transient CA and contact radius under various frequencies and voltages. Hong et al. [69] used the coplanar electrode geometry in experiments to measure droplet oscillations and contact line dynamics. At low frequencies periodic oscillations in the droplet shape were observed; at high frequencies no shape change was recorded. Yamada [67] took a different approach and used a tangential electric field to oscillate droplets to understand the influence of resonance frequency on the change in droplet shape. It was seen that resonance vibration of the droplet occurred when the frequency of the AC field was half the natural frequency of the droplet. Furthermore, the resonance frequency was seen to depend on droplet volume, the surface energy and the electrostatic force profile [67].

In addition to the above four studies, other studies on droplet oscillations under AC EW have used the traditional EW configuration. Oh et al. [71] studied the influence of AC frequency on oscillation behavior (changes in shape modes and resonance frequencies), and derived a shape mode equation for droplet oscillations under AC EW. Dash et al. [74] measured the transient response of droplets under DC and AC fields and reported that the

time taken by a droplet to attain a steady shape is approximately 35 ms (although there is a dependence on the applied voltage). By measuring and comparing the CA under AC and DC electric fields, Li et al. [77] showed the benefits of AC EW in overcoming pinning forces at the contact line.

In the experiments conducted in this dissertation (Chapters 3-6), the EW devices are fabricated such that electrodes have a co-planar geometry. In this geometry, the positive and ground electrodes are in the same plane, separated by a non-conducting gap between them, as shown in Figure 2.6. Under this configuration, the field lines form an arc from the high voltage electrode to the ground electrode based on the voltage gradient generated between the two electrodes [78]. The qualitative difference in the nature of the electric field lines implies that the capacitance will be very different for the two configurations. In the following chapters, an analytical estimate of the capacitance [78]–[80] for our co-planar electrode geometry C_{cp}, is modeled as:

$$C_{cp} = \frac{2\varepsilon_0 \varepsilon_d l}{\pi A} \ln\left[\left(1 + \frac{w}{a}\right) + \sqrt{\left(1 + \frac{w}{a}\right)^2 - 1}\right] \qquad (2.5)$$

where w is the electrode width, a is half the electrode gap width, l is the length of the electrodes and A is the wetted area of the droplet. This capacitance model accounts for the relative width of electrodes in relation to the width of the electrode gap. Alternatively, the traditional parallel plate capacitance is modeled as $C_{pp} = \frac{\varepsilon_0 \varepsilon_d}{d}$, where ε_0 is the electrical permittivity of free space, ε_d is the dielectric constant and d is the thickness of the dielectric layer [17], [18]. This co-planar geometry is advantageous for experiments described ahead as it eliminates the presence of a wire or a top plate that would obstruct condensation from surrounding air.
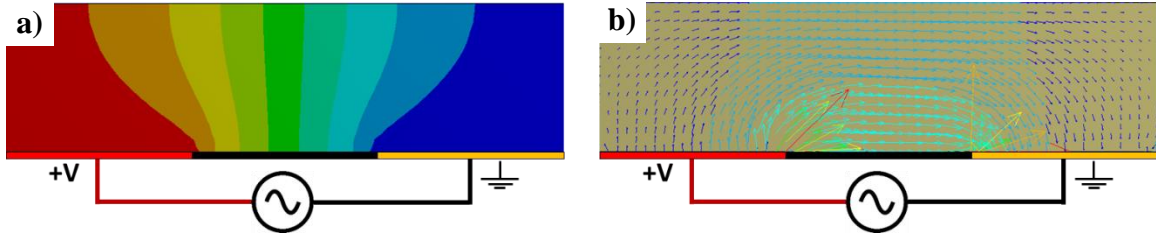
Figure 2.6. a) Voltage distribution and b) electric field between the parallel co-planar electrode arrangement used in this work.

While the above discussion was on the topic of EW-induced contact angle modulation, EW has been widely studied for droplet actuation and motion in many micro-fluidic applications [81], [82]. EW droplet movement devices consist of flat parallel plates separated by fixed spacing with arrays of individually addressable electrodes fabricated on the bottom plate and a ground electrode as the top plate. When an electrode adjacent to the droplet is turned on, the electrostatic force propels the droplet towards it until it comes to equilibrium at the center of the activated electrode. The actuation force that drives droplet motion depends on the change of the droplet area in contact with the activated electrodes. For DC electric fields the EW force can be approximated as [63], [64]:

$$F_{EW} = \frac{1}{2}V^2 \frac{dA}{dx}\left(\frac{\varepsilon_d \varepsilon_0}{d}\right) \qquad (2.6)$$

The above equation estimates the force as the gradient of the electrostatic energy distribution. Also, the EW actuation force is opposed by contact line friction, viscous drag and wall shear forces [63].
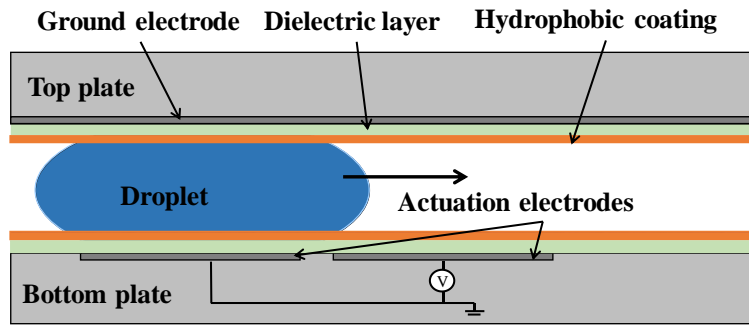
Figure 2.7 Cross section of a parallel plate device used for droplet pumping. Figure 2.7 reprinted with permission from Hale et al. Copyright 2015 IEEE.

2.3 ELECTRIC FIELD ENHANCED CONDENSATION

There have been historical as well as very recent studies on the use of electric fields to enhance condensation. Velkoff and Miller [83] studied electro hydrodynamics (EHD) enhanced condensation in 1965. Subsequent research studied the use of tubes and plates as electrodes to remove vapor or refrigerant condensate off surfaces resulting in heat transfer enhancement [84]–[86]. Studies have analyzed various aspects of EHD including thinning of the condensate film [87], [88], transition from filmwise to pseudo-DWC [89], disruption of the non-condensable gas layer at the liquid-vapor interface and others [86], [90], [91]. On a different note, Butt et al. demonstrated electric-field-induced condensation, where the presence of an electric field reduced saturation vapor pressure [92].

More recently, researchers have studied the influence of an electric field on jumping droplets on superhydrophobic surfaces. As droplets coalesce and leave the superhydrophobic surface, they attain a positive charge due to the electric-double-layer-based charge separation at the interface of the hydrophobic layer and the droplet [93]. The

charged jumping droplets are found to be attracted to the ground or negatively charged electrode and are repelled by the positively charged electrode. This charging behavior occurs because most hydrophobic surfaces have a negative zeta potential. An external electric field can be applied to enhance removal of jumping droplets by counteracting gravitational forces and entrainment forces, preventing droplets from returning to the condensing surface [94]. Experiments showed a 100% increase in heat transfer by preventing droplet return compared to state-of-the-art DWC [95]. Yan et al. [96] showed that by applying a tangential AC electric field of 3-9kV, the jumping frequency was significantly enhanced as compared to that without the electric field; however the tangential droplet growth rate and coalescence was slower. Oh et al. [97], [98] demonstrated the use of electric field controlled jumping droplets for hot spot cooling.

There exist seven studies on the use of EW for condensation enhancement from other research groups. The first study was by Kim et al. [99] and used an overhanging electrode to move droplets on an inclined surface. The electric field was used to overcome the static three-phase contact line friction, and initiate droplet motion. The same group used this concept to drain condensate in heat exchanger evaporators, and showed that the use of EW combined with hydrophobic surfaces can enhance drainage by 3X [100]. It is noted that in both these studies, one of the electrodes was external to the condensing surface.

More recently, Baratian et al. [12] demonstrated EW-enhanced condensation by modifying the standard 'breath figure' condensation droplet arrangement on a surface. They fabricated interdigitated coplanar electrodes by patterning ITO (Indium Tin Oxide) on a glass substrate. Parylene C was used as the dielectric layer and CYTOP as the hydrophobic coating. By using an AC electric field, they were able to change the energy

27

landscape on the surface and modify the distribution of condensed droplets. This study showed that under an electric field, droplets initially aligned parallel to the electrode edges. As they grow, a coalescence cascade sets in to create a monodispersed distribution of droplets that align in the gap between electrodes. By calculating the electrostatic energy profile, they showed that droplets migrate towards the energy minima corresponding to their sizes, which eventually shifts to the center of the electrode gap. All this increases the average droplet size and shifts the distribution of droplet sizes away from classical droplet size distributions. Interestingly, droplet shedding occurred at smaller droplet sizes due to the reduction in contact angle hysteresis. Overall, this study reported an increase in area-averaged droplet size and a 10%-12% reduction in surface coverage.

The same group published another study on droplet shedding under various electrode geometries [13]. They compared droplet shedding radii and frequency on straight interdigitated electrodes and interdigitated electrodes with zigzag edges. For the straight electrodes, the shedding radius decreased with voltage due to the reduction in contact angle hysteresis. However, for the zigzag geometry, droplets accumulated at the apices of the triangles due to electrical trapping. Additionally, the shedding radius increased with voltage as a consequence of the larger electrical trapping force. To overcome this, the voltage was applied intermittently instead of continuously. Coalescence was enhanced with the voltage on, and gravity driven shedding occurred with the voltage off.

A study by Yan et al. [101] showed that the application of a DC electric field increased water shedding by inducing roll-off. However, this study involved condensation of mist droplets from a commercial water mister and cannot be directly compared with other studies on condensation of water vapor which strictly involve condensation via phase

28

change. The same group presented a follow-up study [14] visualizing the droplet size distribution under EW. By using various coplanar electrode designs, they showed that the distribution of droplets deviates from the random distribution seen in classical DWC. When compared to classical droplet size distribution models, a greater number of larger droplets were observed as a result of EW-induced coalescence. Additionally, this study also reported early and more frequent shedding events under an EW field.

More recently, Högnadóttir et al. reported increased droplet coalescence under EW [16]. They applied a low frequency to a range of electrode geometries (electrode:gap width ratios) to identify the configuration that yielded the highest condensation rate. Additionally, this study applied the electric field intermittently, reporting a >50% enhancement in condensation. This highlights the fact that an intermittent field can be more advantageous than a continuous field in terms of removing condensate.

2.4 STATISTICS AND DATA SCIENCE-BASED MODELING OF DROPLET COALESCENCE

Chapter 4 aims to understand the relationships between droplet coalescence and various parameters associated with EW systems. The rationale underlying our approach is that fundamentals-based modeling of droplet coalescence of an ensemble of droplets under an electric field is very challenging owing to the complex physics associated with the underlying phenomena. However, it is relatively easy to get access to large quantities of experimental data on coalescence dynamics based on visualization of droplets. All this data can be analyzed using machine learning techniques to obtain insights into droplet coalescence. This section provides a background on the machine learning algorithms used for the analysis presented in Chapter 4.

Machine learning tools such as image analysis, support vector machines, neural networks etc. have been used in previous microfluidics-focused studies [102]–[104]. Similar tools have also been used for analyzing various heat transfer phenomena as potential replacements for traditional computational techniques. Yang et al. used regression functions, decision trees, random forests and artificial neural network models to predict the interfacial thermal resistance between graphene and hexagonal boron–nitride (hBN) using temperature, coupling strength and in-plane tensile strains data [105]. Zhan et al. used linear regression, Lasso regression and Support Vector regression to model thermal boundary resistance using material properties [106]. Hobold et al. used machine learning visualization and principle component analysis to classify various boiling regimes [102]. Additionally, statistical analysis has also been used to model droplet coalescence in atmospheric sciences [107], [108]. However, there is no prior study on the use of any machine learning technique to study electrically enhanced coalescence of droplets. In Chapter 4, variable selection and regression analysis are used to understand the influence of EW parameters on droplet coalescence dynamics. Some statistical models which are relevant to this analysis are described ahead.

Three variable selection based statistical techniques; Ridge regression, Lasso regression and Random Forest are used (in Chapter 4) to identify the relative influence of the input parameters on the respective output parameters. All these three techniques are supervised learning methods, and are widely used in statistical modeling for feature selection or shrinkage [105]. Ridge regression is an extension of linear regression analysis and imposes a penalty to the expression that minimizes the sum of least squares (which is the cost function associated with linear regression), causing variable shrinkage. The penalty

is imposed to the total size of the coefficients such that more important predictors will have higher coefficients and less important predictors will have lower coefficients, based on the magnitude of the applied penalty [109], [110]. Ridge regression minimizes the cost function as:

$$\sum_{i=1}^{N}\left(y_i - \sum_j x_{ij}\beta_j\right)^2 + \lambda \sum_{j=1}^{p} \beta_j^2 \quad (2.7)$$

where the first term is the cost function associated with least squares, and the second term is the additional penalty term. Here, x includes the set of independent variables and y is the dependent variable to be predicted, λ is the applied penalty which can be optimized. The model solves for the parameter β in order to minimize the cost function.

Another method of variable selection is Lasso regression. Similar to Ridge regression, Lasso regression imposes a penalty term to the sum of squares minimization, where the penalty term takes the form of $\lambda \sum_{j=1}^{p}|\beta_j|$. This penalty term shrinks the unimportant variable coefficients to zero, eliminating them from the model [106], [109], [111] which is a significant benefit of Lasso regression over Ridge regression. This makes Lasso regression an advantageous screening tool to identify the most correlated variable, creating a more sparse problem with fewer coefficients [111]. Additionally, in Lasso regression, the variable selection process is continuous and more stable, making it more computationally feasible for higher dimensional data.

The Random Forest method is widely used in statistical data science regression studies. Random Forests consist of several decision trees which are models that learn to split the dataset into smaller and smaller subsets to predict the target values. During this process, many hyper parameters (such as the number of decision tress in the forest and the number of features considered by each tree when splitting a node) must be optimized in

order to reduce the error between the training and predicted data [105]. Presently, besides optimizing the Random Forest model to minimize the error, the algorithm can also determine the importance of the input features. Feature importance is calculated as the decrease in node impurity weighted by the probability of reaching that node. The node probability is estimated as the ratio of the number of samples that reach the node to the total number of samples. This method identifies the input variables which contribute the most to building the decision trees in the forest; these will also impact the output variables accordingly.

In addition to algorithms that can identify the significant input parameters, it is also important to identify tools to accurately model and predict the relationship between the significant input parameters and output parameters. Chapter 4 involves regression analysis, and we used the Support Vector Regression (SVR) and Kernel Ridge Regression (KRR) methods.

SVR is based on Support Vector Machines (SVM) is a classification method that uses hyperplanes to best separate the features into different domains. Alternatively, SVR is a regression method where, like SVM, bounds are defined within which the error can lie. The goal of SVR is to find these bounds in the form of a function that at most deviates by ε from the target values for all the training data. In this model, ε is the epsilon-tube within which no penalty is associated in the training loss function. Here, ε is the user specified threshold parameter that determines the threshold within which the error can exist. Hence, the goal of this method is to ensure that the errors do not exceed the threshold ε value. A parameter C is defined which is the penalty parameter of the error term. In SVR, the inputs are first nonlinearly mapped into a high dimensional feature space wherein they are

correlated linearly with the output [112]. Such a linear regression in high-dimensional feature space reduces the algorithm complexity, enabling high predictive capabilities of both training and unseen test examples.

KRR is an extension of least square regression which solves overfitting and multicollinearity problems associated with least square methods by integrating Ridge regression and kernel methods [113]. The form of the model is very similar to SVR; however, the loss function uses a squared error. Both SVR and KRR use a kernel function which maps the non-linear data to a higher dimensional linear space to reduce the complexity of solving the problem. Several different kernel functions exist, including linear and polynomial. Another popular kernel function is the radial basis function (rbf) described as [114]:

$$\left(x_i, x_j\right) = \exp\left(-\frac{(x_i-x_j)^T(x_i-x_j)}{2\sigma^2}\right) \qquad (2.8)$$

where x_i and x_j represent the two input vectors and σ is a free parameter which can be expressed as $\gamma = \frac{1}{2\sigma^2}$ such that γ sets the spread of the kernel. These analytical techniques are advantageous to utilize for predictive modeling in complex physical systems with large datasets where analytical or computational predictions are challenging.

Chapter 3: Electrowetting-based enhancement of droplet growth dynamics and heat transfer during humid air condensation[1]

The objective of this task is to study electrowetting (EW)-based enhancement of droplet growth dynamics and heat transfer during humid air condensation. This task describes experiments and analysis to study early-stage droplet growth dynamics, as well as steady state condensation under the influence of an electric field. It is seen that droplet growth is enhanced as the voltage and frequency of AC electric fields is increased, with AC electric fields seen to be more effective than DC electric fields. Droplet roll-off dynamics also depends on the frequency of the AC field. Overall, the electric field alters the droplet size distribution and moves the condensate to more favorable states for removal from the surface. The condensation rate is influenced by the droplet roll-off diameter, frequency of roll-off events, and the interactions of the rolled-off droplets with the remainder of the droplets. An analytical heat transfer model is developed and utilized to relate the measured condensation rate with heat transfer. This model takes into account the fact that this study deals with condensation of humid air, and not pure steam. Overall, this study reports more than 30% enhancement in condensation rates resulting from the applied EW field, which highlights the attractiveness of EW for condensation enhancement.

---

[1] The contents of this chapter have been published in the following journal article: E. D. Wikramanayake and V. Bahadur, "Electrowetting-based enhancement of droplet growth dynamics and heat transfer during humid air condensation," *Int. J. Heat Mass Transf.*, vol. 140, pp. 260–268, 2019. The dissertator is the main contributor of all aspects of this research.

3.1 EXPERIMENTAL SET UP AND PROCEDURE FOR CONDENSATION EXPERIMENTS

Dropwise condensation experiments were conducted on Indium Tin Oxide (ITO) coated glass slides. Photolithography and plasma etching were used to pattern an interdigitated electrode layout (Figure 3.1a), detailed ahead. The substrates were 50mm x 25mm x 1.1mm glass slides with a 120-160 nm thick layer of ITO (Delta Technologies). The slides were patterned via a photolithographic process using the following procedure:

- Substrates were spin coated with the photoresist AZ5209 at 4000 RPM for 45 seconds and soft baked for one minute at 95 °C. This resulted in a 0.9 μm layer of photoresist.

- Substrate was then exposed to UV light through the pattern mask and developed using AZ3000MIF developer to reveal a pattern of exposed ITO and photoresist.

- Exposed ITO was removed by plasma etching (Oxford Instruments Plasma Lab 80) using a mixture of CH_4 and Ar gas.

The two sets of electrodes were connected to the high voltage and ground ends of a signal generator and amplifier, to generate an electric field between adjacent electrodes, as shown in Figure 2.6. The electrode width and gap were 50 μm each. Figure 3.1b shows the cross section of the condensation surface. A 2 μm layer of CYTOP (amorphous hydrophobic fluoropolymer) was spin coated on the surface as the EW dielectric. The dielectric layer is a critical requirement of EW systems, and stores electrostatic energy, which actuates the droplet. The condensing surface was placed (Figure 3.1c) on a liquid nitrogen cold plate (Instec-mK1000 LN2-P), which maintained the surface at 2±1°C, to eliminate ice formation. The entire setup was placed in an environmental chamber (ESPEC Platinous H-series) maintained at 23±2°C and 60±2.5% relative humidity.
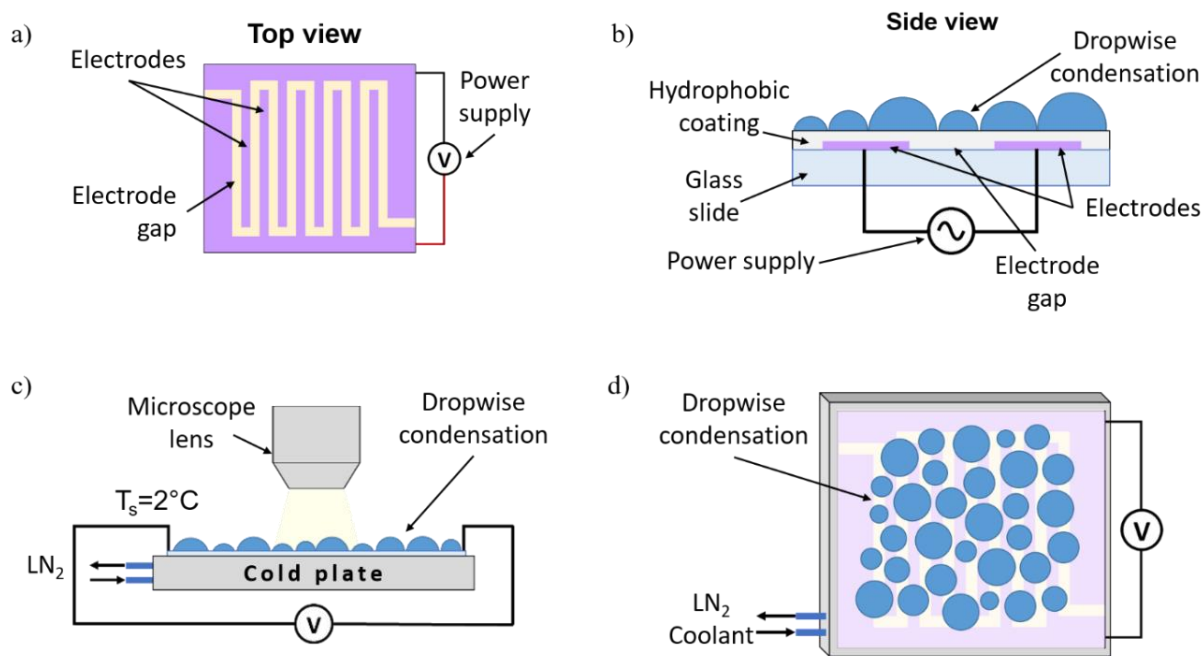
Figure 3.1. Schematic of experimental setup. a) Top view of condensation surface showing interdigitated electrode architecture. b) Cross section of surface showing EW-related details. c) Surface under optical microscope to visualize droplet growth dynamics. d) Vertically oriented surface to study droplet roll-off.

Two types of experiments were presently conducted. The first type of experiments involved visualization of droplet growth dynamics on a horizontal surface (Figure 3.1c). Condensation was prevented on the cold plate (by flowing a stream of nitrogen gas), while the temperature was ramped down. Once the plate reached a steady 2°C, nitrogen flow was turned off, and the EW field was turned on. The electric field remained on for the rest of the experiment. Droplet growth was recorded with a 5X magnification lens of a Nikon Eclipse LV150N optical microscope. Experiments were conducted with 60 V rms and 100

V rms and at AC frequencies of 0 Hz (DC), 1 Hz and 10 kHz. Baseline experiments were conducted without any applied voltage. No experiments were conducted above 100V to avoid breakdown of the dielectric layer. All experiments lasted 30 minutes and capture early-stage dynamics of droplet growth and coalescence.

For the second type of experiments, the surface was oriented vertically (Figure 3.1d) and the experiments were conducted for longer durations. Droplets were seen to grow, coalesce and roll-off with the rolled-off droplets sweeping additional condensate as they left the surface. The amount of condensed water was estimated, and was used to validate the heat transfer model detailed ahead. These experiments were conducted at 100 V rms and at AC frequencies of 1 Hz and 10 kHz.

Post-processing involved using MATLAB to count the number and size of condensed droplets (circle finder image processing script). The software and imaging capabilities allowed the detection of droplets larger than 5 µm. Droplets were assumed to have a spherical cap geometry, with a contact angle of 120° in the absence of an EW field. An EW voltage reduced the contact angle to as low as 90°. It is noted that all reported data in this study is the average of three repetitions.

3.2 EXPERIMENTAL RESULTS: EARLY STAGE DROPLET GROWTH DYNAMICS

This sub-section describes droplet growth dynamics under the influence of an EW field. Figure 3.2 shows snapshots of the droplet size distribution at 10 minutes and 30 minutes for the baseline (no voltage) case, 100 Vrms, 10 kHz case and 100 V DC case. At the beginning, droplets grow post-nucleation by condensation of vapor. Coalescence occurs once the droplets are large enough to contact adjacent droplets[29]. In the absence

of an EW field (Figure 3.2a and d), droplets maintain a self-similar and homogenous random pattern as the average droplet radius increases.
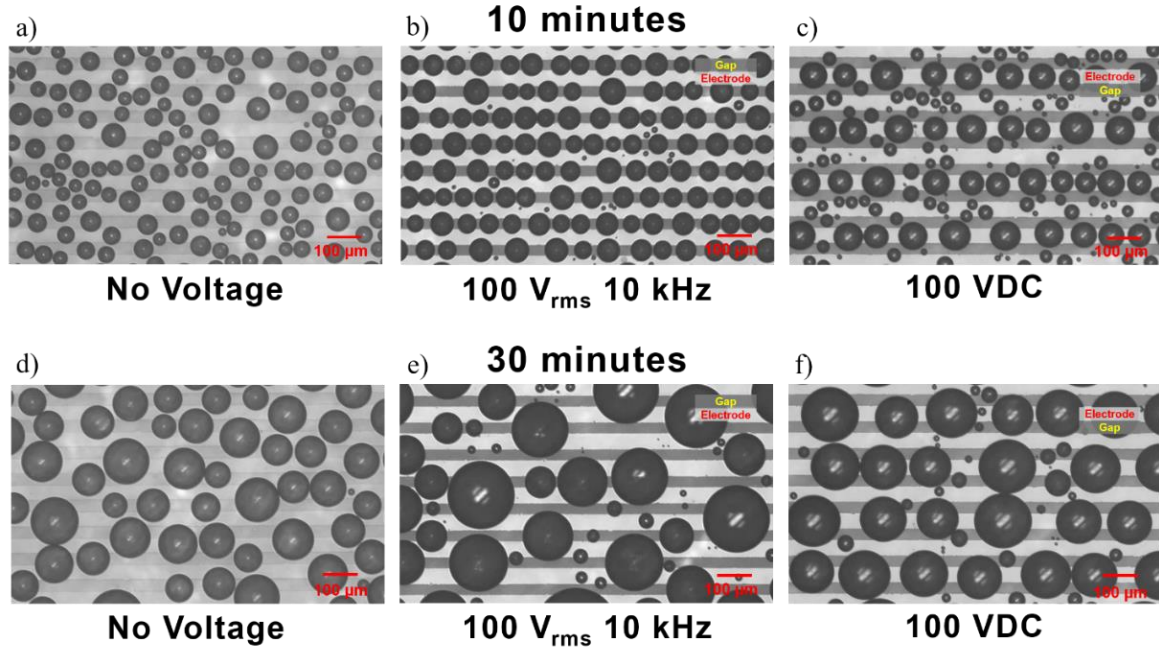
Figure 3.2. Droplet growth patterns under a) no voltage at 10 minutes, b) 100 Vrms, 10 kHz at 10 minutes, c) 100 VDC at 10 minutes, d) no voltage at 30 minutes, e) 100 Vrms, 10 kHz at 30 minutes, f) 100 VDC at 30 minutes. The electrode width (light areas) and gap between electrodes (dark areas) is 50 μm.

It is clearly seen that an electric field alters the droplet distribution. Droplets migrate to locations where the electrostatic energy of the system is minimized; the specific location depends on the electrode and droplet geometry and has been previously studied[17], [63]. Droplets will migrate, when they are large enough (radii> 5-10μm) for the electrostatic force to exceed the resistance due to contact angle hysteresis. Importantly,

as the droplets grow, the electric field is itself modified (droplet is electrically conducting, compared to the insulating dielectric and air), and the minimum energy location can change[12].

Under AC fields, the minimum energy location is the center of the gap between adjacent electrodes[12], [17], [63]. Indeed, Figure 3.2b shows droplets aligning along the electrode gaps (dark areas). As the droplets grow, they will merge, but they still prefer residing in the electrode gaps (Figure 3.2e). Another notable observation is the role of the AC frequency on the type of droplet motion. At 10 kHz, droplets migrate to the minimum energy location, and remain there, with the triple phase line oscillating about the equilibrium position. However, at 1 Hz, droplets respond to the changing voltage by physically translating around their equilibrium positions (in addition to oscillations at the triple phase line). Both types of motions (oscillation, translation) will assist coalescence. Contact-line motion is also favorable from the point of view of reducing pinning at the triple phase line. It is also known that contact angle hysteresis and roll-off angles are lowered with AC electric fields[12], [13].

For the case of a DC field, the droplet arrangement is seen to be the opposite of the AC field. When the droplets are large enough to be affected by the electric field, they migrate to the interface between the ground electrode and the electrode gap (Figure 3.3c). At later instants, these droplets merge and then line up on the ground electrode (Figure 3.3d). The droplets remain here and continue to grow by condensation or coalescence as seen in Figure 3.2c and f. Higher contact line friction (under DC electric fields) prevents them from moving unlike what is observed under AC fields. Figure 3.3 highlights the differences in the coalescence patterns for the AC and DC cases, with droplets clearly

39

lining up in the electrode gap for an AC field (Figure 3.3a and b), and larger (coalesced)

droplets lining up on ground electrodes for the DC field (Figure 3.3c and d).
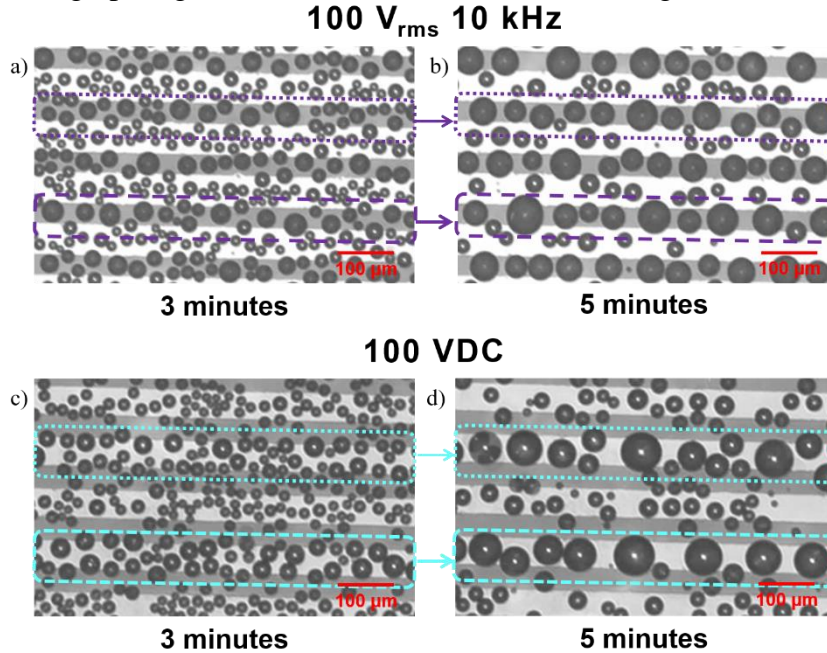
Figure 3.3. Early stage droplet growth dynamics under AC and DC fields a) 100 V rms, 10

kHz at 3 minutes, b) 100 V rms, 10 kHz at 5 minutes c) 100 V DC at 3

minutes, d) 100 V DC at 5 minutes. The dotted lines show droplets aligning

at 3 minutes and then merging to form droplets on the electrode gaps for the

AC case (b) and the ground electrode (d) for the DC case.

The above discussions highlight the dependence of electric field-induced droplet

growth dynamics on the nature of the electric field, electrode architecture and surface

chemistry. Overall, any type of droplet motion is beneficial for promoting coalescence and

enhancing droplet growth. To quantify the overall influence of the electric field on growth

dynamics, the area-weighted average droplet radius, $< R > = \frac{\sum r^3}{\sum r^2}$ was estimated using the

previously described image processing methodology. It is noted that during early stages of growth, the area-weighted average radius for the baseline case is found to be equal to the average radius $\bar{R} = \frac{\sum_i r_i}{n}$, since the droplet size distribution has one dominant average radius.

Figure 3.4 shows the evolution of $< R >$ for applied voltages of 100 V rms (Figure 3.4a) and 60 V rms (Figure 3.4b), with frequencies of 1 Hz, 10 kHz and 0 Hz (DC voltage), along with the baseline case. It is clearly seen that an electric field accelerates growth dynamics, with the differences becoming more pronounced at longer times. At the end of 30 minutes $< R >$ was higher than the baseline by 23% for 60 V (10 kHz) and 35% for 100 V (10 kHz). In general, faster droplet growth was observed for a 10 kHz waveform compared to a 1 Hz waveform. This suggests that the reduced contact angle hysteresis associated with high frequency AC fields[12], [63] makes it easier for droplets to move and coalesce. Very interestingly, the DC electric field showed negligible improvement from the baseline case. For a DC field, the droplets migrate to the minimum energy position and remain there. The absence of oscillatory motion of the contact line reduces the possibility of larger droplets capturing smaller ones. Droplets can only grow by further vapor condensation or via translation of newer droplets, which is also challenging due to the larger hysteresis associated with DC fields. The nature of the electric field lines will also be different for AC versus DC fields. For DC fields, the droplet is considered equipotential, however AC fields will penetrate inside the droplet (this effect becomes more significant with an increase in frequency).
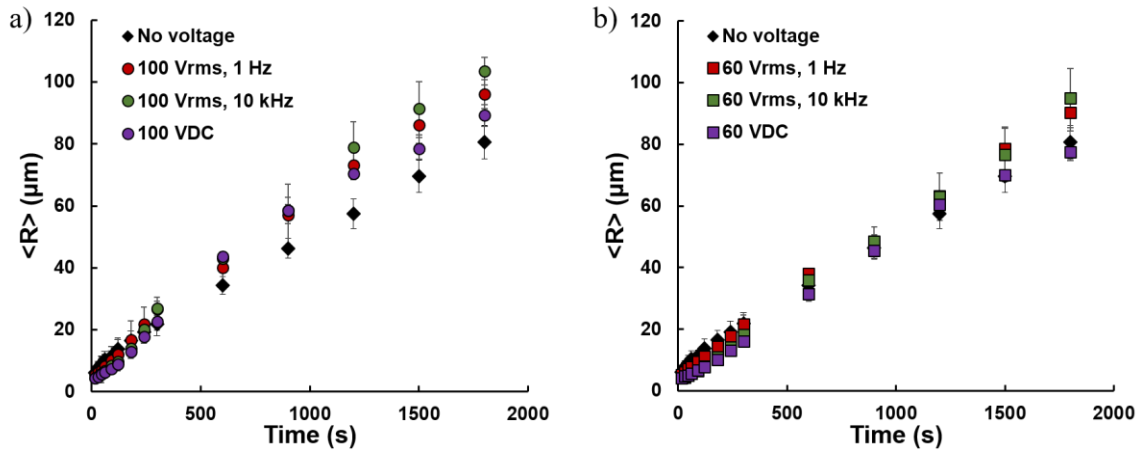
Figure 3.4. Area-weighted average radius of condensed droplets versus time under EW

voltages of a) 100 V and b) 60 V.

The influence of electric fields can also be quantified by analyzing the rate of droplet growth (rate of change of area-averaged radius) $\frac{d<R>}{dt}$. For the baseline case (Figure 3.5), the growth rate of the average radius decreased and plateaued to a constant value, as also reported by Leach et al.[28]. Under AC fields, $\frac{d<R>}{dt}$ shows a decaying oscillatory trend with time. The increase in droplet growth rate, or positive slope regions of this curve are due to electric field-based coalescence cascades. After one cascade droplets settle in their new equilibrium locations, and additional coalescence is prevented for some time, since they are too small to contact the neighboring droplet. Accordingly, the growth rate slows down (negative slope region), with condensation being the growth driver. When these droplets (fed by new condensate) become large enough to 'see' the neighboring droplets, an electric-field based coalescence cascade occurs again (positive slope region). For a DC field, there is an initial increase in growth rate when the influence of an electric field is first seen. However, droplets do not oscillate, and subsequent growth rate reduces as direct

vapor condensation becomes the dominant mechanism, along with the translation of newly nucleated droplets.
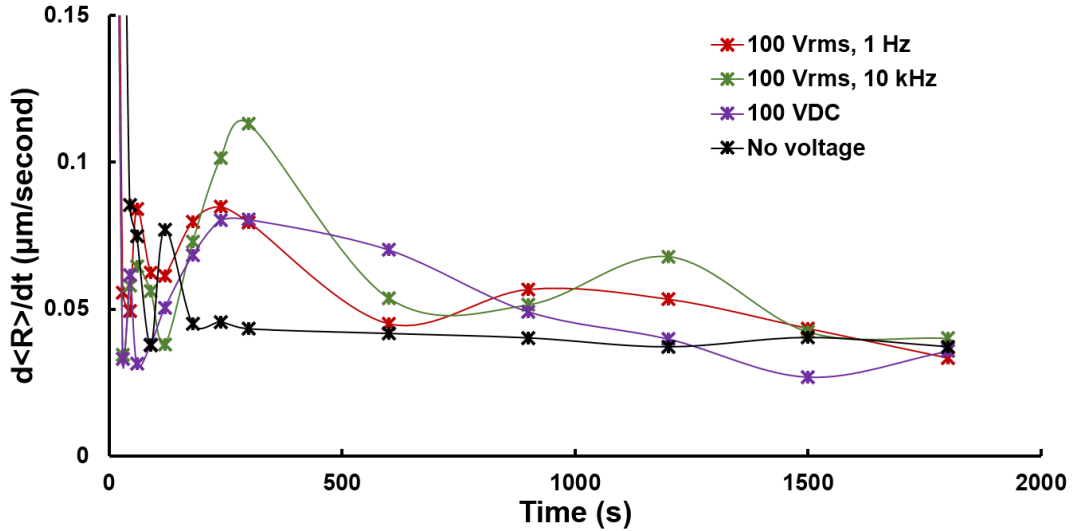
Figure 3.5. Rate of change of area-averaged droplet radius for 100 Vrms AC fields, 100 VDC field and baseline cases.

The impact of electric fields on droplet size distributions after 30 minutes is depicted in Figure 3.6. For the baseline case, a unimodal log-normal distribution is observed which shows a decreasing average radius and a widening droplet size distribution over time until roll-off. Under an electric field, a bi-modal or multi-modal distribution[12] is observed, wherein large droplets are surrounded by many small droplets. Although the distribution shows a smaller number density in the larger size bin, the larger droplets account for a significantly greater volume (volume scales as r^3) percentage of the condensate. At 30 minutes, the total condensate volume in the largest bin (> 100 μm) for 100 V rms AC is 3X greater than in the no voltage case. This again highlights the influence of an electric field in moving condensate to a state favorable for removal.

43
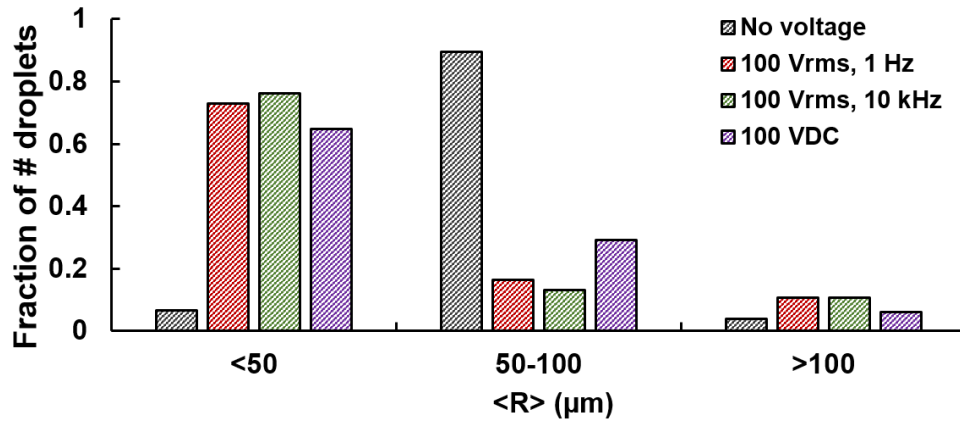
Figure 3.6. Distribution of sizes of droplets condensing under the influence of electric fields after 30 minutes.

Knowledge of droplet size distributions is used to estimate the heat transfer rate, as detailed ahead. Droplet size distribution is also critical to overall enhancement of CHT. While smaller droplets enhance heat transfer locally (lower thermal resistance), larger droplets sweep away significant condensate when they detach, thereby exposing fresh surfaces for nucleation. Additionally, increased condensation rates will lead to more frequent sweeping events. All these considerations are suggestive of an optimum distribution that maximizes heat transfer; this can be explored in a future study.

3.3. EXPERIMENTAL RESULTS: DROPLET ROLL-OFF AND CONDENSATION RATE

This section discusses experiments with vertically oriented surfaces, which allowed the droplets to roll-off. These experiments were run for 3 hours. The condensation rate was obtained by cumulatively adding the mass of droplets rolled-off over time. Droplet mass was estimated using image analysis to find the radius (hence volume) of the spherical cap

shaped droplet after it had rolled off the active condensation area. Figure 3.7a shows the condensation mass flux (average of three experiments) for various cases. Droplet roll-off occurs when the coalesced droplets have reached a critical radius. Thereafter, the condensed mass flux is estimated using the procedure outlined above. For the cases of no voltage and 100 V, 10 kHz, two regions of the curve (Figure 3.7a) can be identified. The initial, higher slope region accounts for a large number of roll-off events taking place between the time corresponding to roll-off of the first droplet, till the time that the entire area is swept at least once. The second region corresponds to a lower and constant slope (constant condensation rate), which is maintained for the remainder of the experiment. This regime is referred to as steady state wherein droplet nucleation, growth, coalescence, and roll-off occur at various places on the surface[28], [115]. This is a quasi-steady process with a stable droplet size distribution and a steady rate of heat transfer. Under these conditions, classical models can be used to characterize the number density of droplets[30]. The slope of the curves in Figure 3.7b can be used to estimate the steady state condensation rate.
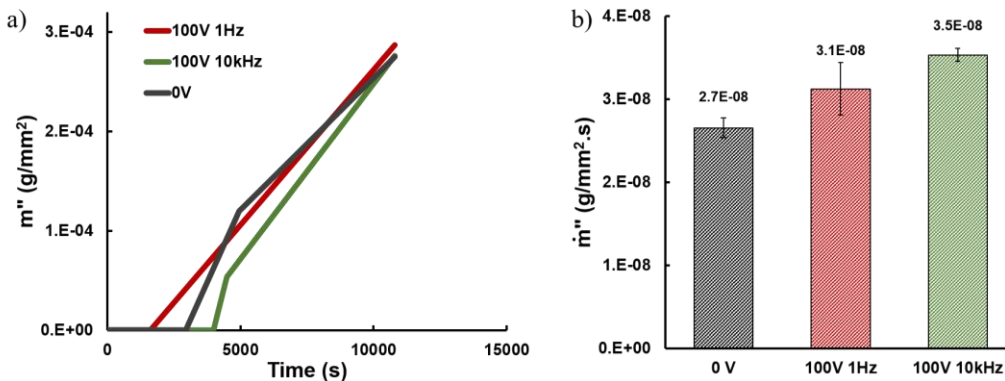
Figure 3.7. a) Condensed mass flux versus time for three cases (no voltage, 100 V, 10 kHz, and 100 V, 1 Hz), and b) Steady state condensation rate for the three cases.

Figure 3.8a compares the roll-off radii for the three cases. Figure 3.8b compares the roll off frequency (the number of roll-off events per unit area) and Figure 3.8c compares the time at which the first roll-off event takes place. For the no voltage case, the first roll-off event occurred at ~60 minutes and the average roll-off radius was 725±89 µm. In this case, droplets maintain a random self-similar pattern (regardless of the size), which results in a stable droplet size distribution. For the 100 V, 10 kHz case, the first roll-off event occurred at ~70 minutes. The average roll-off radius was 730±75 µm. This delayed roll-off is the result of the electric field pinning down droplets [13], noting that the electric field lines will penetrate the droplet. This electrical pinning effect can also be inferred from the low roll-off frequency throughout the experiment. This suggests that periodically turning the electric field off will assist in droplet roll-off. It is also noted that the electrodes were oriented vertically, which significantly reduces the electrostatic resistance to droplet roll-off along the equipotential electrode surface. Also, large droplet roll-off radii are not necessarily detrimental, as the droplet size determines the amount of condensate swept by the droplets as they roll off.
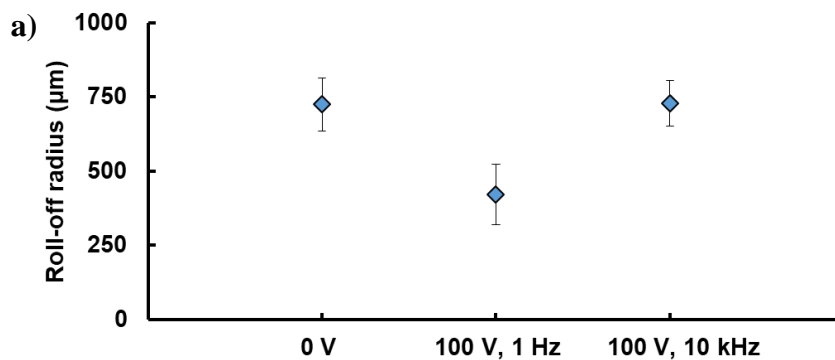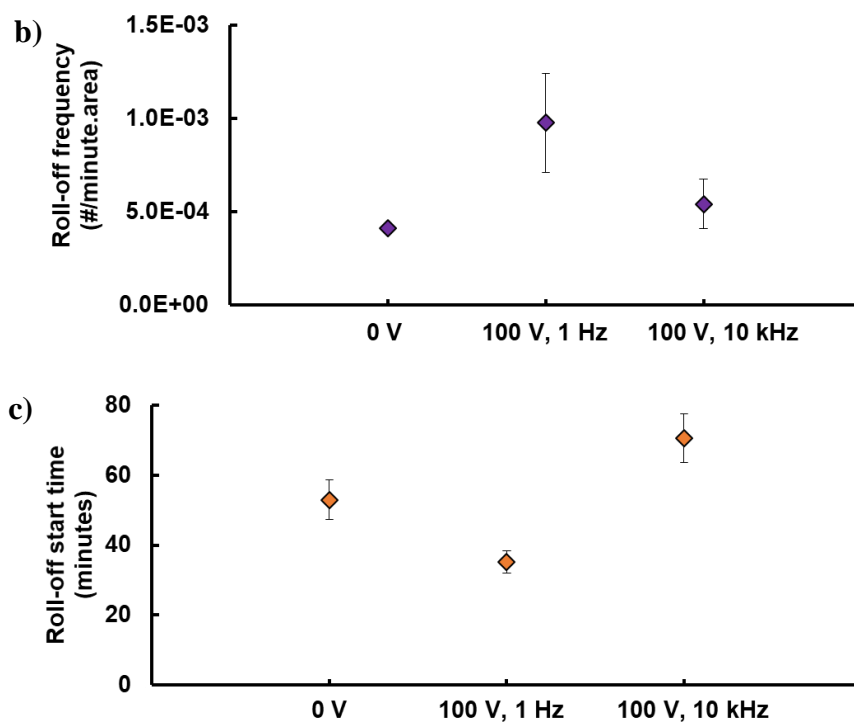
Figure 3.8 Key parameters associated with droplet roll-off under various cases. a) droplet roll-off radius, b) roll-off frequency, c) time for first roll-off event to occur.

The most interesting case is the case of 100 V, 1 Hz. The first roll-off event occurred at ~30 minutes, and the average roll-off radius was 420±100 µm. This is 35% earlier and 42% less than the roll-off start time and average radius of the baseline case, respectively, as seen in Figure 3.8. Additionally, at 100 V, 1 Hz the roll-off radius is >70% smaller than the other cases. The reason for the lower roll-off radius is the reduction in contact angle hysteresis associated with AC electric fields. Droplets are observed to oscillate around their mean position, thereby de-pinning the three-phase contact line from the surface. Additionally, the translation motion of droplets at low frequencies can lead to stochastic

47

coalescence with other droplets, which can trigger roll-off. The high roll-off frequency can be attributed to this phenomenon. As droplets roll off, they gather smaller condensed droplets in their path. Following a roll-off event, smaller droplets which have nucleated in the track exposed by a droplet that rolled-off are observed translating between electrodes under the low frequency AC field. However, although the roll-off frequency is high, the average size of the rolled-off droplet is low, since the droplets have had less time to grow. This results in lower overall condensation rates as compared to the high frequency case. In the high frequency case, the roll-off frequency is low and the roll-off radius is the largest of all the cases studied. These large droplets capture a significant number of smaller droplets on their way down, thereby opening up a large new track for fresh nucleation. Overall, these results demonstrate that condensation need not be maximized by droplets rolling-off rapidly (and at smaller sizes). Condensation also depends on the interactions of the rolling-off droplets with the rest of the droplets.

Figure 3.7b shows the steady state condensation rates for the three cases. The 100 V, 10 kHz case has the highest condensation rate, which is 33% higher than the baseline case. This corresponds to largest droplet roll-off radius and the lowest frequency at which droplets roll-off. The large droplets capture a significant number of smaller droplets on their way down, thereby opening up a large new track for fresh nucleation. For the 100 V, 1 Hz case, the condensation rate is 17% higher than the baseline case. This case is characterized by a relatively low roll-off radius and high frequency of roll-off events. Since the roll-off frequency is high, there is lesser time for droplets to grow. Consequently, smaller droplets are swept away as compared to the 100 V, 10 kHz case. These numbers suggest that overall condensation need not be maximized by droplets rolling-off rapidly

48

and at smaller sizes, but also involves consideration of the interactions of the rolling-off droplets with the rest of the distribution.

3.4 HEAT TRANSFER MODELING

This section details first-order models to relate the measured water collection to condensation heat transfer (CHT). A thermal resistance network-based analytical model is first described, which predicts CHT for a specified droplet size distribution. This model is used to predict the heat transfer for the baseline case with no voltage. Interestingly, it is seen that the predictions from this model reasonably match the predictions of another thermodynamics-based first-order model, which requires the water collection rate as the input (instead of droplet size distribution). This thermodynamics-based model is therefore used to predict CHT under EW fields. It is noted these models constitute the first detailed assessment of the benefits of EW on CHT enhancement.

The thermal resistance network-based heat transfer model is briefly described, and extends the work of Zhoa et al.[49]. Historically, similar models have been used for CHT analysis; however all the studies involved DWC under saturated vapor conditions[5], [32], [116]. In the present experiments with humid air, the thermal resistance network needs to be modified to account for the presence of non-condensable gases. It is well-known that the presence of non-condensables drastically reduces CHT[3], [49], [51]. The thermal resistance network also considers natural convection from the non-wetted area, which is an improvement over existing models which only consider heat transfer through droplets.
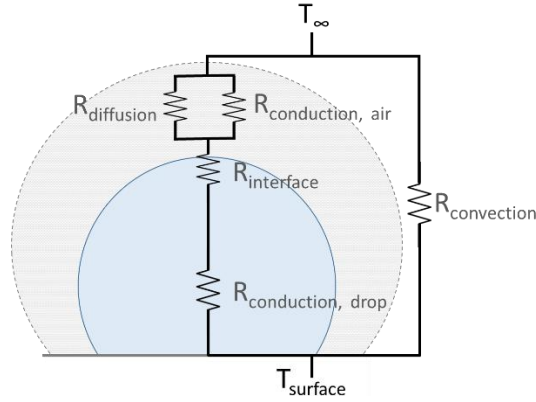
Figure 3.9. Thermal resistance network corresponding to a single droplet and the area surrounding the droplet during dropwise condensation

Figure 3.9 shows the thermal resistance network (corresponding to a single droplet) for DWC in the presence of non-condensables. As water vapor condenses, a layer of non-condensables accumulates at the liquid-vapor interface around the droplet. The water vapor in ambient air diffuses through this boundary layer to reach the droplet, which imposes a conduction resistance through air. This boundary layer offers the largest thermal resistance in the heat transfer network [3], [51], [52]. Zhoa et al.[49] modeled this boundary layer as containing two resistances in parallel which transfer heat from the ambient air at T_∞ to the surface of the droplet at T_i; a similar approach is presently used. The resistance associated with diffusion of vapor through the layer of non-condensables [49] is:

$$R_{diff} = \frac{(T_\infty - T_i)}{\dot{m} h_{fg}} \qquad (3.1)$$

where $\dot{m}$ is the condensation rate based on experimental data, h_{fg} is the latent heat of condensation, and T_i and T_∞ are the interface and ambient temperatures, respectively. The conduction resistance of air [49] is estimated as:

$$R_{cond,air} = \frac{\delta}{k_{air}S(r)} \qquad (3.2)$$

where k_{air} is the thermal conductivity of air and $S(r)$ is the projected area of the droplet. In equation 3.2, δ is the thickness of the boundary layer, which in an unknown. However, by equating the condensation rate to the mass diffusion rate [26], [49], an approximation for δ can be obtained using:

$$\dot{m}'' = -\mathcal{D}Mc\frac{x_i - x_\infty}{\delta} \qquad (3.3)$$

where $\mathcal{D}$ is the diffusion coefficient of water vapor in air, c is the concentration and M is the molecular weight of water. x_∞ is the mole fraction in air, determined by ambient conditions ($x_\infty = RH\frac{P_{sat}}{P_\infty}$, where P_{sat} is the saturation pressure and P_∞ is ambient pressure which is the atmospheric pressure under experimental conditions) . x_i is the mole fraction at the liquid-vapor interface of the droplet determined by the Clausius-Clapeyron Equation 3.4 as:

$$x_i = \exp\left[-\frac{h_{fg}}{R}\left(\frac{1}{T_i} - \frac{1}{T_{boil}}\right)\right] \qquad (3.4)$$

Under these conditions, T_{boil} is the boiling point under atmospheric pressure (P_∞).

Next, the thermal resistance associated with the droplet is considered, based on existing classical droplet thermal resistance models [5], [33], [34]. This network consists of an interface resistance and conduction resistance in series [5], [32], [34], [116]. The interface resistance [32], [33] accounts for the temperature drop at the vapor-liquid interface, and is estimated as:

$$R_{int} = \frac{1}{h_i 2\pi r^2 (1 - \cos\theta)} \qquad (3.5)$$

h_i is the interfacial heat transfer coefficient [5], [33]:

$$h_i = \frac{2\alpha}{2 - \alpha}\frac{1}{\sqrt{2\pi R_g T_s}}\frac{h_{fg}^2}{v_g T_s} \qquad (3.6)$$

where θ is the contact angle and R_g is the specific gas constant. The accommodation coefficient (condensation coefficient), α is the fraction of vapor molecules that move into the liquid droplet during phase change and is found to be in the range of 0.02-0.04 for water [33]. In this work, we use $\alpha = 0.02$ to represent the low humidity conditions of present experiments. Finally, the conduction resistance of the droplets is expressed as [32]:

$$R_{cond,drop} = \frac{\theta}{4\pi k_l r sin\theta} \qquad (3.7)$$

where k_l is the thermal conductivity of water. The overall thermal resistance associated with the droplet can be estimated as:

$$R_{Total}(r) = \left[\frac{1}{R_{diff}} + \frac{1}{R_{cond,air}}\right]^{-1} + R_{int} + R_{cond,drop} \qquad (3.8)$$

The droplet radius dependent heat transfer can then be expressed as:

$$q(r) = \frac{\Delta T}{R_{Total}(r)} \qquad (3.9)$$

where $\Delta T = T_\infty - T_{surface}$. From a knowledge of droplet size distribution and inclusion of natural convection, the overall heat flux can be estimated as [5]:

$$q''_{surface} = \int_{R_{min}}^{R_{max}} q(r)N(r)dr + f_{dry} * h_{air} * (T_\infty - T_s) \qquad (3.10)$$

where the first term on the right is the heat flow through all the droplets. $N(r)$ the number density of droplets at a given time instant. The second term on the right accounts for natural convection through the non-wetted area around the droplet, where f_{dry} is the fraction of dry area and h_{air} is the heat transfer coefficient (method used to estimate h_{air} is described below).

This model predicts a steady-state CHT of 104 W/m^2 for the baseline case, based on the measured droplet size distribution. While this is a low value of flux compared to most studies on condensation, it is noted that this work involves condensation of humid air

and not pure steam (unlike most studies); furthermore, there are no forced convection effects here. The thermal resistance network (Figure 3.9) used in the heat transfer model accounts for heat transfer through the condensed droplets and natural convection in the non-wetted part. The magnitude of various thermal resistances as a function of droplet size is shown in Figure 3.10. The two resistances associated with the droplet are the conduction resistance and the interface resistance. These two resistances are in series and are obtained from classical dropwise condensation heat transfer models [5], [32], [117]. However, since humid air is involved, the resistance network was modified to account for the resistances in the layer of non-condensable gas (NCG) around the droplets [49]. In the NCG layer, the diffusion branch accounts for vapor molecules diffusing through the NCG layer to the droplet. Figure 3.10 shows that the dominant resistance in the network is conduction through air and this resistance determines the overall resistance and the heat transfer. The resistances within the droplet are significantly lower than those in the NCG layer due to the relatively high thermal conductivity of water. This figure also captures the degradation in heat transfer due to the presence of NCGs.
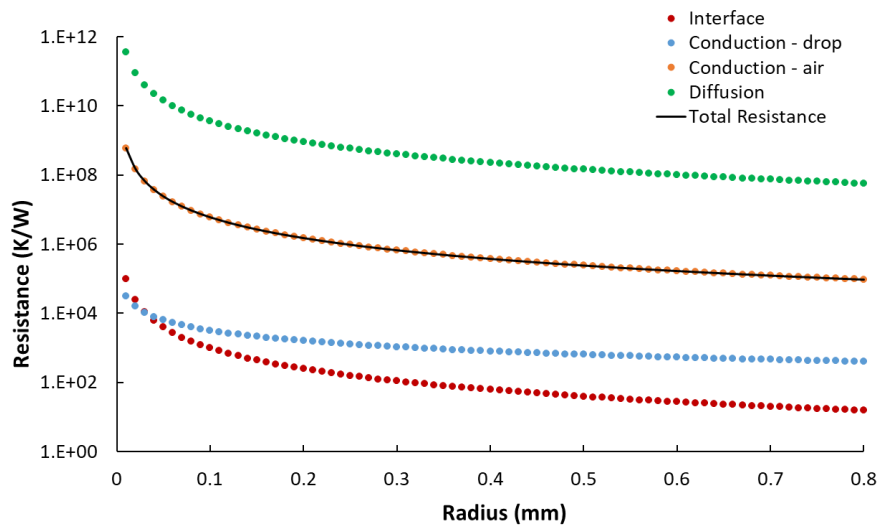
Figure 3.10. Comparison of various thermal resistances in the thermal resistance network.

In addition to the thermal resistance-based analytical model, the heat flux can also be estimated from first-order thermodynamics-based assessments. From the knowledge of the measured condensation rate $\dot{m}"$ and the surface wetted fraction, the overall heat transfer can be estimated as:

$$Q" = \dot{m}"h_{fg} + \dot{m}"C_{p,wv}(T_\infty - T_{dp}) + f_{dry} * h_{air}(T_\infty - T_s) \qquad (3.11)$$

It is noted that a similar approach was used to predict CHT associated with atmospheric water harvesting applications[22]. The first term on the right side in Equation 3.11 accounts for latent heat of condensation h_{fg} (2270 kJ/kg). The second term accounts for sensible cooling of vapor (which eventually condenses) and the third term accounts for natural convection-based heat gain by the dry surface area. $C_{p,wv}$ is the specific heat of vapor, and T_∞ and T_{dp} are the ambient and dew point temperatures, respectively.

The average heat transfer coefficient for the condensing area was estimated by integrating the following expression along the length of the condensing surface[26]:

$$h_{air} = \frac{k_{air}}{L}\left[\frac{g\beta(T_s-T_\infty)}{4v^2}\right]^{\frac{1}{4}} g(Pr) \int_0^L \frac{1}{x^{\frac{1}{4}}} dx \qquad (3.12)$$

where k_{air} is the thermal conductivity of air, g is the acceleration due to gravity, β is the volumetric thermal expansion coefficient, v is the kinematic viscosity, $g(Pr)$ is a function of the Prandtl number (Pr=0.7), $g(Pr) = \frac{0.75Pr^{1/2}}{(0.609+1.221Pr^{1/2}+1.238Pr)^{\frac{1}{4}}}$. This analysis is valid for Rayleigh number range, $Ra = Gr * Pr \approx 10^9$, where the Grashof number is $Gr = \frac{g\beta(T_s-T_\infty)x^3}{v^2}$ [26]. Based on the above description, h_{air} is primarily influenced by the length of the condensing surface and the temperature difference between ambient and the surface.

Comparison of the three terms (latent heat, sensible cooling and natural convection) in Eq. 3.11 shows that the contribution of sensible cooling is negligible. For the baseline case, latent heat and natural convection represent 71% and 29% of the total flux, respectively. The relative contribution of the latent heat term increases with an increase in the condensation rate. For the 100 V, 10 kHz case where the mass flux is highest, latent heat and natural convection show the same breakdown of the total flux as the baseline case.

This thermodynamics-based model (Equation 3.11) predicts a condensation heat flux of 85 W/m^2 for the no voltage case. This is a reasonable match with the prediction of the thermal resistance network-based model (104 W/m^2), considering the simplicity and the significant assumptions involved in the formulation. The thermodynamics-based model requires knowledge only of the condensation rate and the surface wetted fraction which is reported in literature [12], [28], [29]. Using this model for the cases of condensation under EW fields results in heat transfer rates of 102 W/m^2 and 111 W/m^2 for the 100 V, 1Hz and 100 V, 10 kHz cases, respectively. When compared to the baseline case, there is a 21% and 31% enhancement for the 100 V, 1Hz and 100 V, 10 kHz cases, respectively. It is noted that the enhancement in the condensation rate is different from the enhancement in condensation heat flux. This difference is due to the natural convection term in condensation heat transfer, which makes the relationship between CHT and condensation rate non-linear.

3.5 CONCLUSIONS

This study shows that electric fields can significantly influence coalescence and growth dynamics during condensation of humid air. Enhancement is controlled by factors such as

the magnitude and frequency of the applied waveform and the electrode architecture. It is seen that AC fields promote greater coalescence than DC fields, with higher frequencies increasing droplet growth rate. The roll-off dynamics is also altered by the electric fields, and it is possible to control the roll-off size and frequency by controlling the applied waveform. Total condensate removal depends on the size and frequency of droplets rolling off, and also on the amount of liquid captured by the droplet as it departs. Condensate removal enhances heat transfer; heat transfer enhancement of up to 31% was observed in this study. In conclusion, this chapter sets the foundations for EW-based enhancement of droplet growth dynamics and heat transfer during humid air condensation.

Chapter 4: Statistical Modeling of Electrowetting-Induced Droplet Coalescence[2]

As clearly seen in the previous chapter, droplet coalescence is a very important parameter associated with dropwise condensation (DWC). In general, coalescence of droplets is a complex microfluidic phenomenon governed by various interactions occurring at the three-phase contact line and various interfaces. When droplets coalesce, initially a liquid bridge forms between the droplets, followed by the final droplet forming at the center of mass of the original droplets [28], [35]. Studies show that during this process, contact line pinning and viscous dissipation influence the receding contact angle dynamics more strongly than advancing contact line dynamics [36]. Also, the two merging droplets leave behind fresh dry area for nucleation to occur. Modeling the physics associated with all these interactions is very challenging. The challenges are significantly amplified when condensation is influence by EW, as the nature of the electric field will also come in play. Analytical or computational predictions of EW-accelerated coalescence are challenging and of limited use due to limitations in current understanding of the underlying physics and lack of knowledge of parameters to accurately model phenomena occurring at the three-phase line.

In view of the above challenges, the work described in this chapter uses experiments coupled with statistical modeling to study EW-accelerated droplet coalescence. In particular, a parametric study is conducted to understand the influence of

---

[2] The contents of this chapter have been published in the following journal article: E. D. Wikramanayake and V. Bahadur, "Statistical modeling of electrowetting-induced droplet coalescence for condensation applications," *Colloids and Surfaces A*, 2020. The dissertator is the main contributor of all aspects of this research.

three important parameters on EW-accelerated droplet coalescence: applied voltage, frequency of the AC EW field and electrode geometry. We experimentally quantify the change in droplet size distribution upon the application of an electric field, and analyze the results using multiple statistical techniques to quantify the influence of these parameters on droplet coalescence. This approach thus leverages the large amount of data (via tracking of multiple droplets) available in condensation experiments, and uses machine learning-based approaches to develop statistical predictive models, which are grounded in EW physics.

The novelty and intellectual merit of this work is briefly summarized ahead. As background, there are very few studies on droplet dynamics during EW-influenced condensation [12]–[16]. Machine learning tools such as image analysis, support vector machines, neural networks etc. have been used in studies on various microfluidic applications [102]–[104], [106]. Statistical analysis has also been used to model droplet coalescence in atmospheric sciences [107], [108]. However, there is no prior study on the use of any machine learning technique to study electrically enhanced coalescence of droplets. This study uses machine learning-based statistical tools to understand the influence of EW parameters on droplet coalescence dynamics. We use the predictions from the statistical models to propose a reference tool to predict changes in droplet size distribution based on the applied electric field. We note that while the analysis is conducted for a specific EW configuration, the conclusions and the current approach (experimental data-based statistical modeling) can be adopted to a wide variety of configurations.

4.1 EXPERIMENTAL PROCEDURES

Indium Tin Oxide (ITO) coated glass slides were used as the substrates for fabricating EW devices using the procedure described in Chapter 3. Standard photolithography and plasma etching processes were used to pattern an interdigitated electrode layout (Figure 4.1a). A co-planar electrode geometry with interdigitated electrodes stripes was used, with the two sets of electrodes located adjacent to each other (Figure 4.1a). The two sets of electrodes were connected to the high voltage and ground ends of a signal generator and amplifier to generate an electric field in the gap between adjacent electrodes (Figure 2.6). Figure 4.1b shows the cross section of the condensation surface. A 5 µm layer of SU-8 2005 was spin-coated on the entire surface as the EW dielectric. This dielectric layer is critical to the performance of EW systems, as it stores the electrostatic energy for droplet actuation. Finally, a 100 nm layer of Teflon was spin-coated to act as the hydrophobic layer.

Next, the experimental procedure is briefly described. It is noted that the primary objective of this study is to investigate the influence of key EW parameters on coalescence of droplets (and not roll-off). The starting ensemble of droplets (to be coalesced) was obtained by spraying water using a commercial room humidifier on horizontally oriented surfaces. Droplet size distributions obtained via this procedure were reasonably consistent in multiple repetitions, and the mean droplet size of the initial distribution was 79 µm ± 9 µm. It is striking to observe that the obtained droplet size distribution is similar to that obtained in classical dropwise condensation experiments [118]. This finding justifies the utility of the present approach for modeling coalescence in dropwise condensation situations. This approach also enables the collection of large data sets for statistical

59

analysis, noting that dropwise condensation experiments would involve much longer durations, and are complicated to conduct.

Post droplet-deposition, the surface was continuously visualized using the 5X magnification lens of a Nikon Eclipse LV150N optical microscope. The EW field was then turned on for 15 seconds, during which droplet coalescence dynamics were recorded at 100 fps. It is shown subsequently, that 15 seconds is long enough for all coalescence events to be completed. The droplet size distribution before and after the application of an EW field was compared to quantify the extent of coalescence. Post-processing involved using a MATLAB code to count the number and size of droplets on the surface (circle finder image processing script). The current software and imaging capabilities allowed the detection of droplets as small as 5 µm. Droplets were assumed to have a spherical cap geometry, with a contact angle of 120° in the absence of an EW field. Droplet radii before and after the application of voltage were calculated and used in the statistical analysis.

Next, the three experimental parameters varied in this study are briefly described. Firstly, three different electrode geometries were characterized with electrode widths of 50 µm, 100 µm and 200 µm; spacing between adjacent electrodes was maintained at 50 µm in all devices. The electrode:electrode gap ratios were thus 1, 2 and 4. These geometrical parameters influence the inter-electrode field and the penetration height of the electric field outside the surface. The second parameter varied was the applied voltage. Experiments were conducted at three different voltages (100 V, 200 V, 300 V). These voltages were higher than the threshold voltage for EW actuation, but less than the saturation voltage, as observed from the EW curve (Figure 4.9). The third parameter varied was the frequency of the applied AC waveform. Experiments were conducted at 1 Hz, 10 Hz, 50 Hz, and 1 kHz

as they capture various types of droplet motion (ranging from translation of droplets to shape variation). It is noted that all experiments were repeated 10 times. Overall, this procedure highlights the experimental rigor involved in this study, and the efforts to get sufficient data for meaningful statistical analysis.
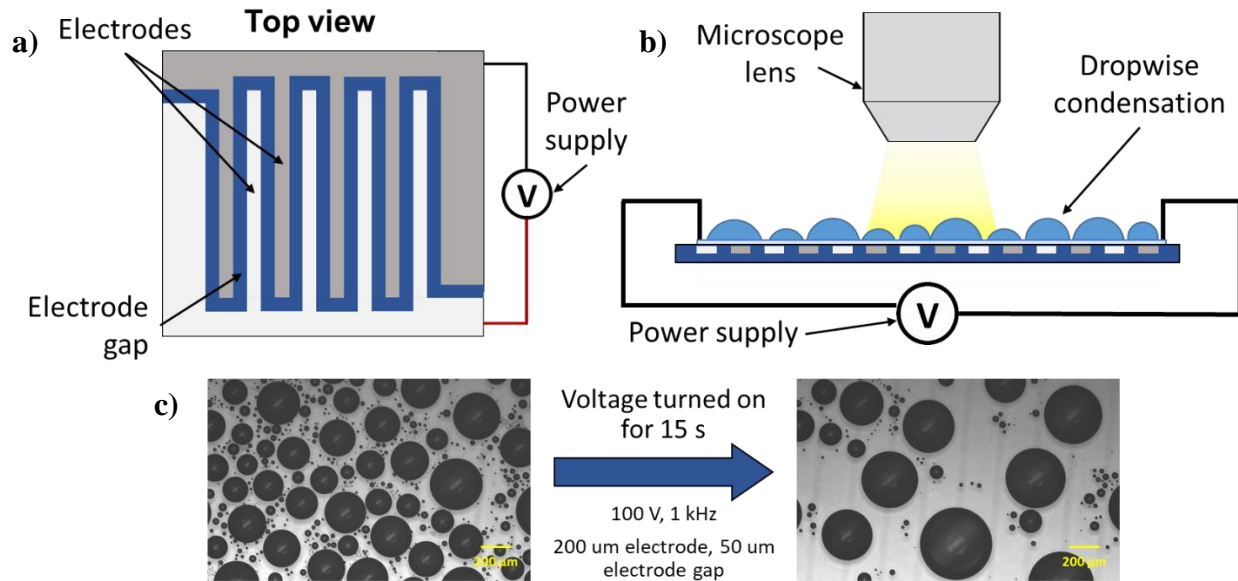
Figure 4.1. Schematic showing the arrangement of interdigitated electrodes (high voltage electrodes in white and ground electrodes in dark grey). (b) Cross section of device with droplets on top. (c) Droplet coalescence due to the influence of an EW field applied for 15 seconds.

4.2 DESCRIPTION OF STATISTICAL ANALYSIS-BASED MODELING APPROACH

The statistical analysis techniques utilized in this study have been briefly described in Sections 2.4. Three statistical techniques (Ridge regression, Lasso regression and Random Forest) were used to analyze the resulting data sets, and to identify the relative

influence of the three input parameters on droplet coalescence. After identifying the significant input parameters (geometry and voltage, as described ahead), the next step in the present work was to select a tool to accurately model and predict the relationship between the significant input parameters and output parameters. Since this study was about regression analysis, we used the Support Vector Regression (SVR) and Kernel Ridge Regression (KRR) methods.

The goal of this study was to identify the relative influence of three input parameters on droplet coalescence; this was achieved by estimating two coalescence-related parameters before and after the application of an EW field. The first parameter is the ratio of the area-averaged radius $< \hat{R} > = \frac{\sum r^3}{\sum r^2}$, after and before the application of the EW field. The second parameter is the ratio of the reduction in the wetted area to the initial wetted area. The wetted area is the fraction of the surface covered by liquid, and will reduce with increasing coalescence. Both these parameters (also referred to as output variables in the model) were estimated via image analysis after every experiment.

The data analysis methodology adopted in this Chapter involved collecting the training and testing data and then preparing the data set by removing any obvious outliers. The data was then scaled linearly before using it in modeling algorithms. For variable selection a model parametric sweep was conducted to identify the best model hyperparameters to minimize the error between the training and testing data [112]. The algorithms used have been detailed in section 2.4. Once the optimized hyperparameters were selected, k-fold cross validation (where k=10) was conducted such that the average absolute error was minimized and the correlation coefficient was enhanced [106], [113]. The training and testing data were compared so as to minimize the root-mean-square error

62

(RMSE) and maximize the coefficient of determination (R^2). It is noted that all the statistical analysis conducted in this work was done in Python.

4.3 RESULTS

The first step in our analysis involved eliminating the possibility of multi-collinearity between input descriptors. A Pearson's coefficient correlation was used to compare the correlation coefficients between the input and output variables. The three input variables (voltage (V), frequency (f) and electrode width (e)) can be captured by three non-dimensional numbers: i) electrowetting number $\zeta = \frac{\varepsilon V^2}{2\gamma d}$, ii) dimensionless relaxation time $\tau = \frac{\sigma/\varepsilon}{\omega}$ ($\omega = 2\pi f$), and iii) geometry ratio $L = \frac{width_{electrode}}{width_{electrode\ gap}} = \frac{e}{g}$. Here $\varepsilon = \varepsilon_d \varepsilon_0$, where ε_d is the electrical permittivity of the dielectric, ε_0 is the electrical permittivity of vacuum, γ is the liquid-vapor surface tension, d is the dielectric layer thickness, σ is the electrical conductivity, e is the electrode width and g is the spacing between the electrodes. The two output variables are the area-weighted radius enhancement ratio $R = \frac{\hat{R}_f}{\hat{R}_i}$ and the normalized reduction in wetted area $A = \frac{A_{wetted,i} - A_{wetted,f}}{A_{wetted,i}}$. Figure 4.2 shows that all the input descriptors have very low statistical correlation coefficients between each other, indicating that they are independent of each other and that there is no multicollinearity between these variables. Additionally, higher correlation coefficients are seen between two input variables (ζ and L) and the output variables.
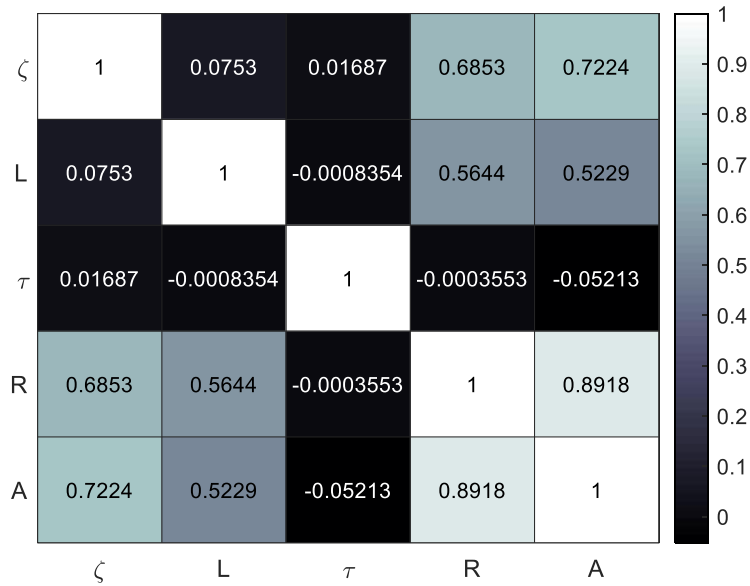
Figure 4.2. Heat map showing Pearson's correlation coefficients between the three input variables (ζ (V), L (e), τ (f)) and the two output variables, R and A.

The next step in the analysis was parameter selection where parameter shrinkage was used to identify the input parameters which dominantly influence the output parameters during droplet coalescence. This was implemented by employing the variable selection methods described in section 2.4; Ridge regression, Lasso regression and Random Forest importance selection. During this analysis the three non-dimensional variables were analyzed against the output variables and the corresponding coefficients were compared. Figure 4.3 shows that coefficients from both regression methods and the Random Forest importance assign high significance to $\zeta(V)$ and $L(e)$, indicating that both these parameters strongly contribute to the change in radius and wetted area. The radius ratio is found to be most dependent on $\zeta(V)$ and $L(e)$, which have ~50% and ~40% Random Forest

importance, respectively. Similarly, the reduction in wetted area also shows strong dependence on $\zeta(V)$ and $L(e)$. In this case, $\zeta(V)$ has a Random Forest importance of ~65% indicating the change in wetted area most strongly depends on the applied voltage, followed by the electrode geometry, $L(e)$, which has an importance of ~35%. Importantly, Figure 4.3 shows that the radius ratio and reduction in wetted area are independent of $\tau(f)$, as the corresponding correlation coefficients are negligible. The correlation coefficients for $\zeta(V)$ and $L(e)$ are ~10X greater than that of $\tau(f)$ for change in radius. Lasso regression completely eliminates $\tau(f)$ as a dependent variable for the change in wetted area. Similar results are seen in the Random Forest classification where frequency dependence is given <10% of the overall importance for both output parameters.
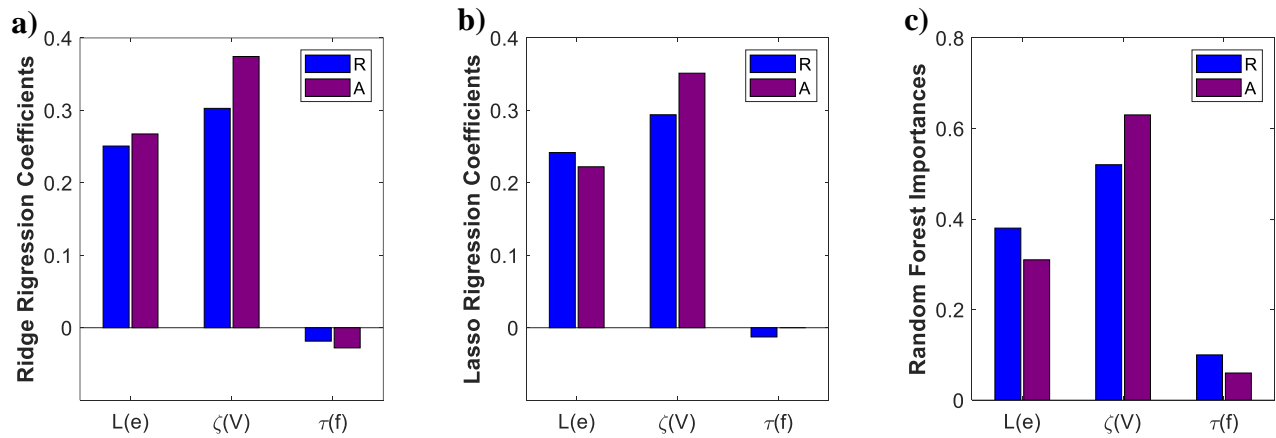
Figure 4.3. Parameter selection and shrinkage conducted via three different methods: a) Ridge regression coefficients, b) Lasso regression coefficients and c) Random Forest importance. Blue and purple bars indicate coefficients associated with the radius ratio and change in the wetted area, respectively.

A key conclusion from Figure 4.3 is that the AC frequency does not influence coalescence dynamics significantly (at least not in the currently used frequency range of 1 Hz to 1 kHz, which is widely used in AC EW experiments). Such conclusions are challenging to arrive at from physics-based models, which would need to account for complex phenomena such as contact angle hysteresis and the electromechanical response of a liquid to a time varying electric field. This finding is also challenging to predict from high speed visualization of droplets. Indeed, Chapter 3[15] showed that the AC frequency strongly influences the nature of droplet motion (translation versus shape oscillation), as well as the orientation of droplets on the electrodes.

The physics underlying the predicted frequency-invariance of coalescence dynamics can be better inferred by analyzing the temporal occurrence of coalescence events. Droplet coalescence is not a continuous process as clearly identified in our previous study on dropwise condensation [15]. Instead coalescence is observed to occur in bursts (reported later in this chapter), with a large number of coalescence events occurring in a very short time interval. Post coalescence, droplets will grow via additional condensation (as observed in previous studies [13], [15], [16]), leading to another 'coalescence cascade' at a later time instant. Such periodic coalescence cascades will not occur in the current Chapter, and only a single coalescence cascade is observed and studied (Figure 4.8). Coalescence parameters R and A depend on this cascade phenomena, which in turn depends on the applied voltage and device geometry, but not significantly on the AC frequency. In summary, the current findings indicate that while the AC frequency will influence the motion of individual droplets, it does not influence the collective coalescence dynamics of an ensemble of droplets.

66

It is noted that this finding of droplet coalescence being AC frequency-independent, underscores the importance of statistical analysis for such complex multi-physics problems. The applied voltage and electrode geometry are two parameters which strongly influence droplet coalescence dynamics. Additionally, this conclusion might not be applicable to droplet shed-off (which is not the focus of the current study), but only for coalescence.

Based on the findings of the variable shrinkage analysis, we next develop a model to predict the radius enhancement ratio R and normalized reduction in wetted area A, as a function of the applied voltage (V) and geometry (electrode width e). Both these parameters can be combined into a parameter similar to the EW number [17], but with the capacitance term modified to incorporate the electrode geometry. The modified, non-dimensional EW number which includes the voltage and the electrode geometry takes the form:

$$\eta(V, e) = \frac{C/w}{\gamma_{lv}} V^2 \qquad (4.1)$$

where C/w is the capacitance per unit width. For the present co-planar electrode geometry, the capacitance can be estimated as [79]:

$$C/w = \frac{2\varepsilon_0 \varepsilon_d l}{\pi A} ln \left[\left(1 + \frac{e}{g}\right) + \sqrt{\left(1 + \frac{e}{g}\right)^2 - 1} \right] \qquad (4.2)$$

Next, a statistical and data science-based model to predict the relationship between R and A versus $\eta(V, e)$, is developed. Since this is a regression-based analysis, the regression models SVR and KKR, described in Section 2.4, are used to compare the predicted values with experimental data. As an additional validation, we also consider the mean and standard deviation of each set of experiments, independent of the frequency, by fitting a probability density function (PDF) to the respective data sets. This step is

important as the data has scatter, especially at larger values of $\eta(V, e)$. The error associated with the statistical models is detailed in Table 4.1 and **Table 4.2: continued next page**

Table 4.2 for the radius enhancement ratio (R) and normalized reduction in wetted area ratio (A), respectively. The predictive accuracy of each model is evaluated by comparing the RMSE and R^2 values between the predicted and experimental data, with models with low RMSE and higher R^2 values representing a more favorable match.

Table 4.1 shows the predictive accuracy of each model and the optimized hyperparameters used in the models to obtain the least error between the experimental and model data. Based on the results for radius enhancement ratio as a function of $\eta(V, e)$ (Table 4.1), the first important observation is that the data follows a linear trend. This is concluded because the linear regression fit shows higher accuracy when compared to the polynomial curve fits. Following this observation, the linear kernel and the rbf kernel are used in the statistical models. When comparing the predictive accuracy of the two kernel methods, the linear kernel shows a lower RMSE and higher R^2 for both methods, implying that the linear kernel can more accurately capture the trend between $\eta(V, e)$ and R. The rbf kernel models attempt to follow the highest probability density in the data at each point with respect to $\eta(V, e)$, and can compromise the accuracy with the entire data set. Additionally, the ε value for the linear fit is several orders of magnitude less than the optimized rbf model indicating that the margin within which error can exist is much less. In the KRR model small positive values of α improve the conditioning of the problem and reduce the variance of the estimates. Overall, *the lowest RMSE and highest accuracy corresponds to the SVR model with the linear kernel*, which shows the best match with experimental data.

	Optimized hyperparameters	RMSE	R^2
Linear Regression		1.14	0.72
Poly. Reg, degree 2		1.25	0.69
Poly. Reg, degree 3		1.48	0.63
SVR - Linear	ε: 1e-5, C: 1e3	1.12	0.72
SVR - RBF	ε: 1, C: 125	1.89	0.53
KRR - Linear	α: 10, γ: 1	1.31	0.73
KRR - RBF	α: 10, γ: 0.5	1.56	0.63

Table 4.1.Compilation of errors (in the form of RMS and R^2 values) for various models predicting the radius enhancement ratio of coalescing droplets. The table also includes optimized hyperparameters that result in the best fit between model and data.

Based on the results for normalized reduction in wetted area as a function of $\eta(V, e)$ (**Table 4.2: continued next page**

Table 4.2), it is seen that 2nd and 3rd degree polynomial curves are a better fit compared to a linear model (based on the resulting RMSE and R^2 values). Polynomial fits with greater than 3rd order did not show any improvement in accuracy. Hence, the statistical models compare the rbf kernels with 2nd and 3rd degree polynomial kernels. When comparing the predictive accuracy of the two statistical models, **Table 4.2: continued next page**

Table 4.2 shows that KRR performs significantly better than the SVR model. Although the SVR model used with the rbf kernel has a low RMSE, the two polynomial

kernels show poor agreement with the experimental data. Alternatively, the KRR model shows good accuracy with low RMSE and high R^2 values for all kernel types. *The best predictability is seen with the KRR model using the 2nd degree polynomial kernel.* Overall, the rbf kernels perform well with both models, however, the KRR model shows the most consistent predictive accuracy for different kernel types. It is important to note that errors associated with linear regression and polynomial regression (degree 2) for radius enhancement ratio and wetted are reduction, respectively, are comparable to the machine learning algorithms that give the greatest predictive accuracy. This indicates that although using machine learning tools provide insight into modeling these coalescence systems, similar analysis can be conducted using linear regression and polynomial regression.

	Optimized hyperparameters	RMSE	R^2
Linear Regression		0.018	0.65
Poly Reg, degree 2		0.014	0.73
Poly Reg, degree 3		0.014	0.71
SVR - RBF	ε: 0.1, C: 5	0.019	0.61
SVR - Poly Reg, degree 2	ε: 10, C: 0.01	0.055	0.36
SVR - Poly Reg, degree 3	ε: 50, C: 0.01	0.055	0.36
KRR - RBF	α: 2.5, γ: 0.25	0.014	0.71
KRR - Poly Reg, degree 2	α: 500, γ: 50000	0.015	0.74
KRR - Poly Reg, degree 3	α: 5, γ: 5	0.014	0.72

Table 4.2: continued next page

Table 4.2. Compilation of errors (in the form of RMS and R^2 values) for various models predicting the wetted area reduction ratio of coalescing droplets. The table also includes optimized hyperparameters that result in the best fit between model and data.

Figure 4.4 shows the experimental data points, mean (μ) values from experimental data, and the model predictions for R as a function of $\eta(V,e)$. Similar to results in Table 4.1, the model agrees best with a linear trend in the data, whereas the polynomial curve fit deviates from the data set. Both models with the linear kernel follow the data trend well; however, a deviation is seen with the SVR model using the rbf kernel. The SVR model with the linear regression kernel (Figure 4.4d) predicts the linear trend in the data reasonably well. Extrapolating the model to $\eta(V,e) = 0$ (no electric field) yields $R \sim 1$ implying no change in droplet radii (as expected).

a)   b)   c)
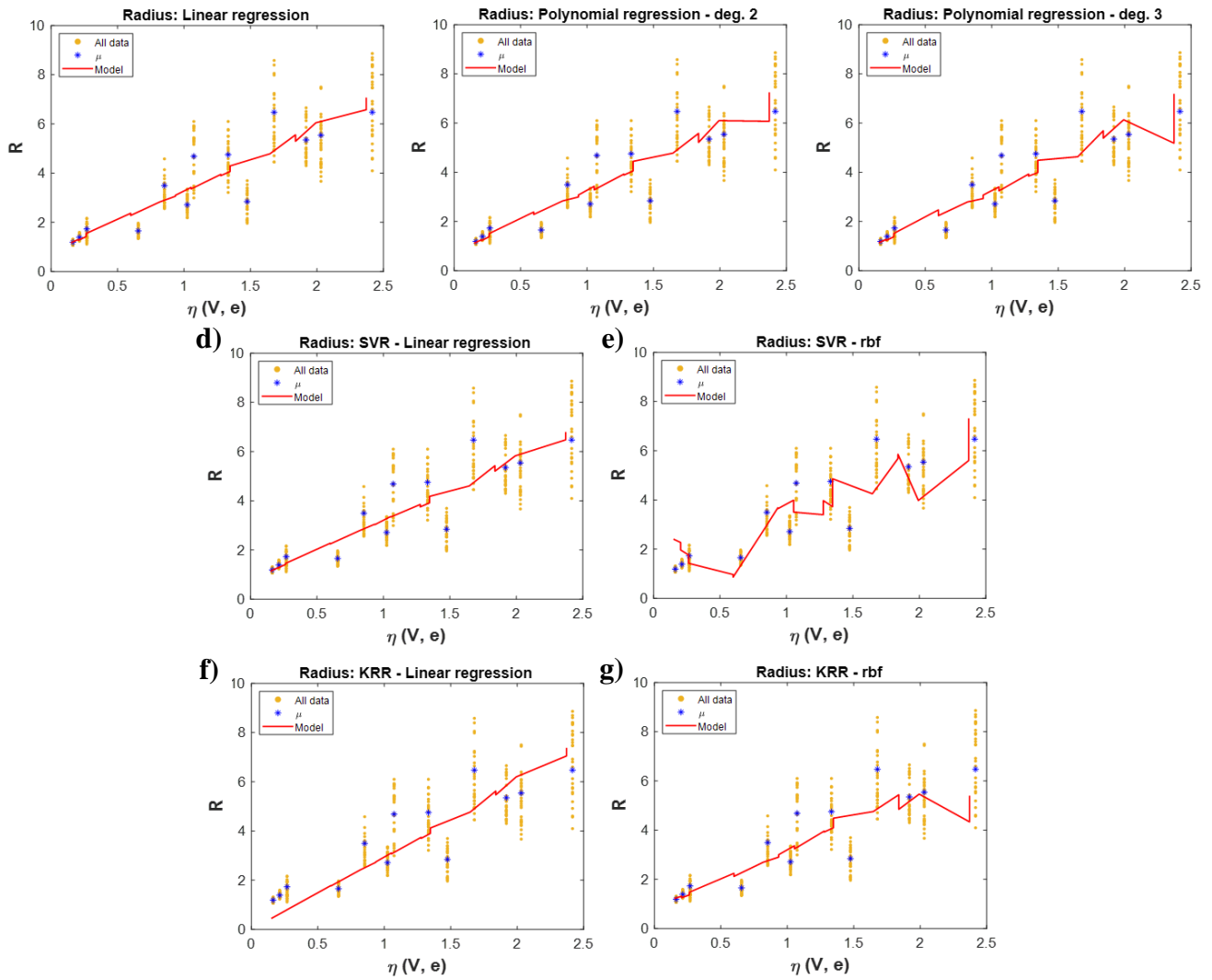
Figure 4.4. Comparing experimental data (yellow), mean values of experimental data (blue) and statistical model predictions (red) for R versus $\boldsymbol{\eta}(\boldsymbol{V}, \boldsymbol{e})$ using a) linear regression curve fit, b) 2nd order polynomial regression curve fit, c) 3rd order polynomial curve fit, d) SVR with linear kernel, e) SVR with rbf kernel, f) KRR with linear kernel, g) KRR with rbf kernel.

Figure 4.5 shows the experimental data points, mean values (μ) from experimental data set and the model predictions for A as a function of $\eta(V, e)$. All models (except the SVR model with the polynomial fits) match well with the experimental data. All the KRR models match well with the dome shaped curve which peaks at $\eta(V, e) \sim 1.75$. From these models, the experimental data for normalized reduction in wetted area compared to the KRR with second order polynomial kernel (Figure 4.5h) show a good match between model and experiments, as captured by the low RMSE and high R^2 values. Again, extrapolating this model to $\eta(V, e) = 0$ shows that $A \sim 0$ which is expected.
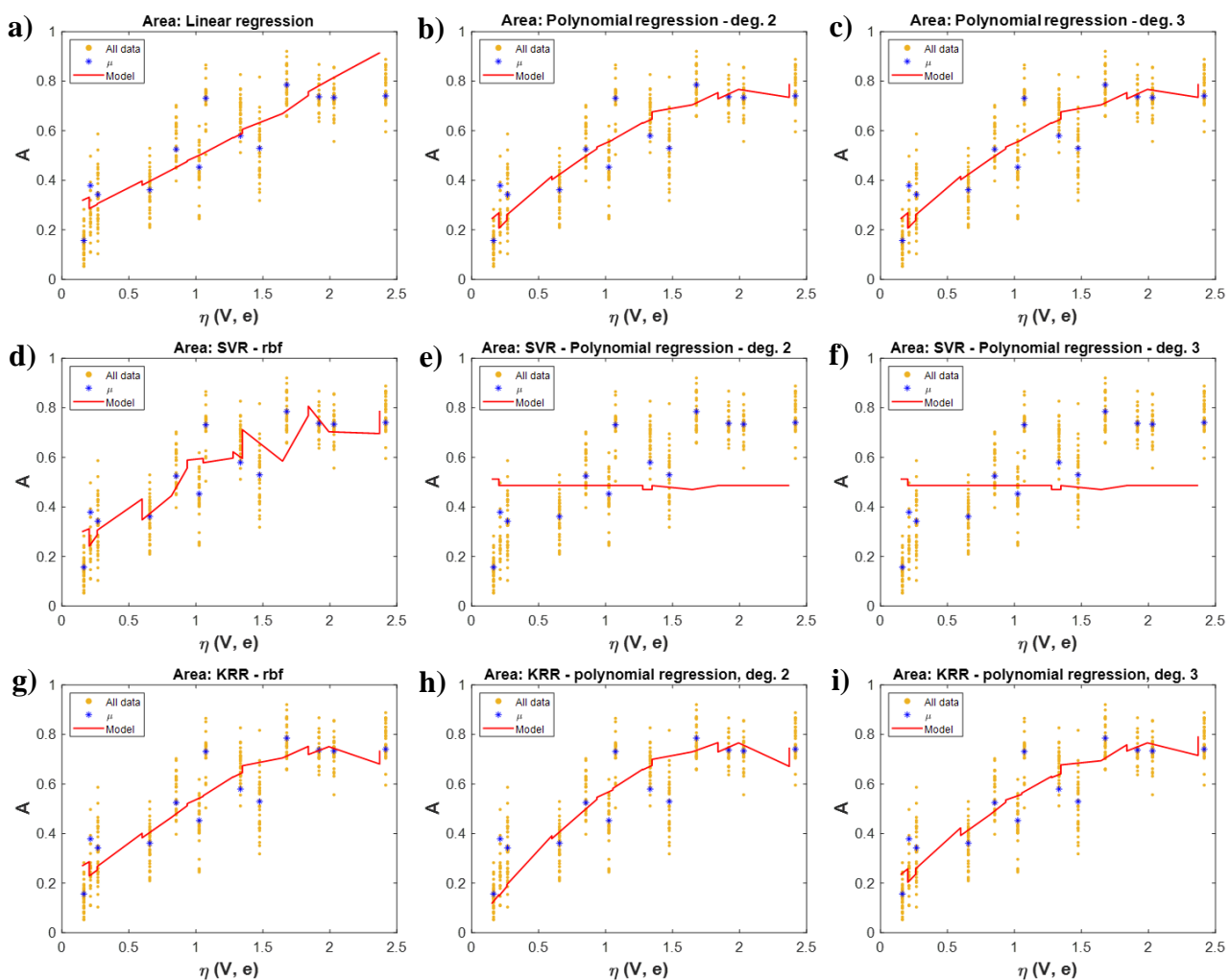
Figure 4.5. Comparing experimental data (yellow), mean values of experimental data (blue) and statistical model predictions (red) for A versus $\boldsymbol{\eta(V, e)}$ using a) linear regression curve fit, b) 2nd order polynomial regression curve fit, c) 3rd order polynomial curve fit, d) SVR with rbf kernel, e) SVR with 2nd order polynomial kernel, f) SVR with 3rd order polynomial kernel, g) KRR with rbf kernel, h) KRR with 2nd order polynomial kernel, i) KRR with 3rd order polynomial kernel.

The predictions of statistical modeling, as captured in Figure 4.4d, indicate that the radius ratio, R linearly increases with $\eta(V,e)$ with a gradient of 2.5. This implies that if an electric field is provided such that $\eta(V,e) = 2$, the initial average radius in the distribution will increase by 5X. The reduction in wetted area does not follow a linear trend (Figure 4.5h), and the model can estimate the electric field to maximize the reduction in wetted area. Figure 4.5h shows $\eta(V,e)\sim1.75$ yields the maximum reduction in wetted area of $\sim70\%$. The utility of this model lies in the ability to predict the electric field, (captured via $\eta(V,e)$), required to yield a desired droplet size distribution from an initial distribution. As an illustration, a 2X increase in average droplet radius would require an electric field corresponding to $\eta(V,e) = 0.75$ (based on the reference given in Figure 4.4d).

An examination of Figure 4.4 also shows that the data has scatter which can be attributed to a combination of experimental uncertainty and the stochastic nature of coalescence dynamics under electric fields. Additionally, the scatter increases at higher values of $\eta(V,e)$, which can be attributed to contact angle saturation, whereby the droplet stops responding to the electric field [17], [18]. Even with the scatter in Figure 4.4 and Figure 4.5, there is a clear trend showing the influence of $\eta(V,e)$ on the radius ratio enhancement and the normalized reduction in wetted area, respectively. It is reiterated that both these variables quantify droplet coalescence and the resulting change in the droplet size distribution upon the application of an EW field.

Figure 4.4 and Figure 4.5 quantify the influence of $\eta(V,e)$ on R and A, respectively, which are directly related to the droplet size distribution. We can also quantify the influence of $\eta(V,e)$ on droplet size distribution further by analyzing the influence of the EW field

on the spread of the droplet size distribution. The spread is defined as the ratio of the standard deviation of the droplet size distribution relative to the area average radius as:

$$S_i = \frac{\sigma_i}{\widehat{R_\iota}} = \frac{standard\ deviation}{area\ average\ radius} \qquad (4.3)$$

A large value of S_i indicates that a wide range of droplet sizes exist relative to $\widehat{R_\iota}$, whereas a smaller value of S_i indicates that most of the droplets are of similar size to $\widehat{R_\iota}$. The change in S_i before and after the application of the EW field is quantified as:

$$S = S_F/S_I \qquad (4.4)$$

where S_F and S_I are the final and initial distribution spreads, respectively. Figure 4.6 shows the change in S as a function of $\eta(V,e)$. For small values of $\eta(V,e)$, the change in the distribution spread is negligible ($S\sim 1$). However, after $\eta(V,e) = 0.75$, the change in the spread shrinks by $\sim 50\%$, indicating that the distribution of droplets reduces significantly and many droplets are closer in size to the mean radius. The spread ratio maintains this trend for larger values of $\eta(V,e)$. Combining this information with the results depicted in Figure 4.4 and Figure 4.5 makes it clear that an increase in $\eta(V,e)$ will not only increase the droplet size and reduce the wetted area, but also narrow the droplet size distribution, and reduce the number of droplets on the surface.
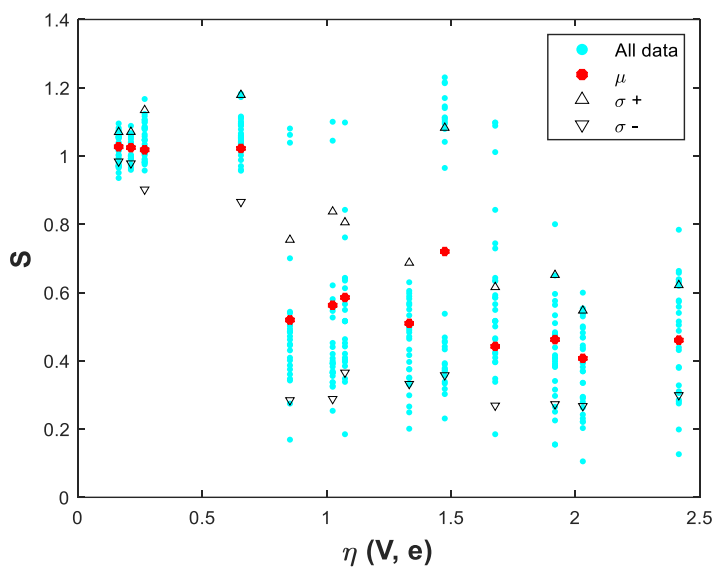
Figure 4.6. Change in the spread in droplet size distribution versus $\eta(V, e)$.

4.4 DISCUSSIONS

We now discuss the transients associated with EW-induced droplet coalescence, noting that the models depicted in Figure 4.4, Figure 4.5 and Figure 4.6 shows the overall change in droplet coalescence parameters. The time-dependent average radius after applying the EW voltage was estimated via the image analysis procedure described previously. Parameter shrinkage analysis using Ridge regression and Lasso regression was conducted to identify the variables which contribute most significantly to the transient change in radius. The variables analyzed were the applied voltage (V), AC frequency (f), electrode geometry (electrode width (e)), and the time (t). Figure 4.7 shows the results from Ridge regression and Lasso regression-based parameter shrinkage analysis. The results show that there are strong correlations between the change in radius R and the voltage, electrode width and time. AC frequency has the lowest correlation coefficient

77

(10X smaller than other coefficients). This again leads to the conclusion that AC frequency has a negligible influence on droplet coalescence dynamics.
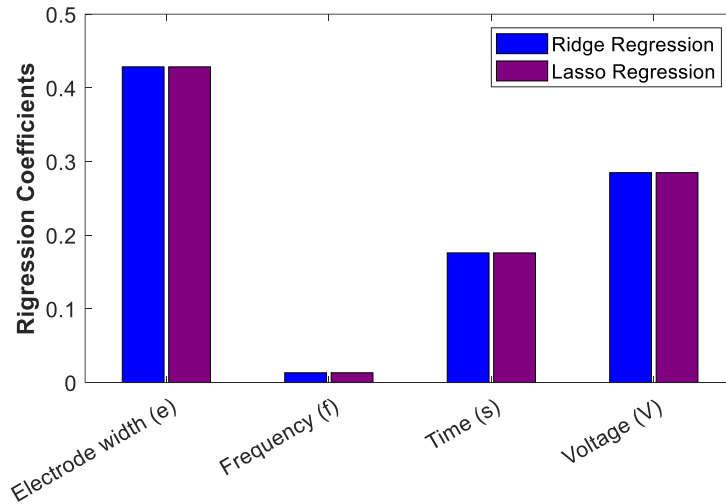
Figure 4.7. Parameter selection and shrinkage conducted using Ridge regression (blue) and Lasso regression (purple) to quantify the influence of various parameters on transient change in radius.

Figure 4.8 shows the voltage-dependent, transient, radius enhancement ratio for three different electrode geometries. As expected, the radius increases faster at higher voltages due to larger electrostatic forces to promote coalescence. Additionally, a large jump in radius ratio from 100 V (threshold voltage) to 200 V is observed. Larger electrode widths also show a greater increase in radius. The 50 µm electrode width geometry enables a maximum radius enhancement ratio of $R\sim3$, whereas the 200 µm electrode width geometry enables an enhancement of $R = 5.5$-6. It is also noted that most of the coalescence events occur in the first 5 seconds after the field is applied, after which the average radius generally plateaus out. Such a coalescence cascade was also reported in

other recent studies [12], [15]. This finding also justifies our use of a 15 second interval to quantify the influence of EW fields on coalescence dynamics.
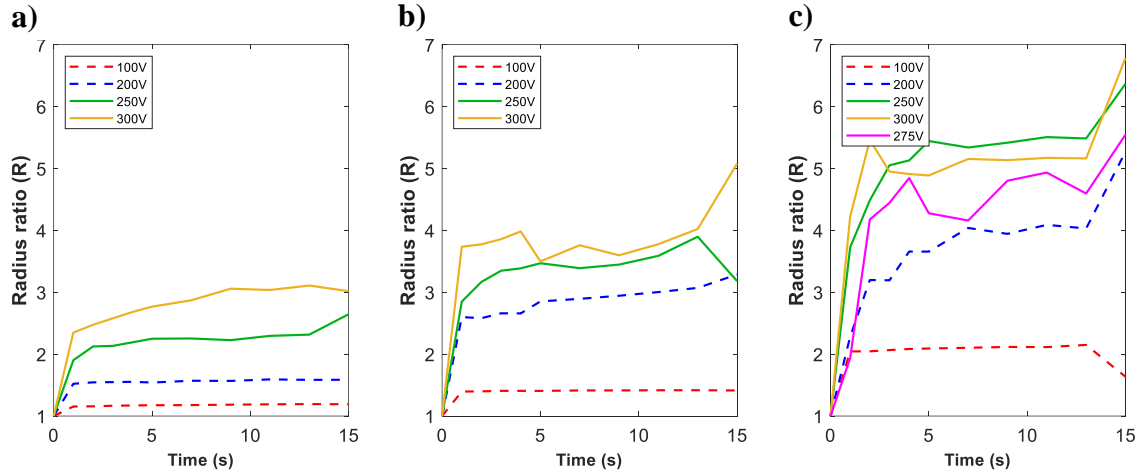
Figure 4.8. Transient change in radius enhancement ratio R for a period of 15 seconds after the application of EW voltages on devices with electrode widths a) 50 μm, b) 100 μm and c) 200 μm. Most coalescence events occur immediately after the application of an EW field leading to a coalescence cascade.

Next, we discuss the physics underlying the observed dependence of coalescence parameters on the applied voltage (V) and electrode geometry (captured by electrode width (e)). The observed data and the models show that higher voltages and higher electrode widths enhance droplet coalescence. This can be explained by considering the electrowetting curve (contact angle (CA) versus voltage) for sessile water droplets [17], [18]. Figure 4.9 shows the electrowetting curves for two different electrode widths as obtained from the Young-Lippman equation (Equation 2.3) and via experiments with sessile water droplets. As expected, droplets spread with increasing voltage till the onset

of CA saturation [12]. Additionally, Figure 4.9 shows that a larger electrode width yields a larger change in CA for a specified voltage; this is directly related to the increased capacitance associated with the larger electrode width as quantified in Equation 2.5. [79]. Since droplet spreading ultimately leads to droplet coalescence, the radius enhancement ratio is expected to increase with higher voltages and electrode widths. Similarly, the reduction in wetted area also increases with an increase in the voltage and electrode width. However, the reduction in wetted area ratio reaches a plateau, as per Figure 4.5, even though the radius enhancement ratio is increasing. This can be explained by the CA saturation phenomena, wherein the wetted area becomes independent of the applied voltage above a certain applied voltage.
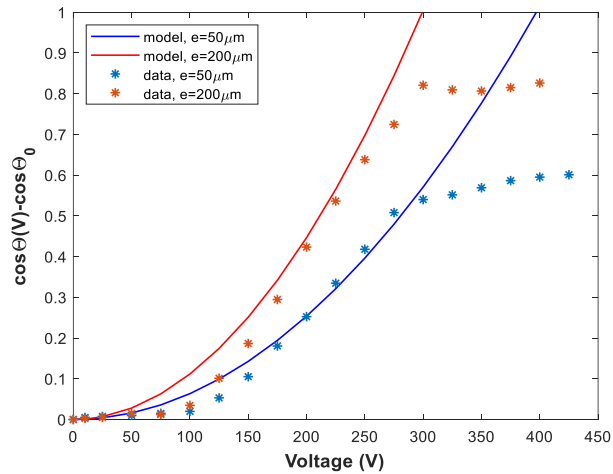
Figure 4.9. Electrowetting curve showing the change in contact angle with applied voltage for two electrode widths.

Finally, the utility of this study for condensation heat transfer is briefly discussed. There are a few recent studies [12]–[14] on EW enhanced droplet condensation, which

involve condensation occurring under a continuously applied electric field. A continuous electric field is not a strict requirement; periodically applied electric fields can also result in significant enhancement in condensation [16]. This study will directly benefit any such 'electrical intervention' strategies to enhance dropwise condensation. The output parameters tracked in this study are critical to overall performance. The growth rate of droplets via coalescence is significant since the enhancement mechanism is about reorganizing the condensate into high volume droplets that can then shed-off. The droplet size is also a critical parameter in the estimation of the thermal resistance associated with heat transfer [5]. The reduction in wetted area determines the rate at which condensation will reoccur on the surface. Overall, this study represents a new approach to predicting the performance of EW-enhanced dropwise condensation. This study can benefit other applications which rely on droplet manipulation via EW like anti-fouling or self-cleaning [23].

4.5 CONCLUSIONS

This is the first reported study of EW-induced droplet coalescence, which uses machine learning-based statistical algorithms to develop predictive models using experimental data. The attractiveness of this approach lies in the challenges involved in developing accurate physics-based models for complex microfluidic systems. Importantly, this approach leverages the large amount of data available in condensation experiments (via tracking a multitude of droplets). The developed models predict the change in droplet radius and wetted fractions as a function of the applied voltage and electrode geometry. Importantly, they can provide additional physics-based insights that would be challenging

to infer otherwise, such as droplet coalescence being independent of the AC frequency. It is important to note that while this analysis involves the use of statistical techniques, it is grounded in the basic physics associated with EW. Overall, this chapter presents a data science-based statistical model as a reference tool to predict droplet coalescence dynamics based on the input EW parameters identified in this study.

Chapter 5: AC electrowetting promoted droplet shedding on hydrophobic surfaces

While several phenomena (droplet growth, coalescence, shedding) are important in dropwise condensation, the key benefit of dropwise condensation is a result of droplet shedding, which exposes fresh areas for re-nucleation, and prevents the formation of a continuous liquid film. The objective of electrowetting (EW)-accelerated condensation is to move the condensed liquid into a more favorable state for removal by coalescing droplets to make them large enough for gravity-assisted removal. Under an EW field, coalescence of a distribution of droplets is not continuous. Rather, coalescence occurs in cascades, wherein droplets coalesce rapidly in a short time interval, followed by a relatively quiet phase (no coalescence), till the droplets grow large enough for the next coalescence cascade. These observations suggest that a continuous EW field is not a strict necessity, and periodic EW fields can be effective in removing condensate; this premise is studied in the present chapter.

This chapter studies the physics underlying EW-induced shedding of droplets on a hydrophobic surface. It is seen that while the applied voltage influences the extent of droplet shedding, the rate of droplet shedding is influenced by the AC frequency. We see that surfaces can be significantly de-wetted (> 90% dry) in less than a second. Importantly, the measured water removal rates under EW fields are higher than typical dropwise condensation rates by >100X. It is noted that this chapter focuses on droplet shedding only, and that the results are applicable even for non-condensation environments.

5.1 EXPERIMENTAL PROCEDURES

Device fabrication and the experimental procedure is briefly described ahead. Indium Tin Oxide (ITO) coated glass slides were used as the substrate. Photolithography and plasma etching were used to pattern ITO into two sets of interdigitated electrodes, shown in Figure 5.1 (detailed fabrication method provided in Section 3.1). These were connected to the high voltage and ground ends of a signal generator and amplifier to generate an electric field in the gap between electrodes (Figure 5.1b). A 5 µm layer of SU-8 was spin-coated as the EW dielectric, followed by spin coating of a 100 nm layer of Teflon for hydrophobicity.

The starting ensemble of droplets (to be shed off) was obtained by spraying water on vertically oriented devices using a commercial humidifier. Droplet size distributions obtained were reasonably consistent (average droplet radius was ~150 µm ± 50 µm). It is striking to observe that the obtained distribution is similar to that obtained in classical dropwise condensation experiments[118]. This justifies the translation of present results to dropwise condensation applications. Post droplet-deposition, the surface was visualized using a stereoscope. The EW field was then turned on for 30 seconds, during which most of the water shed off the surface. Individual droplets were tracked using a MATLAB circle finder code.

Three experimental parameters were varied presently. Firstly, three different electrode geometries were used with electrode widths of 50 µm, 100 µm and 200 µm; spacing between electrodes was 50 µm in all devices. These two parameters influence the electric field and the penetration height of the electric field outside the surface. The second parameter was the applied voltage, with experiments conducted at 175 V, 200 V and 300

V. This voltage range was selected to be above the threshold voltage (when droplet shedding is first observed), and the saturation voltage (contact angle stops responding to voltage[17], [18]). The third parameter was the frequency of the applied AC waveform. Experiments were conducted at 1 Hz, 10 Hz, and 1 kHz; together this frequency range accounts for various types of fluid motion (ranging from droplet translation to shape oscillation). All experiments were repeated 5 times. The applied voltage and geometry were combined in terms of an electric field. The equivalent electric field was estimated as $E \sim \frac{V}{d}$ where V is the voltage and d is the equivalent thickness of the dielectric layer (obtained by fitting the measured change in contact angle to the Lippman's curve).

a)

b)
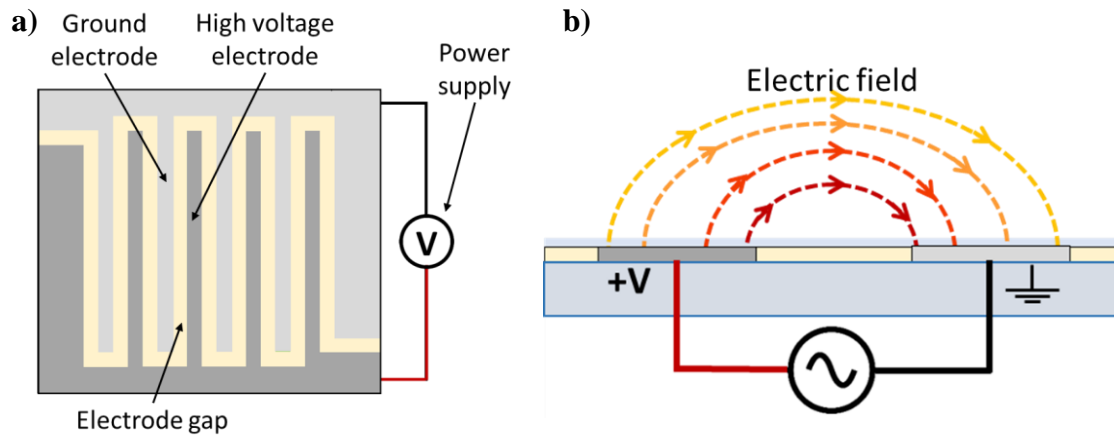
Figure 5.1. Schematic showing the arrangement of interdigitated electrodes. (b) Cross-section of device showing electric field lines.

5.2 EXPERIMENTAL RESULTS- DROPLET ROLL-OFF DYNAMICS

Figure 5.2 shows EW-induced droplet shedding at different frequencies, voltage and electrode geometries. The extent of droplet shedding is quantified by the dry area fraction Γ, estimated as:

$$\Gamma = A_{dry}/A_{total} \qquad (5.1)$$

Γ is estimated via image analysis, and represents the fraction of the surface not covered with water. It is noted that a threshold voltage is needed to electrically actuate droplets. In this study we define the threshold voltage as the voltage which increases Γ by 20%. For the 50 μm, 100 μm and 200 μm devices, the threshold voltages were 175V, 135V and 130V, respectively. Figure 5.2 shows that for a 175 V, 1 Hz waveform, Γ increases from 45% to 70%. Importantly, at higher frequencies, almost the entire surface is water-free; 175 V, 1 kHz increases Γ from 43% to 92%. Additionally, at highest applied voltage (300 V) and largest electrode width (200 μm), Γ increases from 45% to 98%, which is the highest achieved dry area fraction in the configurations used in this study.
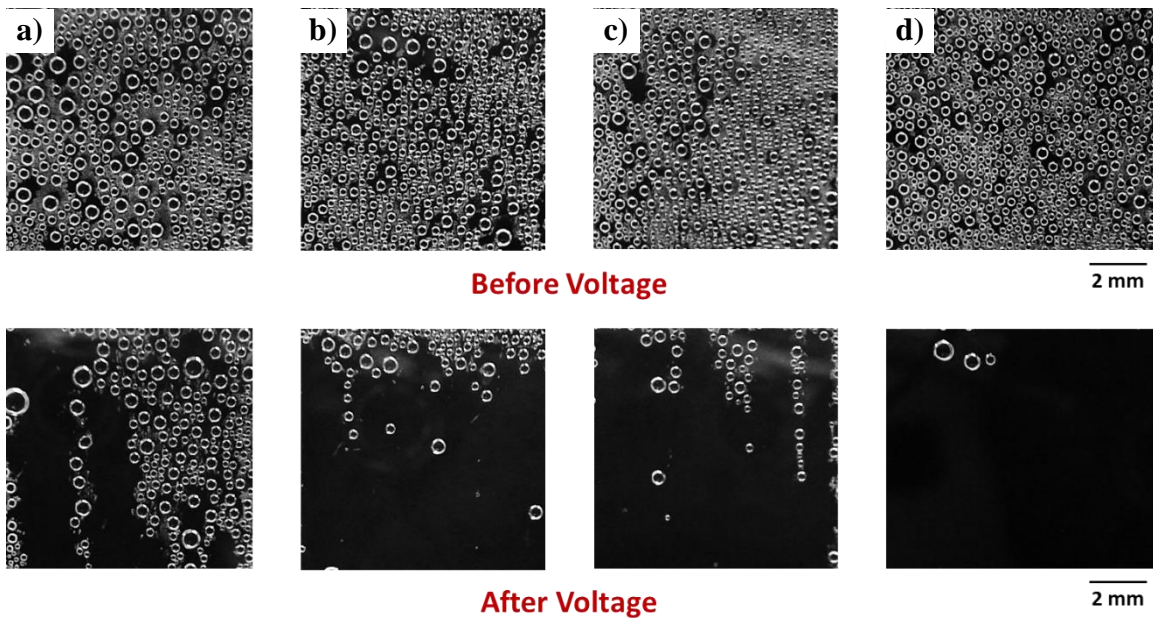
Figure 5.2: continued next page

Figure 5.2 EW-induced droplet shedding at a) 175 V, 1 Hz on 100 μm electrode width device, b) 175 V, 10 Hz on 100 μm electrode width device, c) 175 V, 1 kHz on 100 μm electrode width device, and d) 300 V, 10 Hz on 200 μm electrode width device. The top images show the surface before voltage is applied and the bottom images show the surface 30 seconds after the voltage is applied.

The physics underlying droplet coalescence and shedding is related to the reduction in contact angles as per the Young-Lippman equation (Equation 2.3) [17], [18] and the rearrangement of droplets on energy minima positions on the surface[12], [15]. Figure 4.9 shows the change in contact angle as a function of applied voltage and electrode width, based on the modified capacitance term in the Lippmann's equation (Equation 2.5). The contact angle reduces till contact angle saturation is reached (~300V), after which the contact angle no longer changes with the applied voltage [17]. Figure 4.9 also shows that for a larger electrode width, there is a larger change in contact angle [79]. In the present droplet shedding experiments, the reduction in contact angle leads to the droplet spreading out (in addition to physically moving) and coalescing with neighboring droplets. This leads to droplet growth and eventual shedding.

Under AC electric fields, the nature of droplet motion depends on the AC frequency[15], [69]. At low frequencies (frequency < charge relaxation time), droplets will mechanically oscillate in response to the sinusoidal field [69]. At frequencies greater than the charge relaxation time, the droplet cannot mechanically respond to the changing field; instead convection occurs internally[65], [69]. All types of droplet motion leads to droplet coalescence, growth and eventual shedding. A deeper understanding of this can be gained by high speed visualization of droplet motion, coalescence and shedding. Figure 5.3 shows

a frame illustrating the influence of three different frequencies, 1 Hz, 10 Hz and 1 kHz on a distribution of droplets when the electric field is first applied. At 1 Hz, the droplets begin to slowly move to surface energy minima as the field increases according to the sinusoidal wave form, causing coalescence events. At such low frequencies, droplets maintain their stable location for longer, resulting in slower and less frequent coalescence events. At 10 Hz, similar droplet motion and coalescence events occur, but ~ 10X more often per cycle than at 1 Hz frequency, resulting in faster de-wetting. At 1 kHz, all droplets immediately move to the surface energy minima causing an instant coalescence cascade. Additionally, as the AC frequency is higher than the droplet mechanical response time, the droplet does not translate with the alternating field; instead internal mixing occurs within the droplet. The application of an AC field will also oscillate and perturb the three-phase contact line, depinning the droplets from the surface, further assisting shedding. Figure 5.3 clearly shows that 1 kHz has the maximum number of coalescence events for a given time, followed by 10 Hz and 1 Hz.
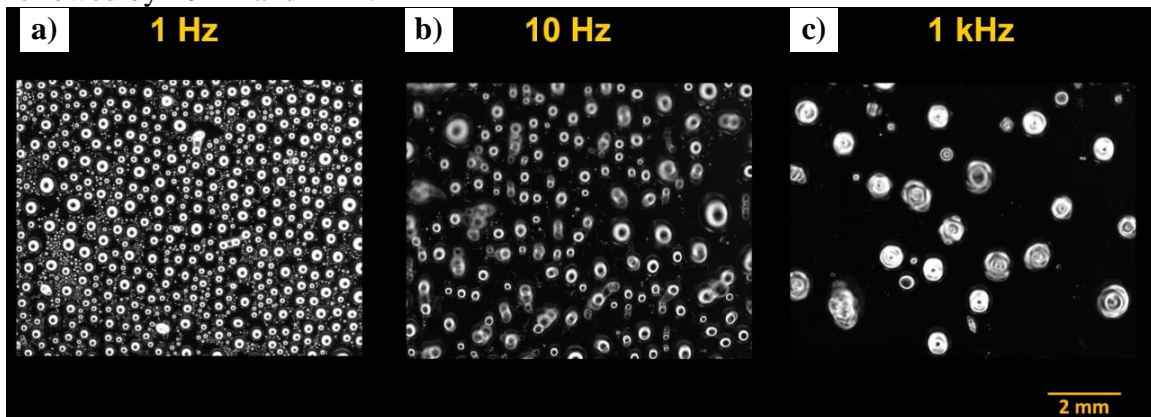
Figure 5.3. AC frequency dependent droplet coalescence dynamics at 300V on devices with electrode width of 200 μm.

Figure 5.4 shows the influence of voltage and frequency on Γ for the three devices. The bottom of the vertical bar shows the initial Γ ($\Gamma_{t=0s}$) and the top shows the Γ after the experiment ($\Gamma_{t=30s}$). Figure 5.4 offers several insights into the underlying physical mechanisms. Firstly, very high Γ ($> 90\%$) is obtained at 300 V for all devices; Figure 5.4 shows that almost the entire surface is water-free, with Γ=98%. In general, Γ increases with voltage, and with larger electrode widths. For electric fields with voltages >200V and electrode:electrode gap ratios >2 (~9 V/µm), the final Γ was always >85%. Achieving such high values of Γ is challenging without the use of superhydrophobic surfaces[23]. Secondly, Γ increases rapidly above the threshold voltage. This is most clearly obvious for the 50 µm device, where the Γ is noticeably higher at 200 V, compared to the threshold voltage of 175 V. This is further confirmed from the results of the 100 µm and 200 µm devices, which do not show a large difference in Γ between 200 V and 300 V, noting that the threshold voltages for these devices are 135 and 130 V respectively. Importantly, these findings *show that significant water shedding can be achieved, without needing to use voltages significantly higher than the threshold voltage*. Thirdly, the *frequency of the AC waveform does not influence Γ at voltages significantly above the threshold voltage*; this is observed for all devices. It is noted that the frequency influences Γ only near threshold voltages, with increasing frequencies resulting in higher Γ's. Overall, these findings show that while the frequency determines the nature of droplet motion, it does not strongly influence Γ, which is primarily determined by the magnitude of the electric field.
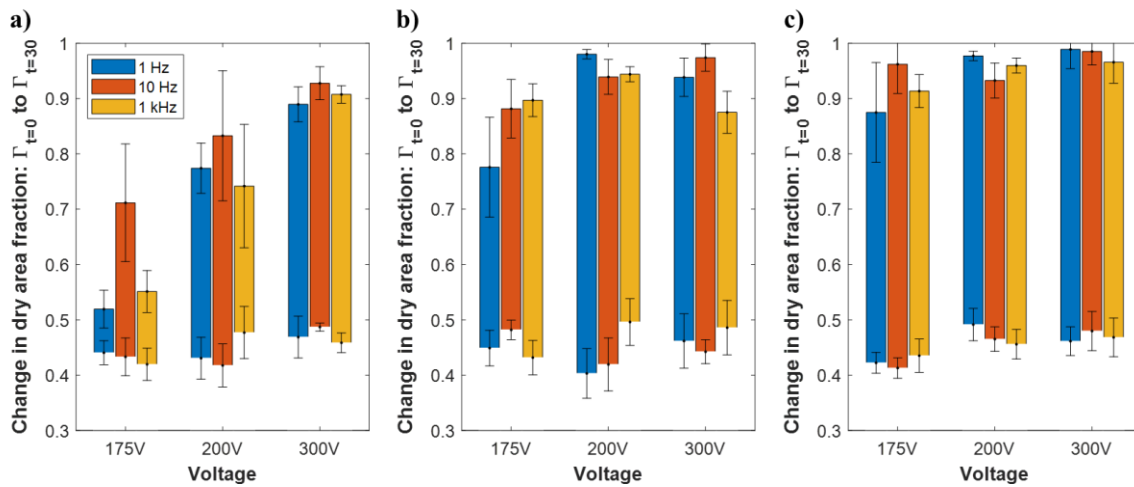
Figure 5.4 Change in dry area fraction due to an EW field on devices with electrode widths of a) 50 μm, b) 100 μm and c) 200 μm. Highest dry area fraction obtained in this study was 98% at 300 V, 10 Hz on the device with 200 μm electrode width.

A deeper understanding of these trends can be gained from evaluating the transient evolution of the dry area fraction. Figure 5.5 shows the transient evolution of dry area fraction (Γ) as a function of voltage, electrode width (top to bottom) and AC frequency (left to right). For weak electric fields corresponding to the threshold voltage the final Γ changes minimally, such that only a 25% increase in Γ occurs at the end of 30 seconds (top left). Above the threshold voltage, the final Γ is greater than >85%. At the highest electric field and highest frequency (bottom right) the final Γ is as high as 95%.
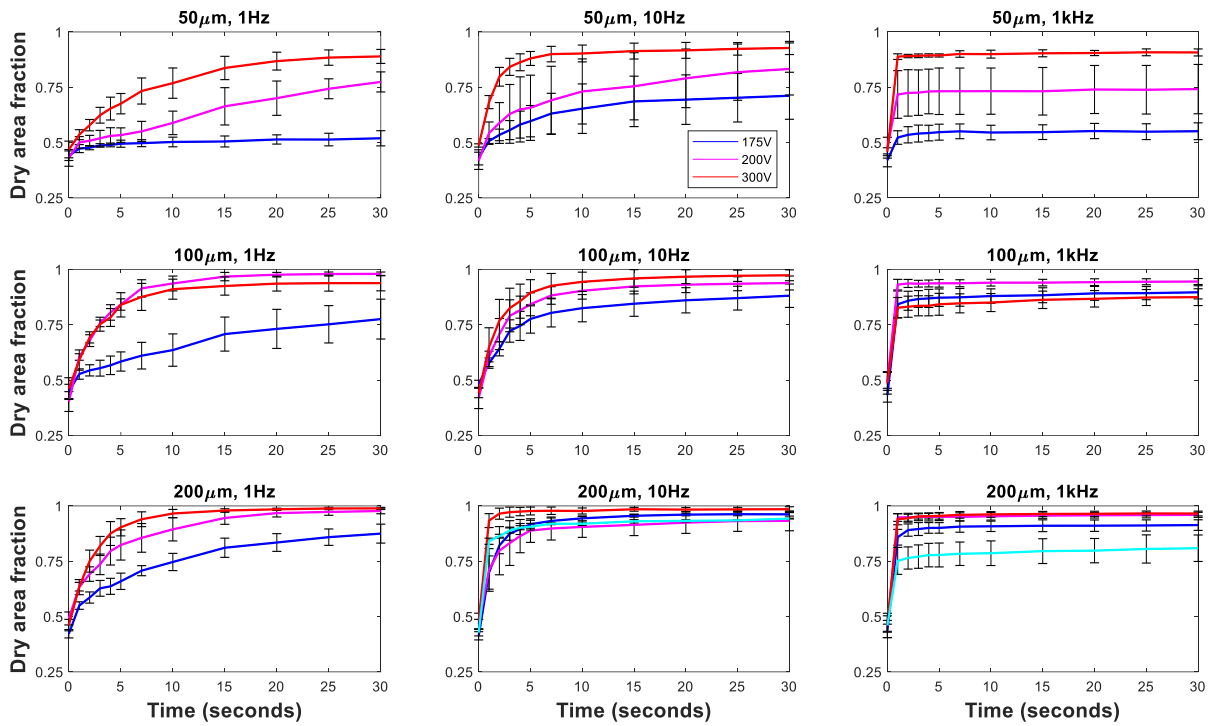
Figure 5.5 Transient evolution of dry area fraction as a function of voltage, electrode width (top to bottom) and AC frequency (left to right). Light blue line represents experiments with horizontally oriented electrodes with 200 μm electrode width, 300 V

The influence of electrode width and frequency on transient Γ can be observed more clearly at voltages close to the threshold voltage, as seen in Figure 5.6. At larger electrode widths (or larger electrode:electrode gap ratios, where electrode gap is 50 μm) the final Γ increases, such that there is ~80% increase in the final Γ when the electrode:electrode gap ratios increases from 1 to 4. This can be attributed to the increased electric field for larger electrode widths. The influence of frequency on final Γ is more clear at lower voltages. At 1 Hz, the smallest increase in Γ is seen, whereas at 10 Hz, the largest increase in Γ is seen,

for all electrode widths. However, as the electric field (or electrode width) increases, the influence of frequency on the final Γ is reduced.
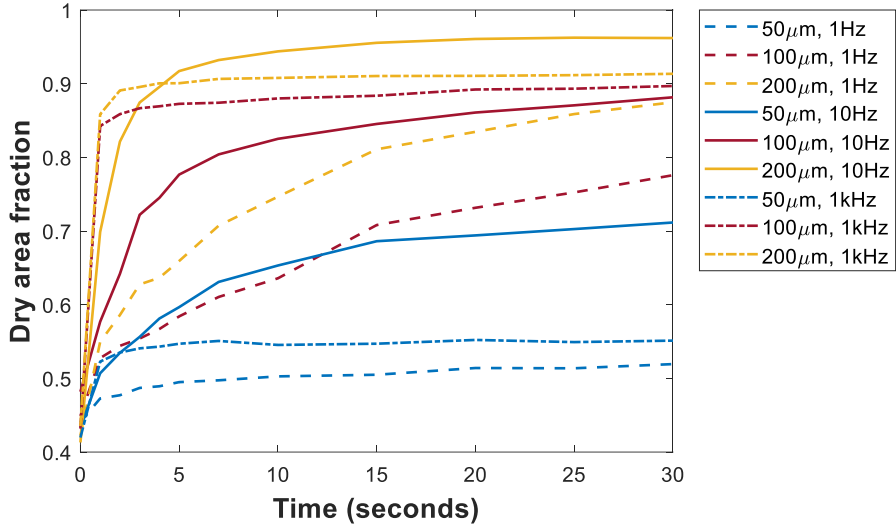
Figure 5.6 Transient evolution of dry area fraction at 175 V, as a function of electrode width and frequency.

In addition to the change in Γ, the rate at which Γ changes is important for applications that require rapid water removal (eg. windshields). In Figure 5.5 and Figure 5.6, the 200 µm device sees a $\Gamma > 90\%$, whereas the 50 µm device only sees $\Gamma \sim 70\%$. This again shows the influence of the electric field (highest for 200 µm device) on droplet shedding.

Significant physical insights can be obtained by using the data in Figure 5.5 to define a *de-wetting time constant* τ; this is a measure of the time taken to reach the steady state Γ. This definition is inspired by comparison with physical systems which involve transients. τ is estimated by fitting the transient Γ to the below model:

$$\frac{\Gamma(t)}{\Gamma_0} = 1 - \exp\left(-\frac{t}{\tau}\right) \qquad (5.2)$$

where Γ_0 is the initial Γ. The steady state is defined as that corresponding to $t = 4\tau$. Physically, τ represents the speed at which the surface is de-wetted, and is an important parameter for systems with transient EW fields.
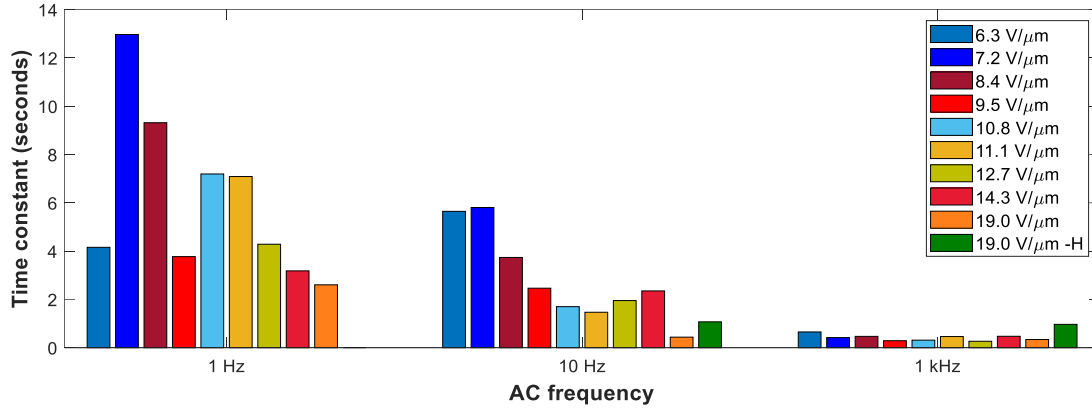
Figure 5.7 Time constant as a function of AC frequency and electric field.

Figure 5.7 shows the frequency-dependent time constant for different devices. At low frequency (1 Hz), the time constant is >4 seconds. At such frequencies, the droplet mechanically responds to the electric field by shape oscillations and translation. At higher frequencies, (1 kHz) the time constant is <1 second. Such frequencies are higher than the charge relaxation time, and no macroscopic droplet motion is observed after droplets reach the energy minima positions. However, the coalescence cascade[12], [15] setup at such frequencies is stronger than the one in the low frequency case, which causes rapid surface cleaning. High speed visualization clearly shows that 1 kHz has the maximum number of coalescence events, followed by 10 Hz and 1 Hz. It is noted that the time constant is

independent of the final Γ. In summary, *while Γ is predominantly determined by the voltage, the time required to reach Γ is strongly influenced by the frequency*. Additionally, Figure 5.7 shows that τ generally decreases with increasing electric field within each frequency bin. For the case of 10 Hz, at the lower range of electric fields (<8 V/μm), the time constant is ~2X higher than the time constant in the higher range of electric fields (>12 V/μm).

It is noted that the electrode orientation plays a notable role in droplet removal. In all the experiments reported so far, the electrodes were vertically oriented (with respect to gravity). For the combination of device and waveform (200 μm electrode width, 300 V at 10 Hz and 1 kHz) that resulted in the highest Γ, additional experiments were conducted with horizontally oriented electrodes. The measured Γ is 4% and 16% less than the vertically oriented electrodes for 10 Hz and 1 kHz, respectively. This can be attributed to electrostatic pinning of droplets on electrodes as droplets move across electrodes (in the horizontal electrode configuration). In contrast, for vertically oriented electrodes, the droplets remain on the same set of electrodes as they slide down, which reduces pinning.

5.3 ELECTRIC FIELD ASSISTED MASS REMOVAL

The above findings highlight the rapid removal of water immediately after the application of an EW field; this suggests benefits in using periodic EW fields as opposed to continuous fields. It is insightful to compare the presently obtained mass removal rates with mass removal rates resulting from continuous EW fields and those achieved during classical steady state condensation. Figure 5.8 provides such a comparison and shows the mass flux versus the electric field. Mass flux in the present study was estimated via image analysis over the duration 4τ. Figure 5.8 also includes condensation rate measurements (80% relative humidity) under a continuous electric field using the procedure detailed in

Chapter 3 [15]. Additionally, steady state condensation rates from two other studies are also included[3], [23].

The presently obtained mass removal fluxes are 200-400X higher than condensation rates for continuous electric fields. They are two orders of magnitude higher than those achieved in the absence of an EW field. These numbers suggest that waiting for droplets to grow and then applying an electric field might result in higher overall condensation rates; however more detailed studies are needed to validate this hypothesis. Figure 5.8 also shows that the mass flux increases with the electric field, which is a consequence of a higher Γ. Higher mass fluxes are obtained at 1 kHz as compared to 1 Hz; this can be attributed to the smaller time constants at 1 kHz.
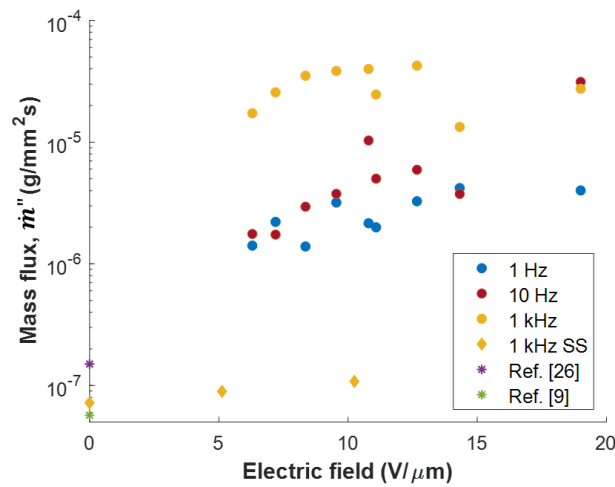
Figure 5.8 Mass flux from the present work compared to steady state condensation mass flux under i) continuous electric fields, and ii) no electric fields[3], [23].

Fundamentally, the mass removal flux can be estimated via scaling analysis from knowledge of the change in dry area fraction and time constant. A control volume can be

defined around a single droplet on the surface (Figure 5.9) and the change in mass within the control volume can be estimated as detailed ahead.
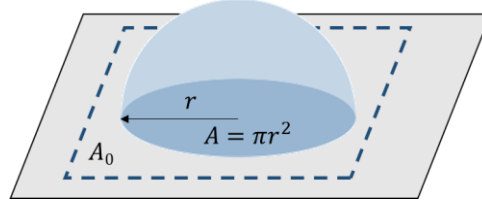
Figure 5.9 Control volume showing a sessile droplet on the surface.

A droplet of radius r and area $A = \pi r^2$ resides within an area A_0 (within the control volume). The corresponding wetted area is $a_w = A/A_0 = \frac{\pi r^2}{A_0}$. The mass of the droplet is $m = \frac{2}{3}\rho\pi r^3$. The rate of change of mass can be expressed as:

$$\dot{m} = \frac{dm}{dt} = 2\rho\pi r^2 \frac{dr}{dt} \qquad (5.3)$$

The change in dry area fraction can be expressed as:

$$\frac{d}{dt}\left(\frac{A}{A_0}\right) = \frac{d}{dt}\left(\frac{\pi r^2}{A_0}\right) = \frac{2\pi r}{A_0}\frac{dr}{dt} \qquad (5.4)$$

Combining equations 5.3 and 5.4, we get:

$$\dot{m} = \frac{dm}{dt} = \rho r A_0 \frac{d}{dt}\left(\frac{A}{A_0}\right) \qquad (5.5)$$

The mass flux then becomes:

$$\dot{m}" = \frac{\dot{m}}{A_0} = \rho r \frac{d}{dt}(a_w) \qquad (5.6)$$

By scaling analysis

$$\dot{m}" \sim \rho r_0 \frac{\Delta a_w}{4\tau} \qquad (5.7)$$

where the change in dry area fraction is $\Delta a_w = a_w(t = 0) - a_w(t = 4\tau)$

Mass flux based on the above analysis can be calculated from the change in dry area fraction and time constant, which are directly related to the electric field (voltage and electrode width) and frequency, respectively. The advantage of this approach is that the two parameters, Γ and τ can be easily evaluated via image analysis. This modeled mass flux (Equation 5.7) is compared with the experimental data to verify the utility of this analysis (Figure 5.10). It is seen that the analytical model shows a very reasonable match (maximum difference of 30%) with experimental measurements of mass removal fluxes, thereby highlighting the utility of this simple model.
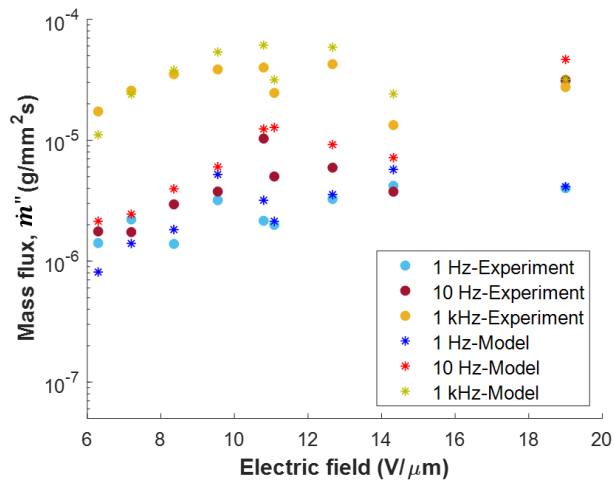
Figure 5.10 Comparison of analytical model with experimentally estimated mass fluxes.

Additionally, the mass removal flux can be modeled using a force balance including effects of gravity, surface tension and electrical forces. Figure 4.9 can be used to derive a relationship for the change in wettability based on the electric field, which will cause droplets to spread out and coalesce, resulting in gravity driven droplet shedding.

5.4 CONCLUSIONS

In conclusion, this chapter provides a deeper understanding of the fundamentals underlying EW-induced droplet shedding on hydrophobic surfaces. Experiments track the shedding of an ensemble of water droplets under the influence of EW fields, with three parameters being varied (voltage, AC frequency and device geometry). Significant physical insights into EW-induced droplet shedding are obtained. Firstly, EW enables almost complete removal of water (dry area fraction> 95%) in very short time durations (~ 1 second). Secondly, while the dry area fraction does depend on the applied voltage, significant water shedding can be achieved without needing to apply voltages significantly higher than the threshold voltage. Thirdly, the frequency of the AC waveform does not influence the dry area fraction for voltages above the threshold voltage; however the time required to shed droplets strongly depends on the AC frequency. Fourthly, the orientation of the device influences water removal due to electrostatic pinning of the droplets. Finally, the measured water removal mass fluxes immediately after the application of an electric field are two orders of magnitude higher than those achieved previously; this highlights the benefits of periodic EW fields as opposed to continuous EW fields. Overall, these results suggest that the combination of electrowetting and hydrophobic surfaces can give performance enhancements similar to those achieved by superhydrophobic surfaces.

Chapter 6: Characterization of oscillation amplitude of contact angle during AC electrowetting of water droplets

This chapter presents a study of AC voltage and frequency dependent oscillations of an electrowetted water droplet on a macroscopically smooth hydrophobic surface. We introduce a new technique to analyze droplet oscillations, which involves characterization of the contact angle oscillation amplitude (CAOA), instead of tracking transient CAs. It is shown that this methodology can be used to develop an experimentally validated, fundamentals-based equation to predict voltage and frequency-dependent CAOA, which is analogous to the Lippman's equation for predicting voltage-dependent CA. It is seen that this approach can help estimate the threshold voltage more accurately, than from experimental measurements of CA change. Additionally, we use a coplanar electrode configuration with high voltage and ground electrodes arranged on the substrate. This configuration eliminates measurement artefacts in the traditional EW configuration associated with a wire electrode protruding into the droplet. An interesting consequence of this configuration is that the system capacitance is reduced substantially, compared to the classical configuration. The coplanar electrode configuration shows a reduced rate of CA change with voltage, thereby increasing the voltage range over which the CA can be modulated. The understanding gained about droplet oscillation dynamics through this study can be used to explain droplet dynamics reported in previous chapters.

6.1 PROCEDURE FOR EXPERIMENTS AND ANALYSIS

For the experimental set up, coplanar electrode-based EW devices were fabricated using photolithographic methods on an Indium Tin Oxide (ITO) coated glass slide [15];

the detailed fabrication procedure described in Chapter 3. A schematic of the arrangement of interdigitated electrodes is shown in Figure 6.1. The electrode width and the spacing between the electrodes (electrode gap) were 50 µm, each. The active electrode area was coated with a 2 µm layer of Parylene C (EW dielectric layer), via room temperature vapor deposition. The devices were then spin coated with a thin (~100 nm) layer of Teflon AF to increase the initial CA of the droplet and reduce friction at the triple-phase contact line.

Droplet oscillation experiments were conducted by placing a 5 µl droplet of deionized water on the substrate. It is noted that a droplet of this volume covered between 17-20 sets of electrodes (set of electrodes includes two electrodes and two electrode gaps, i.e. a total of 200 µm). CA measurements were conducted via side view visualization at upto 210 FPS using a goniometer (Biolin Scientific Theta).
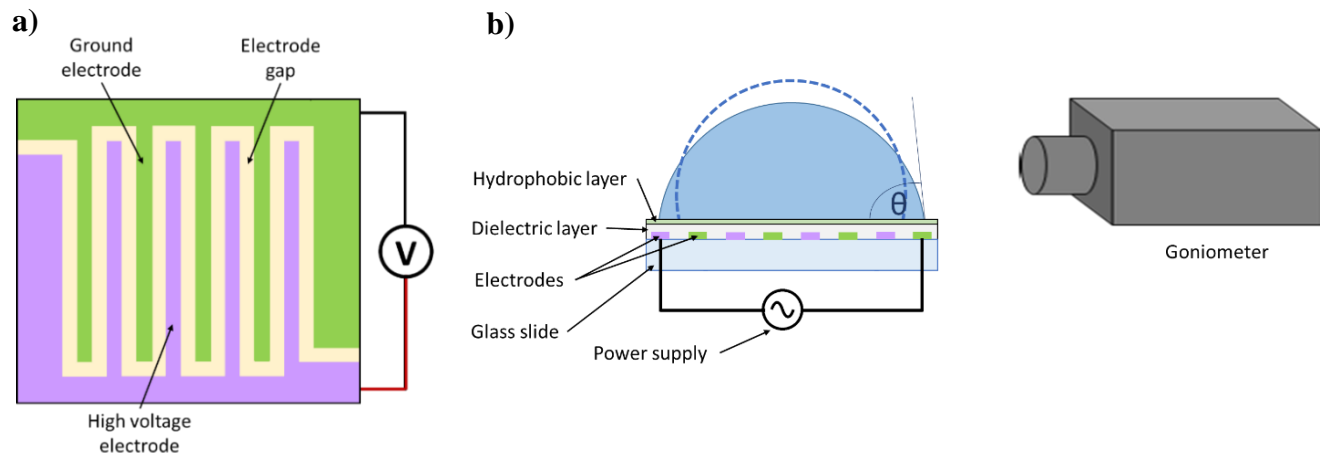
Figure 6.1. (a) Schematic showing the arrangement of interdigitated electrodes (high voltage in purple and ground in green). (b) Cross section of EW device.

Experiments involved visualization of droplet oscillations under the influence of AC electric fields, with the electric field lines directed from the high voltage electrode to the ground electrode, shown in Figure 2.6. CAs during oscillation were measured as a function of the applied voltage and frequency. For a specified AC frequency, the voltage was changed incrementally, with each voltage level held for 10 seconds during which the CA was recorded. The final reported CAs are an average of four experiments.

When studying the influence of AC frequency on EW, existing studies analyze the transient CA and transient contact radius to quantify droplet oscillation. Alternatively, in this study we quantify droplet oscillation dynamics under an AC electric field by measuring the *contact angle oscillation amplitude* (CAOA). The CAOA is defined as the difference between the cosine of the minimum ($cos\theta_{min}$) and maximum ($cos\theta_{max}$) contact angle as the droplet oscillates under a specified voltage and frequency. Mathematically, CAOA is:

$$\Delta cos\theta = cos\theta_{min} - cos\theta_{max} \qquad (6.1)$$

The minimum and maximum contact angle is obtained from the transient oscillatory cycle, as shown in Figure 6.2c. The minimum angle corresponds to maximum droplet spreading as seen in Figure 6.2a. The maximum angle corresponds to the droplets attempts to revert back to its no-voltage CA, as seen in Figure 6.2b. Droplets cycle between these two states, at a frequency twice that of the applied AC frequency (noting that the EW force does not depend on polarity of the electrodes). The magnitude of the CAOA determines the extent of droplet oscillations and its response to the voltage and frequency of the applied AC waveform. It should be noted that the CAOA is a measure of droplet oscillations and is not directly related to CA hysteresis.
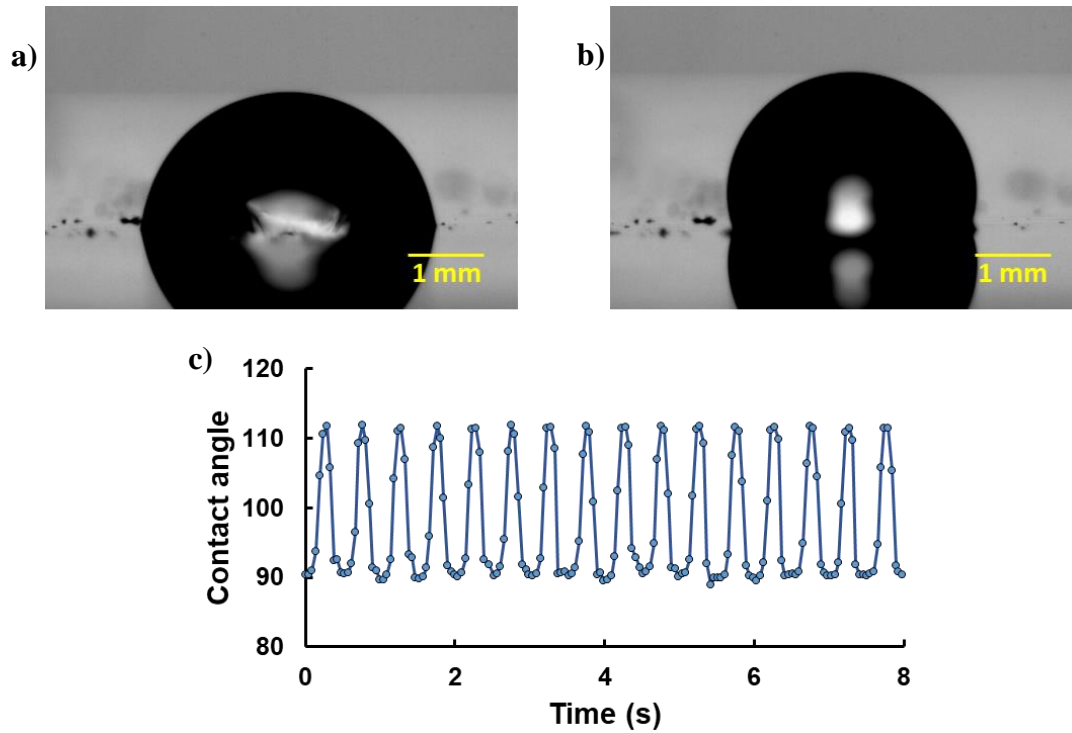
Figure 6.2. a) Minimum, and b) maximum contact angles of water droplets during oscillations under a 200 Vrms, 1 Hz applied AC waveform. c) shows the transient variation in contact angles.

6.2 MODELING DROPLET OSCILLATION DYNAMICS AND RESULTS

This section details the physics-based model developed to predict the response of a droplet to AC electric fields. Firstly, it is noted that capacitance term in Lippman's equation (Equation 2.3) should be modified to account for the non-traditional electrode geometry. In the traditional EW configuration [17], [18], [68], [119], the electric field lines inside the dielectric layer are oriented normal to the plane of the layer, and the dielectric can be considered as a parallel plate capacitor (Figure 2.5 a). The capacitance in such cases is

accurately estimated as $C_{pp} = \frac{\varepsilon_0 \varepsilon_d}{d}$, where ε_0 is the electrical permittivity of free space, ε_d is the dielectric constant and d is the thickness of the dielectric layer.

In the present coplanar electrode configuration, the field lines follow curved paths from the high voltage electrode to the ground electrode, which are on the same plane; the electric field is thus markedly different from that in the traditional configuration (Figure 2.5 and Figure 2.6). The coplanar electrode configuration, C_{cp} is described in detail in section 2.2. Importantly, for the same thickness of the dielectric layer, the capacitance of traditional configuration is significantly higher than that of the present co-planar configuration, with $\frac{C_{pp}}{C_{cp}} \sim 9$. Based on the present geometry (50 µm electrode and gap width) the electric field line penetration height will be ~70 µm above the surface[78].

The importance of using modified Lippmann's Equation to estimate the capacitance is highlighted in Figure 6.3, which shows the match between the predictions and measurements of CAs in the traditional and coplanar electrode configuration (with the same thickness of the dielectric layer). Predictions of CA are based on the Lippman's equation (Equation 2.3) with the capacitance in the traditional and coplanar electrode configurations estimated using the equation provided earlier (Equation 2.5). It is seen that the CA measurements match the predictions for the traditional configuration very well (as expected) till the onset of CA saturation (after which the CA does not decrease significantly with voltage). However, Lippman's equation with the traditional estimate for the capacitance would drastically over predict the CA change, if used for the coplanar electrode configuration. Lippman's equation with the capacitance defined by Equation 2.5 shows a good match with the experimental results for the coplanar geometry. It is noted that the measured CAs are the average of transient CA measurements taken for 10 seconds.

Figure 6.3 can also be used to estimate the threshold and saturation electric fields for the two configurations. For the coplanar electrode configuration, the threshold field and saturation electric fields are 50 V/µm, and 100 V/µm, respectively. The saturation voltage is higher than that for the traditional configuration (45 V/µm). The coplanar electrode configuration shows a reduced rate of CA change with voltage, thereby increasing the range of applied voltage over which the CA can be modulated. All of this is a consequence of the reduced capacitance in the coplanar electrode configuration. Similar results can be obtained in a traditional configuration with the use of thicker dielectric layers. Figure 6.3 implies that the use of the coplanar electrode configuration is advantageous for applications in which fine control of the CA is sought.
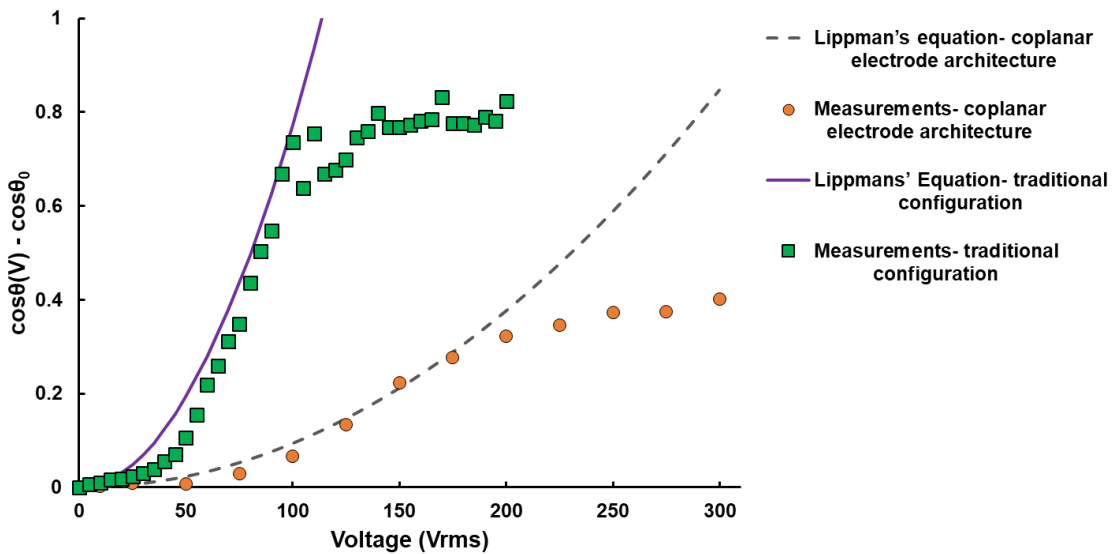
Figure 6.3: continued next page

Figure 6.3. Measured and predicted change in contact angles versus voltage for the traditional and coplanar electrode architectures. Contact angle modulation with voltage differs significantly in the two configurations for the same dielectric layer thickness.

The next step is to characterize droplet oscillations in terms of CAOA, and highlight the benefits of analyzing the voltage and frequency-dependent CAOA. Physically, CAOA captures the change in CA as the droplet oscillates, which also conveys the magnitude of the change in the shape of the droplet (using the spherical cap approximation). At low frequencies the droplet shape is significantly distorted which results in a large change in the CAOA. At high frequencies, the CAOA reduces as a direct consequence of the reduced change in the shape of the droplet (due to the reduced electrostatic forces resulting from penetration of the electric field inside the droplet). Effectively, high AC frequencies serve to negate the influence of the electric field on shape change. Figure 6.4 shows that the CAOA is higher by 10X at a 1 Hz frequency as compared to a 1 kHz frequency. The influence of frequency on wettability and oscillations is thus captured very strongly using the CAOA approach. Another advantage of the CAOA approach is its use in evaluating the threshold voltage, especially at low frequencies. The increase in CAOA defines the threshold voltage, V_{th} at which the droplet begins responding to the applied electric field ($\Delta cos\theta > 0$). Figure 6.4 shows a threshold voltage of ~90V. CAOA measurements can thus be a useful tool to quantify the threshold voltage and complement the determination of threshold voltages by tracking the change in CA versus voltage.
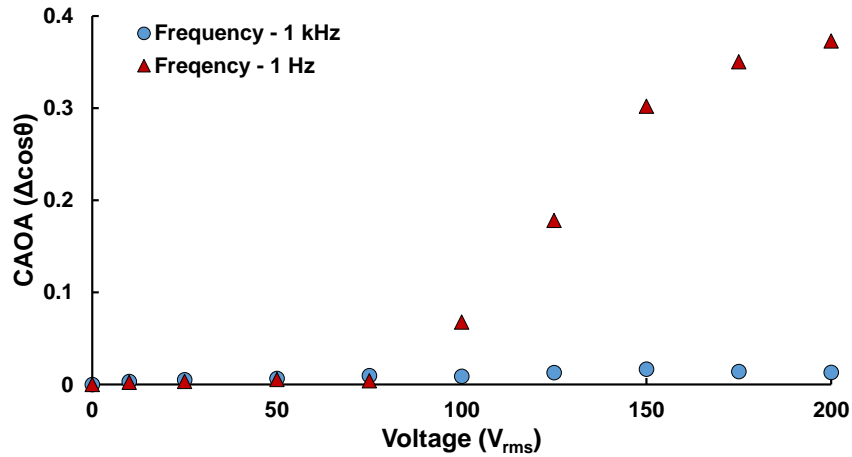
Figure 6.4. Voltage-dependent contact angle oscillation amplitude (CAOA) for two AC frequencies (1 kHz and 1 Hz). The strong influence of frequency is clearly observed with high frequencies cancelling out the influence of the applied electric field on the CAOA.

While there have been many studies on AC EW, most of them are experimental in nature. There do exist studies, which have numerically modeled the shape of oscillating droplet at various frequencies or at resonance frequencies [76], [120]–[122]. However, there are no studies which model the combined influence of voltage and frequency on contact angle oscillations. Presently, we develop a fundamentals-based and experimentally validated model to predict CAOA as a function of both voltage and frequency. The model draws from Lippmann's equation in terms of the relationship between the applied voltage and CA change; additionally, a frequency-dependent term is included, as described ahead.

Firstly, the relationship between CAOA and voltage is considered to be analogous to that between the contact angle and voltage in Lippmann's equation. In a manner analogous to the Lippmann's equation, CAOA is assumed to take the form $\Delta cos\theta(V) =$

106

$\frac{C}{\gamma_{lv}} V^2 * F(\omega)$, where $F(\omega)$ is a function of the applied AC frequency. From previous studies and present experimental data, we know that increasing the frequency will reduce the CAOA. To identify $F(\omega)$, we turn to experimental measurements of CAOA for voltages in the range of 0-250V and frequencies ranging from 1-1000Hz. Knowing that $[\Delta cos\theta(V)] = M * \left[\frac{C}{\gamma_{lv}} V^2\right]$, we use the gradient of the curve, $M = F(\omega)$ to identify the functional relationship between $F(\omega)$ and ω. The experimental data strongly suggest an exponential relationship between $F(\omega)$ and ω, resulting in an expression of the form $F(\omega) = Z_1 * exp\left(-Z_2\omega \frac{\varepsilon_0\varepsilon_D}{\sigma}\right)$. Finally, the voltage and frequency-dependent CAOA can be expressed as:

$$\Delta cos\theta(V, \omega) = Z_1 \frac{C}{\gamma_{lv}} V^2 * exp\left(-Z_2\omega \frac{\varepsilon_0\varepsilon_D}{\sigma}\right) \qquad (6.2)$$

where the angular frequency of the AC electric field is $\omega = 2\pi f$, and other terms have been previously defined. It is noted that the frequency in the exponential term is non-dimensionalized using the relaxation time. This model does involve two fitting parameters Z_1 and Z_2. These can be estimated as $Z_1 = 6, Z_2 = \frac{2}{3}$ for water, based on fitting the model with experimental data for the given range of voltages and frequencies.

The above model shows good agreement with experimental data (Figure 6.5) in the voltage range spanning from the threshold voltage V_{th} to the voltage corresponding to contact angle saturation. Below 100 V (threshold voltage) the model over predicts the CAOA; this should be expected since the model does not account for hysteresis-related effects which are important before the threshold voltage is reached. Above 200 V, the predictions diverge from experimental data; this is a direct consequence of entering the CA saturation regime. Between these two voltages, the model predicts the voltage and frequency dependent CAOA reasonably well.

At high frequencies ($\omega \rightarrow \infty$), the frequency-dependent term in Equation 6.2 becomes negligible, which leads to $\Delta cos\theta\,(V, \omega) \sim 0$ (within error). This aligns with the theory that an electrically conducting droplet will behave like a dielectric at frequencies much higher than the relaxation frequency, which will eliminate electrowettability and the resulting oscillations. At very low frequencies ($\omega \rightarrow 0$) the model shows that the influence of frequency on CAOA will reduce as the rate of oscillations reduces. The droplet has sufficient time to respond to sinusoidal waveform, and will effectively behave as a droplet under the influence of DC EW. In general, while the CAOA increases with a reduction in frequency, the increase in CAOA plateaus at low frequencies when the response time of the droplet (on the order of milli seconds) is less than the AC frequency. This can be observed through a comparison of the difference in CAOA between 1 Hz and 10 Hz, and between 1 Hz and 100 Hz, as seen in Figure 6.5.

It is noted that the model cannot be used with DC electric fields ($\omega=0$), since there are no oscillations in the CA and the model simplifies into a form similar to the Lippman's equation (which only accounts for a voltage dependence). Also, the model tends to under-predict CAOA at resonance frequencies [71] (especially at node n=2), where the largest shape oscillations are expected [71]. For the presently studied droplets the node n=2 corresponds to a resonance frequency of ~40 Hz, where the modeled CAOA is expected to be less than what would be observed.
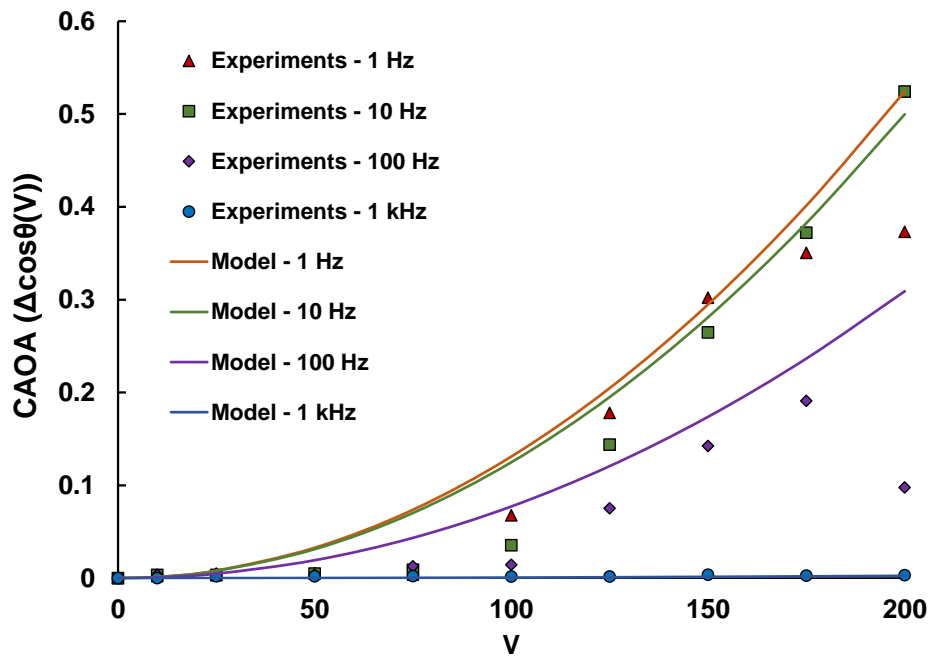
Figure 6.5. Comparison of predicted contact angle oscillation amplitudes (CAOA) with measurements (for various voltages and AC frequencies). The solid lines denote predictions and the symbols denote measurements.

While the model shows a reasonable match with experiments, it does involve two fitting parameters (Z_1 and Z_2) obtained by matching the experimental data to the model. CAOA predictions obtained from the fitting parameters show a good agreement with measurements for all combinations of voltage and frequency in this study. These fitting parameters should not be considered universal, and will need to be estimated for other fluids [123] with different surface tension and electrical properties. Conveniently, both these parameters can be obtained by fitting the model to a single set of experimental data, such as CAOA measurements for a range of voltages at a particular frequency.

Finally, the sensitivity of the predictions of CAOA to five parameters is quantified and discussed. The parameters considered include the permittivity of the droplet (ε_D) and the dielectric layer (ε_d), the electrical conductivity of the droplet (σ), surface tension (γ_{LV}) and capacitance (C). The percentage change in the CAOA as a function of the percentage change in the above parameters is shown in Figure 6.6a and b for 1 Hz and 1 kHz frequencies, respectively. It is seen that the influence of surface tension, capacitance and permittivity of the dielectric layer on CAOA is independent of frequency. An increase in surface tension will reduce droplet oscillations as higher surface tension forces will increase the resistance to changing the shape. Conversely, any increase in capacitance (by changing the electrode geometry or configuration), will increase droplet oscillations, due to larger actuation forces.

At 1 Hz, the CAOA is seen to be most sensitive to the surface tension of the liquid. However, at 1 kHz, the CAOA is most sensitive to the permittivity and the electrical conductivity of the droplet. Both these parameters relate to the electrical properties of the fluid, and determine the charge relaxation time. Increasing the electrical conductivity of the fluid will reduce the relaxation time, thereby allowing oscillations at higher frequencies; this explains the positive slope in the CAOA versus electrical conductivity curve in Figure 6.6b. Analogously, reducing the permittivity of the fluid will reduce the relaxation time, resulting in larger oscillations (larger CAOA). Understanding the impact of individual parameters on contact angle oscillations is helpful in the design and operation of any microfluidic system that relies upon droplet oscillations.

110
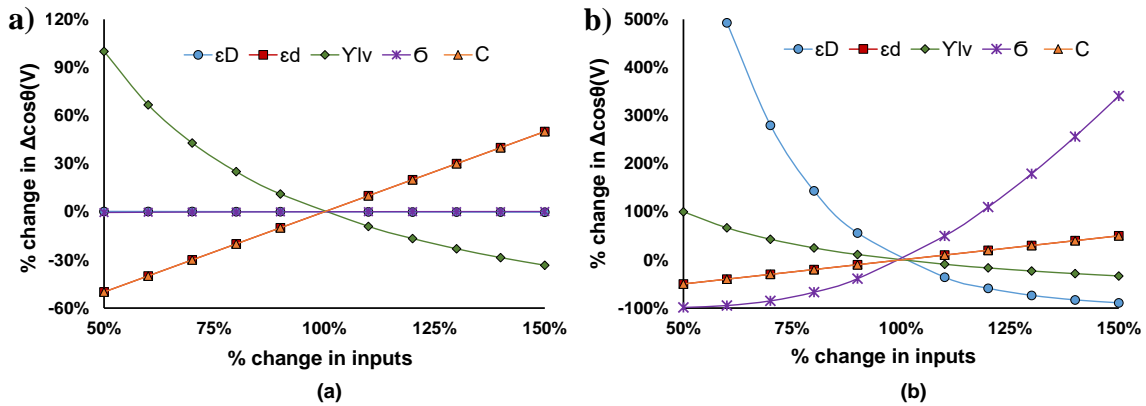
Figure 6.6. Sensitivity analysis showing the influence of various parameters on contact angle oscillation amplitude (CAOA), a) at 1 Hz and b) at 1 kHz.

6.3 CONCLUSIONS

This chapter presents a new approach to study droplet oscillations (and shapes) under AC EW. The oscillation amplitude in CAs is characterized instead of the transient variation in CAs. An experimentally validated analytical model is developed to predict the voltage and frequency-dependent CAOA for water droplets; the same approach can be applied for other liquids. Future studies can relate the CAOA to hydrodynamics and mixing patterns within droplets, that are being used as a microreactor for biology and chemistry applications. This would enable the identification of voltage and frequency regimes required to induce the desired extent of mixing through hydrodynamic or electrothermal flows. Additionally, this analysis can help understand droplet oscillation dynamics observed during dropwise condensation under AC EW, as detailed in the previous chapters.

111

Chapter 7: Conclusions and Suggestions for Future Work

This chapter summarizes the key findings emerging from this dissertation and outlines future research directions in the field of electrically enhanced condensation.

7.1 SCIENTIFIC FINDINGS AND INTELLECTUAL CONTRIBUTIONS OF THIS DISSERTATION

The body of work conducted in this dissertation is detailed in four chapters (Chapter 3 to Chapter 6). Accordingly, the conclusions and the scientific contributions are also summarized on a chapter-by chapter basis.

7.1.1 Electrowetting-based enhancement of droplet growth dynamics and heat transfer during humid air condensation

Chapter 3 studies droplet growth and roll off dynamics during condensation of humid air under a continuous electric field. This is one of the first studies that investigates the influence of EW on dropwise condensation (DWC) of water vapor. Key findings and scientific contributions of this study are as follows:

- Electrowetting can significantly influence droplet growth and roll-off dynamics.
- Higher voltages result in greater droplet growth rates.
- Frequency influences droplet growth and roll-off dynamics:
  o At low frequencies (~1 Hz) droplets translate about electrodes, at high frequencies droplets oscillate in place.
  o High frequencies (~10 kHz) lead to faster droplet growth and larger condensation rates.

o At low frequencies (~1 Hz) droplet roll-off size decreases and roll-off frequency increases.

- The influence of humid air and non-condensable gases (NCG) layer around a droplet can be incorporated into classical thermal resistance-based heat transfer models.

- EW can enhance heat transfer rates by >30%.

7.1.2 Statistical Modeling of Electrowetting-Induced Droplet Coalescence

Chapter 4 is the first-ever study of its kind that analyses electric field-induced droplet coalescence dynamics using machine learning-based approaches. Statistical data science-based models are used to analyze experimental data to identify the key parameters that influence EW enhanced droplet coalescence. Key findings and scientific contributions of this study are as follows:

- The two key parameters that influence droplet coalescence are the applied voltage and the electrode width (both of these are incorporated in one parameter, namely the electric field).

- AC frequency plays a negligible role in droplet coalescence.

- Machine learning-based statistical parameter shrinkage and regression algorithms can be used to identify trends in coalescence dynamics.

- Change in droplet size distributions can be categorized via the change in i) area average droplet radius, ii) wetted area ratio, and via the spread of the distribution.

- Statistical machine learning algorithms can be used as a reference tool to predict the change in droplet size distribution as a function of the applied electric field.

7.1.3 AC electrowetting promoted droplet shedding on hydrophobic surfaces

Chapter 5 presents the first-ever detailed analysis of droplet roll-off dynamics under the influence of an electric field. It is seen that the voltage and frequency determine the extent and rate, respectively, of water removal. Key findings and scientific contributions of this study are as follows:

- EW enables almost complete removal of water (dry area fraction>95%) in very short time durations (~1 second).

- Significant water shedding can be achieved without needing to apply voltages significantly higher than the threshold voltage.

- The frequency of the AC waveform does not influence the dry area fraction for voltages above the threshold voltage.

- The time required to shed droplets, or 'de-wetting time constant' strongly depends on the AC frequency.

- Orientation of the device influences water removal due to electrostatic pinning of the droplets.

- Measured water removal mass fluxes immediately after the application of an EW field are two orders of magnitude higher than those achieved from steady state condensation with a continuous field applied; this highlights the benefits of periodic EW fields as opposed to continuous EW fields.

7.1.4 Characterization of oscillation amplitude of contact angle during AC electrowetting of water droplets

Chapter 6 presents an experimentally validated, fundamentals-based model to predict contact angle oscillation amplitude of water droplets as a function of AC voltage and frequency. Key findings and scientific contributions of this study are as follows:

- Identified new analytical correlation to model capacitance for electrowetting on co-planar electrodes geometry.

- Developed a new method for characterizing droplet oscillation dynamics, via tracking the contact angle oscillation amplitude.

- Related the contact angle oscillation amplitude to both voltage and AC frequency .

- Modified the well-known Lippmann Equation to include the influence of AC frequency (along with voltage) on change in contact angle – analytical model was compared with experiments.

7.1.5 Selection of dielectric materials

Dielectric materials are a vital part of electrowetting devices as they isolate the conductive droplet from the electrodes, prevent current flow and store capacitive energy responsible for EW-based actuation. The attributes of a good dielectric material include high electrical breakdown strength, high dielectric constant, pinhole free nature, good adhesion and moisture resistance. Finding suitable dielectric materials with all the above mentioned properties has been a long-time challenge for the EW community. In the present work, additional challenges arose due to the presence of copious amounts of water in the

EW systems. Three dielectric materials were utilized in the work described in this dissertation, and are briefly discussed in this sub-section.

The three dielectric materials used in the presented studies include: i) Cytop, which is a hydrophobic fluoropolymer material, ii) Parylene C which is a polymeric material, and iii) SU-8 2005 which is an epoxy-based photoresist. Table 7.1 shows the dielectric properties of the materials used in this study.

Dielectric material	Dielectric constant	Dielectric strength (V/µm)	Thickness of coating (µm)
Cytop	2.1	150	2
Parylene C	3.2	270	2
SU-8 2005	3.2	100	5

Table 7.1. Properties of dielectric materials used in study

The study described in Chapter 3 utilized Cytop as the EW dielectric. A major advantage of Cytop is that it is hydrophobic in nature, which obviates the need for an additional hydrophobic coating. However, it was found that under the influence of an electric field and under high moisture conditions, Cytop had low durability. Additionally, when Cytop was coated as a single layer, the presence of pinholes was observed to be a problem. Parylene C is a commonly used dielectric material in the EW community due to its high breakdown voltage and dielectric constant; conformal coatings can be fabricated via room temperature vapor deposition. However, low adhesion to glass in the presence of high moisture caused delamination of the Parylene C coating. SU-8 was also used as the EW dielectric material in some of the studies mentioned in this dissertation. However, SU8

coatings are inherently thick (due to higher viscosity). Good adhesion to glass was observed, which is an advantage, compared to Paryene C. However, the low dielectric strength of SU-8 limits the magnitude of the applied electric field.

7.2. SUGGESTIONS FOR FUTURE WORK

Suggestions for future research on topics related to the content of this dissertation are outlined ahead.

7.2.1 Using traveling electric fields to sweep away condensed droplets

In addition to the explored approaches for accelerating droplet coalescence/growth, electric fields can also be utilized to actively pump the condensed droplets away, using a traveling electric field. EW is a powerful technique to move fluids as droplets [63], [64]. By actively pumping the droplets away, condensate removal can be significantly enhanced as compared to gravity-assisted shedding. A travelling electric field can be generated using dielectrophoretic or electrowetting forces. Under the dielectrophoretic effect, a neutral particle is polarized under a non-uniform electric field such that the voltage, frequency and dielectric properties determine the magnitude and direction of the induced dipole [124], [125]. Such a system can be developed using a 3-phase traveling electric field which can ensure a preferred direction for sweeping the condensate away. Figure 7.1 schematically shows the electrode arrangement to actively pump condensate off the surface.

As an alternative method, EW can be used to pump droplets off the surface using electrowetting on dielectric based droplet movement methods [63], [64]. Such a system would involve an open plate coplanar electrowetting configuration where the ground

electrode would be in parallel with individually addressable electrodes that would control droplet pumping [126]. This open plate system would be advantageous as condensation can occur unobstructed by the presence of a top plate. This study would demonstrate removal of droplets at smaller sizes and higher rates than would be possible with non-traveling electric field-assisted condensation. The minimum size of the droplet that would be pumped will depend on the electrode width and switching frequency.
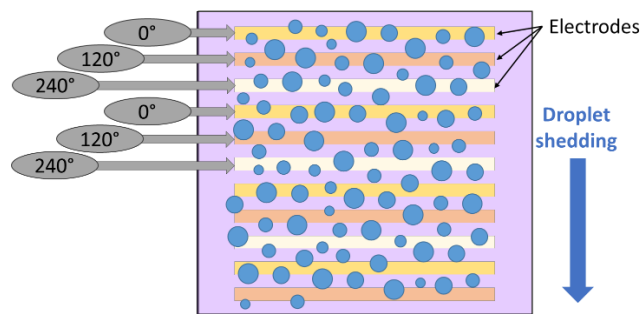
Figure 7.1. Electrode geometry and phase shift design for travelling electric field assisted condensation.

7.2.2 Acoustics driven coalescence

Similar to electric fields, acoustics has also been used as an active method to enhance droplet coalescence and roll-off during DWC. When the surface is vibrated at the resonant frequency, it has been shown that droplet coalescence and shedding is enhanced, and the droplet departure time and size can be reduced. All these improvements result in a substantial increase in heat transfer [127], [128]. However, this method has its disadvantages, since these mechanical vibrations can only remove droplets of sizes that have resonant frequencies equal to or a harmonic multiple of the applied frequency.

118

Additionally, subjecting a physical structure to prolonged vibration can lead to failure owing to fatigue resulting from stress cycles.

Alternatively, a different approach can be used to coalesce droplets by avoiding mechanical vibrations of the condensing surface. Standing waves have been used to move or levitate droplets [129]. In a droplet levitation system, a transducer is used to generate a wave which is reflected by a reflector, this creates a standing wave. A droplet can be in equilibrium where the acoustic pressure force balances the gravitational force, causing it to levitate at the nodes of the standing wave. By applying a similar concept to a droplet size distribution on a surface, a standing wave can be used to push droplets from high pressure points to the nodal lines, thereby causing droplets to accumulate and coalesce at these nodes.

Acoustic agglomeration is another method of using sound waves to coalesce droplets. Acoustic agglomeration is the process in which acoustic waves are used to manipulate the motion of airborne particles and in the process, promote collisions that lead to the formation of agglomerates (clustering of particles). Under these acoustic waves, smaller particles tend to follow the acoustic vibrations closely, while larger particles rarely move with acoustic waves due to their larger inertia. Consequently, the relative motions between the different sized particles result in collisions. Most acoustic agglomeration related application focus on airborne particles, aerosols, and air pollutants such as smoke, fly ash, and coal dust. However, similar concepts can be applied to micron sized water droplets in air sitting on hydrophobic surface. Although mechanically vibrating a surface has been found to enhance CHT, other methods described in this section have not been explored and hold promise for enhancing droplet coalescence and roll-off during DWC.

Appendix A: Flared natural gas-based onsite atmospheric water harvesting (AWH) for oilfield operations [22]

Abstract: Natural gas worth tens of billions of dollars is flared annually, which leads to resource waste and environmental issues. This work introduces and analyzes a novel concept for flared gas utilization, wherein the gas that would have been flared is instead used to condense atmospheric moisture. Natural gas, which is currently being flared, can alternatively power refrigeration systems to generate the cooling capacity for large scale atmospheric water harvesting (AWH). This approach solves two pressing issues faced by the oil–gas industry, namely gas flaring, and sourcing water for oilfield operations like hydraulic fracturing, drilling and water flooding. Multiple technical pathways to harvest atmospheric moisture by using the energy of natural gas are analyzed. A modeling framework is developed to quantify the dependence of water harvest rates on flared gas volumes and ambient weather. Flaring patterns in the Eagle Ford Shale in Texas and the Bakken Shale in North Dakota are analyzed to quantify the benefits of AWH. Overall, the gas currently flared annually in Texas and North Dakota can harvest enough water to meet 11% and 65% of the water consumption in the Eagle Ford and the Bakken, respectively. Daily harvests of upto 30,000 and 18,000 gallons water can be achieved using the gas currently flared per well in Texas and North Dakota, respectively. In fifty Bakken sites, the water required for fracturing or drilling a new well can be met via onsite flared gasbased AWH in only 3 weeks, and 3 days, respectively. The benefits of this concept are quantified for the Eagle Ford and Bakken Shales. Assessments of the global potential of this concept are presented using data from countries with high flaring activity. It is seen that this waste-

to-value conversion concept offers significant economic benefits while addressing critical environmental issues pertaining to oil– gas production.

Appendix B: Modeling humid air condensation in waste natural gas-powered atmospheric water harvesting systems [60]

Abstract: 4% of the natural gas produced globally is flared at oilfields due to the absence of gas handling infrastructure and unfavorable economics. Recent work has proposed the utilization of this excess gas for atmospheric water harvesting (AWH) for oilfield operations, wherein gas-powered refrigeration cycles generate the cooling capacity for large scale dehumidification, via condensation. This work develops an indepth, comprehensive, analytical modeling framework to predict the water condensation in waste gas-powered AWH systems. Firstly, gas powered refrigeration systems are analyzed to identify key system parameters and considerations. Secondly, an analytical model is developed to capture the complex heat and mass transfer phenomena associated with condensation of humid air in a fin and tube heat exchanger. This involves using heat and mass transfer relations to estimate the dehumidification process line. The model can predict the water condensation rate as a function of the gas flow rate, ambient weather and the refrigeration system utilized. The model is used to predict flared gas-based water harvests in the Eagle Ford (Texas) and Bakken (North Dakota) Shale oilfields, which account for the majority of US flaring. Results indicate that 1 cubic meter of natural gas can condense 2.3 and 0.65 gallons water (on an annual average basis) in Texas and North Dakota, respectively. The weather-dependent condensation rates range from 3 to 10 (Texas) and 0 to 0.8 (North Dakota) gallons/day/square meter of condenser area. Overall, flared gas-based AWH can utilize 77% and 40% of the excess gas in Texas and North Dakota, respectively. This work analyzes various aspects of humid air condensation and evaluates the sensitivity of the condensation rate to key engineering parameters. Overall, this work

develops the foundational modeling tool to predict the performance of all types of humid air condensation systems.

Appendix C: Landfill gas-powered atmospheric water harvesting for oilfield operations in the United States [21]

Abstract: Landfill gas accounts for 18% of US greenhouse gas emissions. The energy wasted via venting/flaring methane in landfill gas can be valued at 7.5 billion USD (annually). This work presents a novel utilization concept, wherein landfill gas-powered refrigeration enables large-scale atmospheric water harvesting, via dehumidification. This work analyzes the potential of landfill gas-powered atmospheric water harvesting towards meeting the water requirements of oilfields located near landfills. Heat and mass transfer-based analytical modeling is used to estimate the seasonal water harvest, and techno-economic analyses are presented to quantify the benefits for US oilfields. This technology is seen to be attractive for the Barnett Shale (Texas) and Kern County (California), which can be served by 30 landfills each, and are located in hot-humid and water-stressed areas. Results show that landfill gas-powered water harvesting can meet 34% of water requirements (hydraulic fracturing) in the Barnett Shale and 12–26% of water requirements (enhanced oil recovery) in Kern County oilfields, respectively. Landfill gas projects are economically more viable in the Barnett as compared to Kern County. The impact of landfill gas-powered water harvesting on CO2e emissions from landfills is quantified. Constraints and challenges associated with water harvesting are discussed. Importantly, this waste-to-value concept has worldwide relevance since landfills co-exist with population centers.

Appendix D: Characterizing Microfluidic Operations Underlying an Electrowetting Heat Pipe on the International Space Station [130]

Abstract: Electrowetting heat pipes (EHPs) are a newly conceptualized class of heat pipes, wherein the adiabatic wick section is replaced by electrowetting-based pumping of the condensate (as droplets) to the evaporator. Specific advantages include the ability to transport high heat loads over long distances, low thermal resistance and power consumption, and the absence of moving mechanical parts. In this work, we describe characterization of key microfluidic operations (droplet motion and splitting) underlying the EHP on the International Space Station (ISS). A rapid manufacturing method was used to fabricate the electrowetting device on a printed circuit board. Key device-related considerations were to ensure reliability and package the experimental hardware within a confined space. Onboard the ISS, experiments were conducted to study electrowetting-based droplet motion and droplet splitting, by imaging droplet manipulation operations via pre-programmed electrical actuation sequences. An applied electric field of 36 Volts/um resulted in droplet speeds approaching 10 mm/s. Droplet splitting dynamics was observed and the time required to split droplets was quantified. Droplet motion data was analyzed to estimate the contact line friction coefficient. Overall, this demonstration is the first-ever electrowetting experiment in space. The obtained results are useful for future design of the EHP and other electrowetting-based systems for microgravity applications. The testing was performed under the Advanced Passive Thermal eXperiment (APTx) project, a project to test a suite of passive thermal control devices funded by the ISS Technology Demonstration Office at NASA JSC.

Appendix E: Scalably manufactured textured surfaces for controlling wettability in oil-water systems [131]

Abstract: Competitive wettability in oil-water systems influences applications such as oil-water separation and enhanced oil recovery. Here, we study the wettability of water (in oil) and oil (in water) on sub-millimeter/micro/nano textured surfaces fabricated on a variety of substrates (metals, polymers, elastomers). Importantly, all the fabrication processes employed involved non-cleanroom-based scalable techniques. Metal surfaces were fabricated via wet etching processes and polymer/elastomer surfaces were fabricated via laser etching. These fabrication techniques can enable texturing with sub-millimeter, micron and sub-micron feature sizes. Wettability was characterized by measuring static contact angle and dynamic contact angle (roll-off angle). Several insights into wettability are obtained from this work. Firstly, textured metal surfaces with low energy surface chemistry showed the lowest adhesion to water and oil droplets. Textured metal surfaces coated with Teflon AF were superhydrophobic (in oil) with very low roll-off angles (4°–7°). Uncoated textured metal surfaces were superoleophobic (in water) with roll-off angles of 3°–9°. Secondly, textured polymer and elastomer surfaces exhibited utrahydrophobicity (in oil); however not all textured elastomers exhibited superoleophobicity (in water). Thirdly, no droplet roll-off was observed on any textured elastomer and polymer surface, despite very favourable contact angles. This indicates that high contact angles do not always translate to superhydrophobicity/oleophobicity. Fourthly, it is seen that competitive wettability of a surface can be understood by analysing the corresponding water and oil wettability of that surface in an air environment. Additionally, the initial state of the surface can be important, as the first fluid in contact with the surface fills the porous textures, and

dictates subsequent wettability. All these findings and insights position this work as the foundation for more detailed studies on the development of surfaces for specific applications.

References

[1] J. W. Rose, "Condensation Heat Transfer Fundamentals," *Chem. Eng. Res. Des.*, vol. 76, no. 2, pp. 143–152, 1998.

[2] E. Schmidt, W. Schurig, and W. Sellschopp, "Experiments on the condensation of water vapor in film and drop form," *Eng. Mech. Thermodyn.*, vol. 1, no. 2, pp. 53–63, 1930.

[3] B. Mondal, M. Mac Giolla Eain, Q. F. Xu, V. M. Egan, J. Punch, and A. M. Lyons, "Design and Fabrication of a Hybrid Superhydrophobic-Hydrophilic Surface That Exhibits Stable Dropwise Condensation," *ACS Appl. Mater. Interfaces*, vol. 7, no. 42, pp. 23575–23588, 2015.

[4] C. W. Lo, Y. C. Chu, M. H. Yen, and M. C. Lu, "Enhancing Condensation Heat Transfer on Three-Dimensional Hybrid Surfaces," *Joule*, vol. 3, no. 11, pp. 2806–2823, 2019.

[5] N. Miljkovic, R. Enright, and E. N. Wang, "Modeling and Optimization of Superhydrophobic Condensation," *J. Heat Transfer*, vol. 135, no. 11, p. 111004, 2013.

[6] Y. Hou, M. Yu, X. Chen, Z. Wang, and S. Yao, "Recurrent filmwise and dropwise condensation on a beetle mimetic surface," *ACS Nano*, vol. 9, no. 1, pp. 71–81, 2015.

[7] A. Ghosh, S. Beaini, B. J. Zhang, R. Ganguly, and C. M. Megaridis, "Enhancing Dropwise Condensation through Bioinspired Wettability Patterning," *Langmuir*, vol. 30, p. 13103−13115, 2014.

[8] P. B. Weisensee, Y. Wang, Q. Hongliang, D. Schultz, W. P. King, and N. Miljkovic, "Condensate droplet size distribution on lubricant-infused surfaces," *Int. J. Heat Mass Transf.*, vol. 109, pp. 187–199, 2017.

[9] S. Anand, A. T. Paxson, R. Dhiman, J. D. Smith, and K. K. Varanasi, "Enhanced condensation on lubricant-impregnated nanotextured surfaces," *ACS Nano*, vol. 6, no. 11, pp. 10122–10129, 2012.

[10] X. Yan *et al.*, "Droplet Jumping: Effects of Droplet Size, Surface Structure, Pinning, and Liquid Properties," *ACS Nano*, p. acsnano.8b06677, 2019.

[11] N. Miljkovic *et al.*, "Jumping-droplet-enhanced condensation on scalable superhydrophobic nanostructured surfaces," *Nano Lett.*, vol. 13, no. 1, pp. 179–187, 2013.

[12] D. Baratian, R. Dey, H. Hoek, D. Van Den Ende, and F. Mugele, "Breath Figures under Electrowetting: Electrically Controlled Evolution of Drop Condensation

Patterns," *Phys. Rev. Lett.*, vol. 120, no. 21, p. 214502, 2018.

[13] R. Dey, J. Gilbers, D. Baratian, H. Hoek, D. van den Ende, and F. Mugele, "Controlling shedding characteristics of condensate drops using electrowetting," *Appl. Phys. Lett.*, vol. 113, 2018.

[14] R. Yan and C.-L. Chen, "Condensation Droplet Distribution Regulated by Electrowetting," *J. Heat Transfer*, vol. 141, no. 11, 2019.

[15] E. D. Wikramanayake and V. Bahadur, "Electrowetting-based enhancement of droplet growth dynamics and heat transfer during humid air condensation," *Int. J. Heat Mass Transf.*, vol. 140, pp. 260–268, 2019.

[16] S. Högnadóttir, K. Kristinsson, H. G. Thormar, and K. Leosson, "Increased droplet coalescence using electrowetting on dielectric (EWOD)," *Appl. Phys. Lett.*, vol. 116, no. February, p. 073702, 2020.

[17] F. Mugele and J.-C. Baret, "Electrowetting: from basics to applications," *J. Phys. Condens. Matter*, vol. 17, no. 28, pp. R705–R774, Jul. 2005.

[18] L. Chen and E. Bonaccurso, "Electrowetting — From statics to dynamics," *Adv. Colloid Interface Sci.*, vol. 210, pp. 2–12, Aug. 2014.

[19] J. Ma, H. Cha, M. Kim, D. G. Cahill, and N. Miljkovic, "Condensation Induced Delamination of Nanoscale Hydrophobic Films," *Adv. Funct. Mater.*, vol. 29, no. 43, p. 1905222, Oct. 2019.

[20] Y. Tu, R. Wang, Y. Zhang, and J. Wang, "Progress and Expectation of Atmospheric Water Harvesting," *Joule*, vol. 2, no. 8. Cell Press, pp. 1452–1475, 15-Aug-2018.

[21] E. D. Wikramanayake, O. Ozkan, and V. Bahadur, "Landfill gas-powered atmospheric water harvesting (AWH) for oilfield operations in the United States," *Energy*, vol. 138, pp. 647–658, 2017.

[22] E. D. Wikramanayake and V. Bahadur, "Flared natural gas-based onsite atmospheric water harvesting (AWH) for oilfield operations," *Environ. Res. Lett.*, vol. 11, no. 3, p. 034024, 2016.

[23] I. Nayshevsky, Q. Xu, and A. M. Lyons, "Hydrophobic-Hydrophilic Surfaces Exhibiting Dropwise Condensation for Anti-Soiling Applications," *IEEE J. Photovoltaics*, vol. 9, no. 1, pp. 302–307, 2019.

[24] Y. Zhao, Y. Liu, Q. Xu, M. Barahman, and A. M. Lyons, "Catalytic, self-cleaning surface with stable superhydrophobic properties: Printed polydimethylsiloxane (PDMS) arrays embedded with TiO2 nanoparticles," *ACS Appl. Mater. Interfaces*, vol. 7, no. 4, pp. 2632–2640, 2015.

[25] R. Blossey, "Self-cleaning surfaces - Virtual realities," *Nat. Mater.*, vol. 2, no. 5, pp.

301–306, 2003.

[26] F. P. Incropera, D. P. DeWitt, T. L. Bergman, and A. S. Lavine, "Fundamentals of Heat and Mass Transfer," in *6th Edition*, WILEY, 2006.

[27] J. H. Pu, J. Sun, Q. Sheng, W. Wang, and H. S. Wang, "Dependences of Formation and Transition of the Surface Condensation Mode on Wettability and Temperature Difference," *Langmuir*, vol. 36, no. 1, pp. 456–464, 2020.

[28] R. N. Leach, F. Stevens, S. C. Langford, and J. T. Dickinson, "Dropwise condensation: experiments and simulations of nucleation and growth of water drops in a cooling system.," *Langmuir*, vol. 22, no. 3, pp. 8864–8872, 2006.

[29] J. E. Castillo, J. a. Weibel, and S. V. Garimella, "The effect of relative humidity on dropwise condensation dynamics," *Int. J. Heat Mass Transf.*, vol. 80, pp. 759–766, 2015.

[30] N. Watanabe, M. Aritomi, and A. Machida, "Time-series characteristics and geometric structures of drop-size distribution density in dropwise condensation," *Int. J. Heat Mass Transf.*, vol. 76, pp. 467–483, Sep. 2014.

[31] J. B. Boreyko and C. Chen, "Self-Propelled Dropwise Condensate on Superhydrophobic Surfaces," vol. 184501, no. October, pp. 2–5, 2009.

[32] S. Kim and K. J. Kim, "Dropwise Condensation Modeling Suitable for Superhydrophobic Surfaces," *J. Heat Transfer*, vol. 133, no. 8, p. 081502, 2011.

[33] V. P. Carey, *Liquid-vapor phase-change phenomena: an introduction to the thermophysics of vaporization and condensation processes in heat transfer equipment*, 2nd ed. Taylor and Francis, 2008.

[34] J. W. Rose, "Dropwise condensation theory and experiment: A review," *Proc. Inst. Mech. Eng. Part A J. Power Energy*, vol. 216, no. 2, pp. 115–128, 2002.

[35] X. Yan, L. Feng, L. Zhang, S. Sett, L. Li, and N. Miljkovic, "'Dancing Droplets': Partial Coalescence on Superhydrophobic Surfaces," *J. Heat Transfer*, vol. 142, no. 3, Mar. 2020.

[36] Y. Nam, D. Seo, C. Lee, and S. Shin, "Droplet coalescence on water repellant surfaces," *Soft Matter*, vol. 11, no. 1, pp. 154–160, 2015.

[37] D. M. Anderson *et al.*, "Using amphiphilic nanostructures to enable long-range ensemble coalescence and surface rejuvenation in dropwise condensation," *ACS Nano*, vol. 6, no. 4, pp. 3262–3268, 2012.

[38] K. Rykaczewski, A. T. Paxson, S. Anand, X. Chen, Z. Wang, and K. K. Varanasi, "Multimode Multidrop Serial Coalescence Effects during Condensation on Hierarchical Superhydrophobic Surfaces," 2013.

[39] R. Enright, N. Miljkovic, J. Sprittles, K. Nolan, R. Mitchell, and E. N. Wang, "How coalescing droplets jump," *ACS Nano*, vol. 8, no. 10, pp. 10352–10362, 2014.

[40] M. Roudgar and J. De Coninck, "Condensation heat transfer coefficient versus wettability," *Appl. Surf. Sci.*, vol. 338, pp. 15–21, 2015.

[41] D. Attinger *et al.*, "Surface engineering for phase change heat transfer: A review," *MRS Energy Sustain.*, vol. 1, p. E4, 2014.

[42] K. Hou, X. Li, Q. Li, and X. Chen, "Tunable Wetting Patterns on Superhydrophilic/Superhydrophobic Hybrid Surfaces for Enhanced Dew-Harvesting Efficacy," *Adv. Mater. Interfaces*, vol. 7, no. 2, p. 1901683, Jan. 2020.

[43] S. Wang *et al.*, "Bioinspired hierarchical copper oxide surfaces for rapid dropwise condensation," *J. Mater. Chem. A*, vol. 5, no. 40, pp. 21422–21428, Oct. 2017.

[44] D. Orejon, A. Askounis, Y. Takata, and D. Attinger, "Dropwise Condensation on Multiscale Bioinspired Metallic Surfaces with Nanofeatures," *ACS Appl. Mater. Interfaces*, vol. 11, no. 27, pp. 24735–24750, Jul. 2019.

[45] L. Guo and G. H. Tang, "Dropwise condensation on bioinspired hydrophilic-slippery surface," *RSC Adv.*, vol. 8, no. 69, pp. 39341–39351, Nov. 2018.

[46] H. Cha *et al.*, "Dropwise condensation on hydrophilic surfaces," *Sci. Adv.*, vol. 6, 2020.

[47] A. Azar, V. Bahadur, A. Kulkarni, M. Yamada, and J. A. Ruud, "Hydrophobic surfaces for control and enhancement of water phase transitions," *MRS Bull. Interfacial Mater. with Spec. Wettability*, vol. 38, no. 5, pp. 407–411, 2013.

[48] J. Huang, J. Zhang, and L. Wang, "Review of vapor condensation heat and mass transfer in the presence of non-condensable gas," *Appl. Therm. Eng.*, vol. 89, pp. 469–484, 2015.

[49] Y. Zhao, D. J. Preston, Z. Lu, L. Zhang, J. Queeney, and E. N. Wang, "Effects of millimetric geometric features on dropwise condensation under different vapor conditions," *Int. J. Heat Mass Transf.*, vol. 119, pp. 931–938, 2018.

[50] S. Zheng, F. Eimann, C. Philipp, T. Fieback, and U. Gross, "Modeling of heat and mass transfer for dropwise condensation of moist air and the experimental validation," *Int. J. Heat Mass Transf.*, vol. 120, pp. 879–894, 2018.

[51] S. Zheng, F. Eimann, C. Philipp, T. Fieback, and U. Gross, "Experimental and modeling investigations of dropwise condensation out of convective humid air flow," *Int. J. Heat Mass Transf.*, vol. 151, p. 119349, 2020.

[52] X. Ma, X. Zhou, Z. Lan, Y. Li, and Y. Zhang, "Condensation heat transfer enhancement in the presence of non-condensable gas using the interfacial effect of

dropwise condensation," vol. 51, pp. 1728–1737, 2008.

[53] V. G. Reifert, A. I. Sardak, S. V. Grigorenko, and V. L. Podbereznyj, "Heat exchange at dropwise condensation in heat exchangers of desalination plants," *Desalination*, vol. 74, pp. 373–382, Jan. 1989.

[54] S. Parekh, M. M. Farid, J. R. Selman, and S. Al-hallaj, "Solar desalination with a humidification-dehumidification technique — a comprehensive technical review," *Desalination*, vol. 160, no. 2, pp. 167–186, Jan. 2004.

[55] E. Bar, "Extraction of water from air - An alternative solution for water supply," *Desalination*, vol. 165, no. SUPPL., p. 335, Aug. 2004.

[56] S. Algarni, C. A. Saleel, and M. A. Mujeebu, "Air-conditioning condensate recovery and applications—Current developments and challenges ahead," *Sustain. Cities Soc.*, vol. 37, pp. 263–274, Feb. 2018.

[57] O. Klemm *et al.*, "Fog as a fresh-water resource: Overview and perspectives," *Ambio*, vol. 41, no. 3, pp. 221–234, 2012.

[58] K.-C. Park, S. S. Chhatre, S. Srinivasan, R. E. Cohen, and G. H. McKinley, "Optimal Design of Permeable Fiber Network Structures for Fog Harvesting," *Langmuir*, vol. 29, no. 43, pp. 13269–13277, Oct. 2013.

[59] R. V Wahlgren, "Atmospheric water vapour processors designs for potable water production: a review," *Elsevier*, vol. 35, no. 1, pp. 1–22, 2001.

[60] O. Ozkan, E. D. Wikramanayake, and V. Bahadur, "Modeling humid air condensation in waste natural gas-powered atmospheric water harvesting systems," *Appl. Therm. Eng.*, vol. 118, pp. 224–232, May 2017.

[61] H. Kim *et al.*, "Adsorption-based atmospheric water harvesting device for arid climates," *Nat. Commun.*, vol. 9, no. 1, Mar. 2018.

[62] G. Lippmann, "Relations entre les phénomènes électriques et capillaires," *Gauthier-Villars*, 1975.

[63] V. Bahadur and S. V. Garimella, "An energy-based model for electrowetting-induced droplet actuation," *J. Micromechanics Microengineering*, vol. 6, pp. 1494–1503, 2006.

[64] N. Kumari, V. Bahadur, and S. V. Garimella, "Electrical actuation of electrically conducting and insulating droplets using ac and dc voltages," *J. Micromechanics Microengineering*, vol. 18, no. 10, 2008.

[65] R. Malk, Y. Fouillet, and L. Davoust, "Rotating flow within a droplet actuated with AC EWOD," *Sensors Actuators B Chem. B Chem.*, vol. 154, no. 2, pp. 191–198, 2011.

[66] P. Sen and C. J. Kim, "Capillary spreading dynamics of electrowetted sessile droplets in air," *Langmuir*, vol. 25, no. 8, pp. 4302–4305, 2009.

[67] T. Yamada, T. Sugimoto, Y. Higashiyama, M. Takeishi, and T. Aoki, "Resonance phenomena of a single water droplet located on a hydrophobic sheet under AC electric field," *IEEE Trans. Ind. Appl.*, vol. 39, no. 1, pp. 59–65, 2003.

[68] S. H. Ko, H. Lee, and K. H. Kang, "Hydrodynamic flows in electrowetting," *Langmuir*, vol. 24, no. 3, pp. 1094–1101, 2008.

[69] F. J. Hong, D. D. Jiang, and P. Cheng, "Frequency-dependent resonance and asymmetric droplet oscillation under ac electrowetting on coplanar electrodes," *J. Micromechanics Microengineering*, vol. 22, no. 8, 2012.

[70] P. García-Sánchez, A. Ramos, and F. Mugele, "Electrothermally driven flows in ac electrowetting," *Phys. Rev. E - Stat. Nonlinear, Soft Matter Phys.*, vol. 81, no. 1, pp. 1–4, 2010.

[71] J. M. Oh, S. H. Ko, and K. H. Kang, "Shape oscillation of a drop in ac electrowetting," *Langmuir*, vol. 24, no. 15, pp. 8379–8386, 2008.

[72] F. Mugele, J. C. Baret, and D. Steinhauser, "Microfluidic mixing through electrowetting-induced droplet oscillations," *Appl. Phys. Lett.*, vol. 88, no. 20, 2006.

[73] H. Lee, S. Yun, S. H. Ko, and K. H. Kang, "An electrohydrodynamic flow in ac electrowetting," *Biomicrofluidics*, vol. 3, no. 4, pp. 1–12, 2009.

[74] S. Dash, N. Kumari, and S. V. Garimella, "Frequency-dependent transient response of an oscillating electrically actuated droplet," *J. Micromechanics Microengineering*, vol. 22, no. 7, 2012.

[75] J. Lee, H. Moon, J. Fowler, T. Schoellhammer, and C.-J. Kim, "Electrowetting and electrowetting-on-dielectric for microscale liquid handling," *Sensors Actuators A Phys.*, vol. 95, pp. 259–268, 2002.

[76] R. Malk, A. Rival, Y. Fouillet, and L. Davoust, "EWOD in Coplanar Electrode Configurations," in *ASME 2010 8th International Conference on Nanochannels, Microchannels, and Minichannels collocated with 3rd Joint US-European Fluids Engineering Summer Meeting*, 2010, pp. 239–248.

[77] F. Li and F. Mugele, "How to make sticky surfaces slippery: Contact angle hysteresis in electrowetting with alternating voltage," *Appl. Phys. Lett.*, vol. 92, no. 24, pp. 1–4, 2008.

[78] J. Z. Chen, A. A. Darhuber, S. M. Troian, and S. Wagner, "Capacitive sensing of droplets for microfluidic devices based on thermocapillary actuation," *Lab Chip*, vol. 4, no. 5, pp. 473–480, 2004.

[79] C. Elbuken, T. Glawdel, D. Chan, and C. L. Ren, "Detection of microdroplet size and speed using capacitive sensors," *Sensors Actuators, A Phys.*, vol. 171, no. 2, pp. 55–62, 2011.

[80] C. G. Cooney, C. Y. Chen, M. R. Emerling, A. Nadim, and J. D. Sterling, "Electrowetting droplet microfluidics on a single planar surface," *Microfluid. Nanofluidics*, vol. 2, no. 5, pp. 435–446, 2006.

[81] R. S. Hale and V. Bahadur, "Electrowetting-based microfluidic operations on rapid-manufactured devices for heat pipe applications," *J. Micromechanics Microengineering*, vol. 27, no. 7, 2017.

[82] X. Sun and K. D. Gillis, "On-chip amperometric measurement of quantal catecholamine release using transparent indium tin oxide electrodes," *Anal. Chem.*, vol. 78, no. 8, pp. 2521–2525, 2006.

[83] H. R. Velkoff and J. H. Miller, "Condensation of Vapor on a Vertical Plate With a Transverse Electrostatic Field," *J. Heat Transfer*, vol. 87, no. 2, p. 197, May 1965.

[84] H. Y. Choi, "Electrohydrodynamic Condensation Heat Transfer," *J. Heat Transfer*, vol. 90, no. 1, p. 98, Feb. 1968.

[85] R. E. Holmes and A. J. Chapman, "Condensation of Freon-114 in the Presence of a Strong Nonuniform, Alternating Electric Field," *J. Heat Transfer*, vol. 92, no. 4, p. 616, Nov. 1970.

[86] A. K. Seth and L. Lee, "The Effect of an Electric Field in the Presence of Noncondensable Gas on Film Condensation Heat Transfer," *J. Heat Transfer*, vol. 96, no. 2, p. 257, May 1974.

[87] A. Yabe, "Active heat transfer enhancement by applying electric fields," in *Proceedings of the 1991 ASME JSME thermal engineering joint conference*, 1991.

[88] K. Yamashita, M. Kumagai, S. Sekita, A. Yabe, T. Taketani, and K. Kikuchi, "Heat transfer characteristics on an EHD condenser," in *In Proceedings of the 1991 ASME JSME thermal engineering joint conference.*, 1991.

[89] A. Yabe, T. Taketani, Y. Yoshizawa, and K. Sunada, "Experimental study of EHD pseudo-dropwise condensation," in *Proceedings of the 1991 ASME JSME thermal engineering joint conference.*, 1991.

[90] M. K. Bologa, I. K. Savin, and A. B. Didkovsky, "Electric-field-induced enhancement of vapour condensation heat transfer in the presence of a non-condensable gas," *Int. J. Heat Mass Transf.*, vol. 30, no. 8, pp. 1577–1585, Aug. 1987.

[91] H. Omidvarborna, A. Mehrabani-Zeinabad, and M. N. Esfahany, "Effect of

electrohydrodynamic (EHD) on condensation of R-134a in presence of non-condensable gas," *Int. Commun. Heat Mass Transf.*, vol. 36, no. 3, pp. 286–291, Mar. 2009.

[92] H.-J. Butt, M. B. Untch, A. Golriz, S. A. Pihan, and R. Berger, "Electric-field-induced condensation: An extension of the Kelvin equation," *Phys. Rev. E*, vol. 83, no. 6, p. 061604, Jun. 2011.

[93] N. Miljkovic, D. J. Preston, R. Enright, and E. N. Wang, "Electrostatic charging of jumping droplets," *Nat. Commun.*, vol. 4, pp. 1–9, 2013.

[94] N. Miljkovic, D. J. Preston, R. Enright, and E. N. Wang, "Electric-field-enhanced condensation on superhydrophobic nanostructured surfaces," *ACS Nano*, vol. 7, no. 12, pp. 11043–11054, 2013.

[95] B. Bhatia *et al.*, "Nanoengineered Surfaces for Thermal Energy Conversion," *J. Phys. Conf. Ser.*, vol. 660, no. 1, 2015.

[96] X. Yan, J. Li, L. Li, Z. Huang, F. Wang, and Y. Wei, "Droplet condensation on superhydrophobic surfaces with enhanced dewetting under a tangential AC electric field," *Appl. Phys. Lett.*, vol. 109, no. 16, 2016.

[97] J. Oh *et al.*, "Jumping-droplet electronics hot-spot cooling," *Appl. Phys. Lett.*, vol. 110, no. 12, pp. 1–6, 2017.

[98] T. Foulkes, J. Oh, P. Birbarah, J. Neely, N. Miljkovic, and R. C. N. Pilawa-Podgurski, "Active hot spot cooling of GaN transistors with electric field enhanced jumping droplet condensation," *Conf. Proc. - IEEE Appl. Power Electron. Conf. Expo. - APEC*, pp. 912–918, 2017.

[99] J. Kim and M. Kaviany, "Purging of dropwise condensate by electrowetting," *J. Appl. Phys.*, vol. 101, no. 10, 2007.

[100] J. Kim and M. Kaviany, "Electrowetting purged surface condensate in evaporators," *Heat Transf. Eng.*, vol. 31, no. 2, pp. 101–107, 2010.

[101] R. Yan *et al.*, "Enhanced water capture induced with electrowetting-on-dielectric (EWOD) approach," *Appl. Phys. Lett.*, vol. 113, no. 20, p. 204101, 2018.

[102] G. M. Hobold and A. K. da Silva, "Machine learning classification of boiling regimes with low speed, direct and indirect visualization," *Int. J. Heat Mass Transf.*, vol. 125, pp. 1296–1309, Oct. 2018.

[103] C. Svensson *et al.*, "Coding of Experimental Conditions in Microfluidic Droplet Assays Using Colored Beads and Machine Learning Supported Image Analysis," *Small*, p. 1802384, Dec. 2018.

[104] T. Wang, T. H. Kwok, C. Zhou, and S. Vader, "In-situ droplet inspection and closed-

loop control system using machine learning for liquid metal jet printing," *J. Manuf. Syst.*, vol. 47, pp. 83–92, Apr. 2018.

[105] H. Yang, Z. Zhang, J. Zhang, and X. C. Zeng, "Machine learning and artificial neural network prediction of interfacial thermal resistance between graphene and hexagonal boron nitride," *Nanoscale*, vol. 10, no. 40, pp. 19092–19099, 2018.

[106] T. Zhan, L. Fang, and Y. Xu, "Prediction of thermal boundary resistance by the machine learning method," *Sci. Rep.*, vol. 7, no. 1, pp. 1–2, 2017.

[107] W. T. Scott, "Poisson Statistics in Distributions of Coalescing Droplets," *J. Atmos. Sci.*, vol. 24, no. 2, pp. 221–225, Mar. 1967.

[108] M. Warshaw, "Cloud Droplet Coalescence: Statistical Foundations and a One-Dimensional Sedimentation Model1," *J. Atmos. Sci.*, vol. 24, no. 3, pp. 278–286, May 1967.

[109] F. Al-Obeidat, B. Spencer, and O. Alfandi, "Consistently accurate forecasts of temperature within buildings from sensor data using ridge and lasso regression," *Futur. Gener. Comput. Syst.*, 2018.

[110] C. S. Sanjaya, T. H. Wee, and T. Tamilselvan, "Regression analysis estimation of thermal conductivity using guarded-hot-plate apparatus," *Appl. Therm. Eng.*, vol. 31, no. 10, pp. 1566–1575, 2011.

[111] Y. Sun, L. Gu, C. F. J. Wu, and G. Augenbroe, "Exploring HVAC system sizing under uncertainty," *Energy Build.*, vol. 81, pp. 243–252, 2014.

[112] A. B. Gandhi, J. B. Joshi, V. K. Jayaraman, and B. D. Kulkarni, "Development of support vector regression (SVR)-based correlation for prediction of overall gas hold-up in bubble column reactors for various gas-liquid systems," *Chem. Eng. Sci.*, vol. 62, no. 24, pp. 7078–7089, 2007.

[113] M. Maalouf, D. Homouz, and M. Abutayeh, "Accurate prediction of preheat temperature in solar flash desalination systems using kernel ridge regression," *J. Energy Eng.*, vol. 142, no. 2, pp. 1–7, 2016.

[114] K. M. Tao, "A closer look at the radial basis function (RBF) networks," 1993, pp. 401–405.

[115] S. Chavan *et al.*, "Heat Transfer through a Condensate Droplet on Hydrophobic and Nanostructured Superhydrophobic Surfaces," *Langmuir*, vol. 32, pp. 7774–7787, 2016.

[116] N. Miljkovic, R. Enright, and E. N. Wang, "Growth Dynamics During Dropwise Condensation on," in *ASME 2012 3rd Micro/Nanoscale Heat & Mass Transfer International Conference MNHMT2012*, 2012, vol. 1, pp. 1–10.

[117] N. Miljkovic, R. Enright, and E. N. Wang, "Effect of droplet morphology on growth dynamics and heat transfer during condensation on superhydrophobic nanostructured surfaces," *ACS Nano*, vol. 6, no. 2, pp. 1776–1785, 2012.

[118] J. W. Rose, "Dropwise condensation theory," *Int. J. Heat Mass Transf.*, vol. 24, no. 2, pp. 191–194, 1981.

[119] J. C. Baret, M. M. J. Decré, and F. Mugele, "Self-excited drop oscillations in electrowetting," *Langmuir*, vol. 23, no. 9, pp. 5173–5179, 2007.

[120] J. Lee, J. K. Park, J. Hong, S. J. Lee, K. H. Kang, and H. J. Hwang, "Nonlinear oscillations of a sessile drop on a hydrophobic surface induced by ac electrowetting," *Phys. Rev. E - Stat. Nonlinear, Soft Matter Phys.*, vol. 90, no. 3, pp. 33–36, 2014.

[121] Y. Lu, A. Sur, C. Pascente, S. Ravi Annapragada, P. Ruchhoeft, and D. Liu, "Dynamics of droplet motion induced by Electrowetting," *Int. J. Heat Mass Transf.*, vol. 106, pp. 920–931, 2017.

[122] M. H. Nazemi and V. Hinrichsen, "Experimental investigations on water droplet oscillation and partial discharge inception voltage on polymeric insulating surfaces under the influence of AC electric field stress," *IEEE Trans. Dielectr. Electr. Insul.*, vol. 20, no. 2, pp. 443–453, 2013.

[123] D. Chatterjee, B. Hetayothin, A. R. Wheeler, D. J. King, and R. L. Garrell, "Droplet-based microfluidics with nonaqueous solvents and solutions," *Lab Chip*, vol. 6, no. 2, pp. 199–206, 2006.

[124] C. Zhang, K. Khoshmanesh, A. Mitchell, and K. Kalantar-Zadeh, "Dielectrophoresis for manipulation of micro/nano particles in microfluidic systems," *Anal. Bioanal. Chem.*, vol. 396, no. 1, pp. 401–420, 2010.

[125] D. Liu and S. V. Garimella, "Microfluidic pumping based on traveling-wave dielectrophoresis," *Nanoscale Microscale Thermophys. Eng.*, vol. 13, no. 2, pp. 109–133, 2009.

[126] U. C. Yi and C. J. Kim, "Characterization of electrowetting actuation on addressable single-side coplanar electrodes," *J. Micromechanics Microengineering*, vol. 16, no. 10, pp. 2053–2059, 2006.

[127] C. P. Migliaccio, "Resonance-induced condensate shedding for high-efficiency heat transfer," *Int. J. Heat Mass Transf.*, vol. 79, pp. 720–726, Dec. 2014.

[128] R. A. Huber and M. M. Derby, "Droplet coalescence and departure on a vibrating film during humid air condensation," in *ASME 2017 15th International Conference on Nanochannels, Microchannels, and Minichannels, ICNMM 2017*, 2017.

[129] A. L. Yarin, D. A. Weiss, G. Brenn, and D. Rensink, "Acoustically levitated drops: Drop oscillation and break-up driven by ultrasound modulation," *Int. J. Multiph. Flow*, vol. 28, no. 6, pp. 887–910, Jun. 2002.

[130] E. Wikramanayake *et al.*, "Characterizing Microfluidic Operations Underlying an Electrowetting Heat Pipe on the International Space Station," 2018.

[131] M. Lokanathan, E. Wikramanayake, and V. Bahadur, "Scalably manufactured textured surfaces for controlling wettability in oil-water systems," *Mater. Res. Express*, vol. 6, no. 4, p. 046507, Jan. 2019.